DIGITAL PREDISTORTION LINEARIZATION FOR MULTI-BAND/MULTI-CHANNEL SOFTWARE DEFINED TRANSMITTERS

Ph.D THESIS

by

PRAVEEN JARAUT

DEPARTMENT OF ELECTRONICS AND COMMUNICATION ENGINEERING
INDIAN INSTITUTE OF TECHNOLOGY ROORKEE
ROORKEE - 247667, INDIA
NOVEMBER, 2018

DIGITAL PREDISTORTION LINEARIZATION FOR MULTI-BAND/MULTI-CHANNEL SOFTWARE DEFINED TRANSMITTERS

A THESIS

Submitted in partial fulfilment of the requirements for the award of the degree

of

DOCTOR OF PHILOSOPHY

in

ELECTRONICS AND COMMUNICATION ENGINEERING

by

PRAVEEN JARAUT

DEPARTMENT OF ELECTRONICS AND COMMUNICATION ENGINEERING
INDIAN INSTITUTE OF TECHNOLOGY ROORKEE
ROORKEE – 247 667 (INDIA)
NOVEMBER, 2018

INDIAN INSTITUTE OF TECHNOLOGY ROORKEE
ROORKEE

CANDIDATE'S DECLARATION

I hereby certify that the work which is being presented in the thesis entitled **"DIGITAL PREDISTORTION LINEARIZATION FOR MULTI-BAND/MULTI-CHANNEL SOFTWARE DEFINED TRANSMITTERS"** in partial fulfilment of the requirements for the award of the Degree of Doctor of Philosophy and submitted in the Department of Electronics and Communication Engineering of the Indian Institute of Technology Roorkee, Roorkee is an authentic record of my own work carried out during a period from July, 2014 to November, 2018 under the supervision of Dr. Meenakshi Rawat, Assistant Professor, Department of Electronics and Communication Engineering, Indian Institute of Technology Roorkee, Roorkee.

The matter presented in this thesis has not been submitted by me for the award of any other degree of this or any other Institute.

(PRAVEEN JARAUT)

This is to certify that the above statement made by the candidate is correct to the best of my knowledge.

(Meenakshi Rawat)
Supervisor

The Ph.D. Viva-Voce Examination of Praveen Jaraut, Research Scholar, has been held on March 2nd, 2019.

Chairman, SRC **Signature of External Examiner**

This is to certify that the student has made all corrections in the thesis.

Signature of Supervisor **Head of the Department**

Dated:_____

Abstract

Each generation of wireless communication systems is evolving to provide higher data rates with more services and accommodate more users within a limited radio-frequency (RF) spectrum. The wireless technologies, such as worldwide interoperability for microwave (WiMAX), Long Term Evolution (LTE), and Long Term Evolution-advanced (LTE-A) are being used to provide higher data rate wireless services. However, this places very challenging requirements for RF front-end specifications in terms of power efficiency and bandwidth for both base stations and hand-held devices. As the RF spectrum nowadays is shared by many users. Therefore, spectral efficient complex modulation schemes, such as orthogonal frequency-division multiplexing (OFDM), have to be used. In order to access these various schemes and services, the multi-band/multi-standard transceiver designs are used and getting enhanced in order to reduce power consumption, physical size and cost. The RF power amplifier (PA) is the main power consuming device in the multi-band and multi-input-multi-output (MIMO) transceivers and generates unwanted nonlinear distortion while operating close to the saturation region. The most optimum PA linearization technique is Digital Predistortion (DPD). The complexity and numerical stability of the DPD model is still a huge challenge.

The thesis investigates the issue of implementation complexity, numerical stability and feasibility of DPD model adaptation for low cost FPGAs for single band, multi-band and multi-channel transmission. Principal Component Analysis (PCA) based DPD technique is investigated as a solution to the numerical stability problem arising in lower-bits fixed-point digital signal processor/FPGA. It is reported with measurement results that PCA based model provides better linearization performance than memory polynomial (MP), orthogonal memory polynomial (OMP), and generalized memory polynomial (GMP) models in 16-bit fixed-point DSP operation.

Further, to enhance numerical stability of the state-of-the-art models, Independent Com-

ponent Analysis (ICA) as a novel algorithm level solution is proposed for different carrier aggregated (intra-band contiguous, intra-band non-contiguous and inter-band noncontiguous) LTE signals. ICA technique is proposed for 12-bit fixed-point digital signal processor/FPGA implementation of DPD for intra-band and inter-band CA signals. The application of the ICA technique upon MP model reduces model complexity and improves numerical stability of the DPD model for CA LTE signals. The proposed MP-ICA requires lesser memory requirement as compared to the state-of-the-art low complexity models such as MP model, OMP model and PCA-based memory polynomial (MP-PCA) model for CA LTE signals.

A novel two-dimensional curtailed harmonic memory polynomial (2D-CHMP) model to capture harmonic interferences, cross-modulation distortions (CMDs) and intermodulation distortions (IMDs) in concurrent dual-band PA operating at harmonic frequencies is further purposed to reduce the complexity of the state-of-the art models. The 2D-CHMP model is constructed by simplifying the envelope terms of the state-of-the-art two-dimensional harmonic memory polynomial (2D-HMP) model. The model complexity and memory requirement of 2D-CHMP are very less as compared to the 2D-HMP model. In addition, the novel DPD models is proposed for linearization of a previously uninvestigated case of concurrent tri-band PA at harmonic frequencies. This work analyzes the IMD terms which are producing harmonic distortions and proposes three-dimensional harmonic memory polynomial (3D-HMP) and harmonic Volterra spline (3D-HVS) models for mitigation of in-band interferences, CMDs, and IMDs.

As an integral solution to compensate for crosstalk, PA nonlinearity, I/Q imbalance and dc offset imperfections simultaneously in MIMO transmitters, a neural network (NN)-based DPD models has been investigated. The proposed NN DPD model provides a single-model digital mitigation solution to multi-branches of MIMO transmitters, which is suitable for higher order MIMO operation. A less complex, novel polynomial-based DPD model is also proposed for linearizing higher dimension MIMO transmitters along with its characterization procedure. The proposed model performs comparably to the state-of-art DPD model parallel Hammerstein (PH) with lower number of coefficients and floating point operations (flops).

Acknowledgements

I wish to express my deep sense of gratitude to Prof. Meenakshi Rawat for her excellent guidance and encouragement during the course of work. She has been generous in undertaking comprehensive discussions and meticulously reviewing of the thesis, without which the work could not have come to its present shape.

I would like to thank Prof. Debashis Ghosh, HOD, Electronics and Communication Engineering, IIT Roorkee, for providing necessary resources and friendly environment which helped me to carry out my research work in a lucid manner. My sincere gratitude to all the faculty members of my department for their invaluable support and suggestions. I would like to express my deep sense of gratitude to my research committee members, Prof. Dharmendra Singh, and Prof. Sandeep Kumar Garg for their continuous support and invaluable suggestions. Their suggestions and comments with regard to my thesis have helped me to improve my work. I wish to express my thanks to the non−teaching staff members Mr. Mahendra Singh and Mr. Anand Krishna Yadav of the Communication Laboratory.

I would like to thank my friends and lab-mates for valuable technical and non-technical discussions, hence making this journey memorable. I am thankful to my friend Manish Kumar for his support and encouragement.

I am thankful to my brother Manish Jaraut and sister-in-law Kusum for always believing in me.

I am extremely thankful to my parents who have been a constant support and love throughout my life. I am so blissed to have my son Medhansh whose single smile is enough to bring my stressful mind to peace. Most importantly, I would like to thank my wife Meena for her unconditional love and understanding, without which I could never made this far.

Praveen Jaraut

To

The Almighty,

My Mother and Father,

my soulmate cum friend

Meena

and my son

Medhansh.

Table of Contents

List of Figures

List of Tables

List of Abbreviations

2-D	:	Two-Dimensional
3-D	:	Three-Dimensional
4G	:	Fourth Generation
5G	:	Fifth Generation
ACEPR	:	Adjacent Channel Error Power Ratio
ACPR	:	Adjacent Channel Power Ratio
ADC	:	Analog-to-Digital Converter
AM-AM	:	Amplitude Modulation to Amplitude Modulation
AM-PM	:	Amplitude Modulation to Phase Modulation
AWGN	:	Additive White Gaussian Noise
BER	:	Bit Error Rate
CA	:	Carrier Aggregation
CMD	:	Cross-Modulation Distortion
CR	:	Cognitive Radio
DAC	:	Digital-to-Analog Converter
DFT	:	Discrete Fourier Transform
DPD	:	Digital Predistortion
DSP	:	Digital Signal Processing
DUT	:	Device Under Test
EVM	:	Error Vector Magnitude
FIR	:	Finite Impulse Response
FLOP	:	Floating Point Operations
FPGA	:	Field-Programmable Gate Array
ICI	:	Inter Carrier Interference
IF	:	Intermediate Frequency

I/Q	:	In-phase / Quadrature-phase
IRR	:	Image Rejection Ratio
IFFT	:	Inverse Fast Fourier Transform
ISI	:	Inter Symbol Interference
LO	:	Local Oscillator
LS	:	Least Squares
LTE	:	Long Term Evolution
LUT	:	Look-Up Table
MP	:	Memory Polynomial
NMSE	:	Normalized Mean Square Error
MMSE	:	Minimum Mean Square Error
OFDM	:	Orthogonal Frequency Division Multiplexing
PA	:	Power Amplifier
PAPR	:	Peak to Average Power Ratio
PSD	:	Power Spectral Density
QAM	:	Quadrature Amplitude Modulation
QPSK	:	Quadrature Phase Shift Keying
PCC	:	Polynomial Cancellation Coding
RC	:	Raised Cosine
RF	:	Radio Frequency
SC-FDMA	:	Single Carrier Frequency Division Multiple Access
SDR	:	Software Defined Radio
SER	:	Symbol Error Rate
SINR	:	Signal to Interference Noise Ratio
SNR	:	Signal to Noise Ratio
SVD	:	Singular Value Decomposition
UWB	:	Ultra Wide Band
VSA	:	Vector Signal Analyzer
VSG	:	Vector Signal Generator
WCDMA	:	Wideband Code Division Multiple Access
WiFi	:	Wireless Fidelity
WiMaX	:	Worldwide Interoperability for Microwave Access

Chapter 1

Introduction

1.1 Background and Motivation

Wireless and mobile communication is evolving to offer newer services and higher data rates to more number of users within a limited radio-frequency (RF) spectrum. In order to meet the requirements, transceivers should support multi-standards, multiple bands and multiple-input multiple-output (MIMO) topology [1, 2]. Nowadays, complex modulation schemes, such as orthogonal frequency-division multiplexing (OFDM) is used in Long-Term evolution (LTE) and Worldwide Interoperability for Microwave Access (WiMAX) wireless technologies. These modulation schemes are spectrally efficient, but have a high peak-to-average power ratio (PAPR). The multi-carrier and carrier aggregation (CA) techniques are used to increase overall network capacity, data rates and achieve an allocation of the fragmented spectrum [3]. CA consists of combining various component carriers (CCs). In Long Term Evolution-Advanced (LTE-A), CA of up to five CCs, each of up to 20 MHz is possible [4]. This places very challenging requirements for radio frequency (RF) front-end specifications in terms of power efficiency for base stations. When base station connects to user equipments (UEs) in downlink operation, it requires high power and this requirement is met using Power Amplifier (PA) [5–19]. PA should operate near saturation region to satisfy the exacting requirements on power efficiency. However, PA behaves nonlinearly in saturation region and produces distortions. This undesirable effect due to non-linearity of the PA can be overcome by digital predistortion (DPD), which is also the most popular technique for linearization of PA [20–37, 48]. The DPD comprises of nonlinear digital model which pre-distorts the incoming signal, which in turn cancels the distortion generated by PA. Several behavioral

models consider static nonlinearities only [38, 39] but due to a poor decoupling in FET gate and drain as well as poor decoupling in BJT base and collector, electrical memory effects are present in PAs. The thermal memory effect is also present in PA due to junction temperature. Many behavioral methods such as Volterra [22] and Memory Polynomial (MP) [23, 24] have been widely used to account for these memory effects. Several variations of MP and Volterra models such as generalized memory polynomial (GMP) [27] and Modified Volterra Series or dynamic Volterra series [28, 29] were proposed. However, when a wideband signal is used, more number of coefficients are required in their DPD models due to prominent memory effects [32].

Therefore, DPD techniques with lower complexity are required to linearize the RF PA output especially for multi-channel communication systems such as multi-band and MIMO signal transmitters.

1.2 Thesis Objectives

1. Polynomial based solution proposed in single-band and concurrent dual-band DPD till now are either rigid in their performance or are very complex due to high number of coefficients and multiples of high order polynomials. Although these models provide adequate outcome for proof-of-concept, their real time implementation is still limited by their complexity. Thus the first objective is to reduce model complexity while maintaining linearization performance of DPD for single-band, concurrent multi-band transmission and MIMO transmission.

2. Currently proposed single-band and concurrent dual-band DPD models have high condition number of observation (predistorter) matrix which leads to numerically unstable solutions. Moreover, with fixed point implementation in Field-Programmable Gate Array (FPGA), model performance diverts drastically from its calculated output leading to inefficient implementation. Thus the second objective is to improve the numerical stability of digital models for successful implementation of DPD in single-band and concurrent multi-band transmission.

3. Recently, research in PA design is moving towards ultra-wideband application [11], which, in turn raises concern of interference from harmonics. These harmonic component might fall within the working range of ultra-wideband power. Generally bulky

filter-banks are used to filter out the harmonic signals, however if these filter-banks can be avoided using digital cancellation schemes, this will result in significant reduction in transmitter size. Keeping this innovative trend in mind, there had been very few recent attempts to model PA harmonics [40]. Harmonic cancellation feedforward techniques are proposed in [41] by injecting an uncorrelated signal at harmonic frequency, whereas [42] proposes a 2D-Harmonic Memory Polynomial and Harmonic 3-D Volterra (H3D-V) model for modeling and DPD when one of the harmonics of the signal interferes with the upper band and cannot be removed using RF filters, however proposed schemes are extremely bulky in nature and impractical to implement. Thus the third objective is to enhance the performance and to reduce the implementation cost of the existing Harmonic DPD schemes for concurrent dual-band and tri-band transmission.

4. Most of the researchers focus on the SISO transmitter behavioral modeling and in the case of MIMO transmitters, the most investigated case is of 2×2 MIMO. In the coming year higher-dimension MIMO is going to be incorporated in 5G, but research is limited up to 2×2 MIMO DPD design. Thus one of the objective of the thesis is to design efficient DPD technique for higher-dimension MIMO topologies to support the need for proposed massive MIMO schemes in 5G and beyond systems.

1.3 Thesis Contributions

1.3.1 Principal Component Analysis based effective DPD technique for low-cost FPGA implementation

This work investigates the issue of low-cost DPD implementation in fixed-point FPGA/digital signal processor by considering the bit-resolution along with lower number of coefficients. The impact of principal component analysis (PCA) on bit-resolution of DPD solution is investigated within the context of established DPD models. Unlike previously proposed PCA based solutions, it is established by simulation and measurement that the numerical stability problem associated with popular models such as MP can be alleviated when PCA is applied to the observation (predistorter) data matrix. It is reported that the PCA based model provides better linearization performance with the lesser memory size requirement and number

of LUTs in 16-bit fixed-point FPGA/digital signal processor operation than MP, orthogonal memory polynomial (OMP) and GMP models. The performance of the proposed model is evaluated in terms of normalized mean square error (NMSE), adjacent channel error power ratio (ACEPR), matrix condition number and dispersion coefficient for continuous Class-AB and ZX60-V63+ PAs using wide code-division multiple access signal (WCDMA) and LTE signal with PAPR around 9.895 dB and 11.92 dB respectively.

1.3.2 DPD technique for low resource consumption using Carrier Aggregated 4G/5G Signals

CA is an essential part of LTE signals for 4G/5G wireless communication. However, CA LTE signals place stringent conditions on the RF PAs. The multi-band operation, wider bandwidth and related hardware cost are few of the DPD implementation limitations identified for the multi-band PAs. In this work, we present novel Independent Component Analysis (ICA) method for the DPD models which is suitable for all three cases (intraband contiguous, intraband non-contiguous and inter-band non-contiguous) of CA. Salient point is that this method provides numerical stability to the coefficient vector by whitening process irrespective of the digital model. It has been established that the memory requirement of ICA-based memory polynomial (MP-ICA) model implementation is much lesser as compared to the state-of-the-art low complexity models such as MP model, OMP model and PCA-based memory polynomial (MP-PCA) model for CA LTE signals. The proof-of-concept is provided with two different measurement setups for establishing its versatility.

1.3.3 Digital Predistortion for concurrent multi-band transmission at harmonic frequencies

Multi-band transmitter systems are evolving to support the smooth transition from 4G to 5G communication systems. Moreover, recent developments of multi-band and ultra-wideband PAs have led to a novel scenario where the second carrier signal is transmitted at the harmonic frequency of the first carrier signal. This results in harmonic interference from the first carrier signal as well as additional cross-modulation distortion (CMD) and intermodulation distortion (IMD) components, which cannot be filtered out. The computational and memory requirements for DPD in such scenario increase drastically to include all the interference

terms. This work presents a novel two-dimensional curtailed harmonic memory polynomial (2D-CHMP) model to capture harmonic interferences, CMDs and IMDs. The model complexity and memory requirement of 2D-CHMP are very less as compared to the state-of-the-art 2D-HMP model. For proof-of-concept, it is shown with two different measurement setups that the proposed 2D-CHMP DPD provides similar linearization performances as compared to the 2D-HMP DPD with lesser number of coefficients and computational complexity.

In the second part of this work, we investigate and present the novel DPD models for linearization of a previously uninvestigated case of concurrent tri-band PA at harmonic frequencies. This work analyzes the intermodulation (IMD) terms, which are producing harmonic distortions and proposes three-dimensional harmonic memory polynomial (3D-HMP) and harmonic Volterra spline (3D-HVS) models for mitigation of in-band harmonic, CMDs and IMDs.

1.3.4 DPD Model for mitigation of imperfections in MIMO Transmitters

Multi-input multi-output (MIMO) is anticipated to be a prominent technique proposed in the wireless communications to improve the system capacity and data rates of wireless networks. However, the MIMO transmitter suffers from imperfections like crosstalk, PA nonlinearity, in-phase and quadrature (I/Q) imbalance and dc offset. Investigating these effects, this work proposes neural network (NN)-based DPD as an integral solution to compensate for crosstalk, PA nonlinearity, I/Q imbalance and dc offset imperfections simultaneously in MIMO transmitters. The proposed NN DPD model provides a one-step single-model digital mitigation solution to multi-branches of MIMO transmitters. With the increase in the dimensions of MIMO transmitter, the proposed NN-based DPD model provides better compensation for transmitter imperfections and also reduces the complexity as compared to the state-of-the-art DPD methods. The proof-of-concept is provided with the 2×2 and 3×3 MIMO transmitters in the presence of strong PA nonlinearity, crosstalk, I/Q imbalance and dc offset for homodyne as well as heterodyne transmitters' cases.

This work also proposes a less complex, novel polynomial-based model for DPD for linearizing MIMO transmitters along with its characterization procedure. The proof-of-concept is provided with the 4×4 MIMO transmitters in the presence of nonlinear crosstalk, linear crosstalk and strong PA nonlinearity. The proposed model performs comparably to the state-

of-art DPD model parallel Hammerstein (PH) with lower number of coefficients and floating point operations (flops).

1.4 Outline of the Thesis

The summary of the work presented in each chapter is briefly outlined as follows:

Chapter 2: This chapter provides a detailed literature review of the work done by various researchers in the field of DPD. The mathematical formulation of various DPD models are discussed.

Chapter 3: This chapter investigates the issue of DPD implementation in low-bit fixed-point arithmetic and proposes PCA as a solution for established DPD models.

Chapter 4: This chapter presents a novel ICA method for the DPD models for CA LTE signals. In this chapter, the memory requirement by MP-ICA DPD model is compared to the state-of-the-art low complexity models such as MP model, OMP model and MP-PCA model for CA LTE signals.

Chapter 5: This chapter presents novel 2D-CHMP model to capture harmonic interferences, CMDs and IMDs in concurrent dual-band transmitter at harmonic frequencies. This chapter also presents a novel DPD models for linearization of concurrent tri-band transmitter at harmonic frequencies.

Chapter 6: In this chapter, we present a neural network (NN)-based DPD as an integral solution to compensate for crosstalk, PA nonlinearity, I/Q imbalance and DC offset imperfections simultaneously in MIMO transmitters. This chapter also presents a novel polynomial-based DPD model for the mitigation of imperfections like crosstalk and PA nonlinearity in MIMO transmitters.

Chapter 7: This chapter concludes the present study and compares the results obtained. Further, recommended research directions for future investigations are also discussed.

Chapter 2

Behavioral Models for Digital Predistortion Techniques: Survey

2.1 Introduction

With the goal of being more energy efficient, PAs should operate in the highly nonlinear region close to the saturation. However, when they operate in that region, PAs produce high level of out-of-band and in-band distortion. The preditortion can be performed on baseband, intermediate frequency (IF) or RF signals. For baseband level predistortion, a baseband signal should be passed through DPD linearizer implemented into Digital Signal Processing (DSP) that, in an ideal case, is the PA's inverse transfer function (Figure 2.1) [36]. The resultant transfer function of DPD+PA system is a linear function.

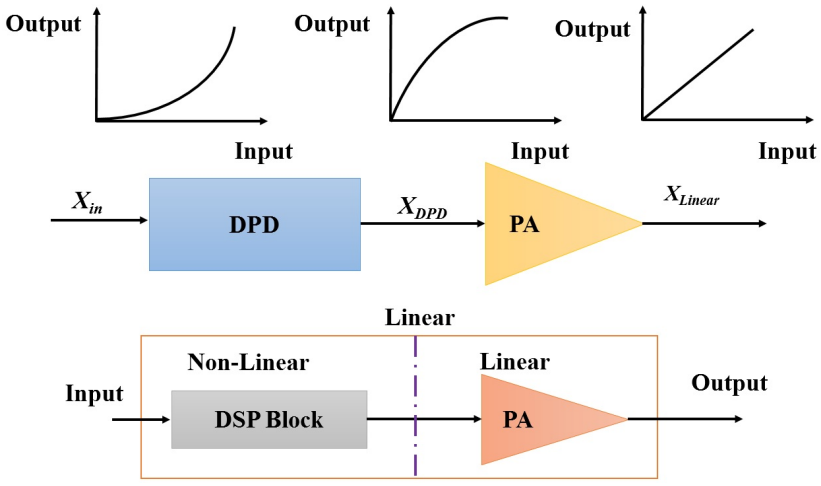

Figure 2.1: The fundamental concept of DPD [36].

2.2 Device under Test (DUT) Model Extraction

DPD consists of the digital predistorter block cascaded with a PA [36]. Digital predistorter is complementary non-linearity upstream of the PA. Behavioral modeling is performed to estimate the non-linearity and memory effects of the PA and the transmitter in general. According to indirect learning scheme of DPD implementation, the Predistortion function is equivalent to the behavioral modeling of the PA's inverse transfer function obtained by interchanging the input and output signals with appropriate small-signal (linear) gain normalization [36].

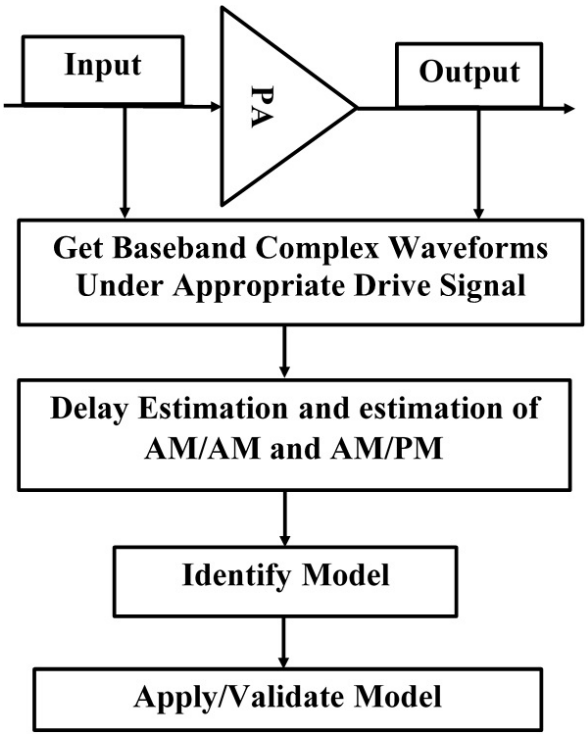

Figure 2.2: Behavioral model extraction procedure [36].

The behavioral modeling procedure is shown in Figure 2.2. It can be separated into two main parts: the characterization and the model extraction.

- The characterization corresponds to the experimental acquisition of the input and output PA signals, delay estimation, delay compensation and estimation of AM/AM and AM/PM characteristics [36].

- The model extraction refers to the choice of an appropriate mathematical function that defines all the substantial interaction between the input and output PA signals, its identification and validation [36].

2.3 Single-Band Digital Predistortion

Some of the frequently used models (formulations) in single-band are Look-Up-Table (LUT) based models, volterra based models and its variation. The LUT based models are memmoryless LUT, wiener, hammerstein and nested LUT models [20, 21, 36]. Several variations of the volterra based models are MP, envelope memory polynomial, orthogonal polynomial, generalized memory polynomial (GMP) and Modified Volterra Series or dynamic Volterra series [22–29]. The overview of these models is as follows:

2.3.1 Look-Up-Table (LUT) Model

The look-up-table model is the behavioural model used for the memoryless nonlinearities [20]. Two look-up tables are used to store complex gain of the DUT. The output signal of the model is given as:

$$x_{out}(n) = G(|x_{in}(n)|)x_{in}(n) \tag{2.1}$$

where $x_{in}(n)$ is the baseband input signal and $G(|x_{in}(n)|)$ is the instantaneous complex gain of the DUT.

2.3.2 Wiener Model

The Wiener model consists of a linear finite impulse response (FIR) filter block cascaded by a memoryless nonlinear function [36]. The output signal is given by

$$x_1(n) = \sum_{j=0}^{M} h(j)x_{in}(n-j) \tag{2.2}$$

and

$$x_{out}(n) = G(|x_1(n)|)x_1(n) \tag{2.3}$$

where M, $h(j)$, $x_1(n)$ and G are the memory depth, coefficients of the FIR filter impulse response, the output of the FIR filter and the memoryless instantaneous gain function applied in the look-up table model respectively.

The memoryless nonlinearity can be represented by a LUT or memmoryless polynomial model.

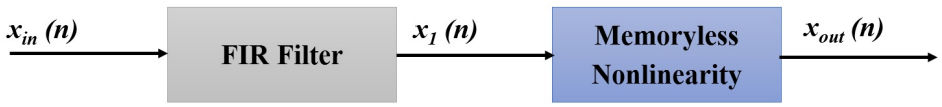

Figure 2.3: Wiener Model [36].

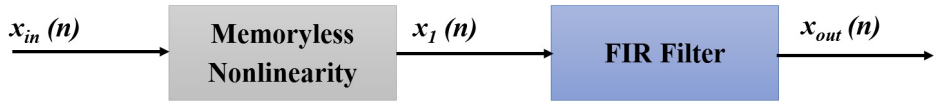

Figure 2.4: Hammerstien Model [36].

2.3.3 Hammerstein Model

The Hammerstein Model model is a two-box model composed of a memoryless nonlinear function followed by a linear FIR filter [36]. The output signal of the model is

$$x_1(n) = G(|x_{in}(n)|)x_{in}(n) \tag{2.4}$$

and

$$x_{out}(n) = \sum_{j=0}^{M} h(j)x_1(n-j) \tag{2.5}$$

where M, $G(|x_{in}(n)|)$, $h(j)$ and $x_1(n)$ are the memory depth, the instantaneous gain of the look-up table model, coefficients of the FIR filter impulse response and the output of the first box (look-up table model) respectively.

2.3.4 Nested Look-Up-Table Model

The nested look-up-table model for RF PAs exhibiting memory effects was proposed in [21], where look-up-table-based model was augmented to include memory effects. In this model, the instantaneous gain of the DUT is a function of the actual input sample $x_{in}(n)$ and the M-1 preceding samples [$x_{in}(n-1)$, $x_{in}(n-2)$,.....,$x_{in}(n-M)$]. Therefore, the size of look-up table is K^{M+1}, where K is the number of bins required for the memoryless look-up table model.

The output signal of the model is

$$x_{out}(n) = G(|X_{in}(n)|)x_{in}(n) \tag{2.6}$$

where $G(|X_{in}(n)|)$ is the instantaneous complex gain of the DUT, $X_{in}(n))$ is the input vector

including the present and the M preceding samples given as

$$X_{in}(n) = [x_{in}(n-1)x_{in}(n-2), ..., x_{in}(n-M)] \tag{2.7}$$

2.3.5 Volterra Model

The Volterra Model is best suited for dynamic nonlinear system [22]. The output signal of the model is given as:

$$y(n) = \sum_{k=1}^{K} \sum_{i_1=0}^{M} .... \sum_{i_p=0}^{M} h_p(i_1, i_2...., i_p) \prod_{j=1}^{k} x(n-i_j) \tag{2.8}$$

where M, K and $h_p(i_1, i_2...., i_p)$ are the memory depth, nonlinearity order and the parameters of the volterra model respectively.

2.3.6 Memory Polynomial Model

The MP model has been extensively used to account for the memory effects present in PAs. MP model is a simplified variant of Volterra series, in which only diagonal elements are retained. [23, 24]. The output signal is given by

$$y(n) = \sum_{k=0}^{K-1} \sum_{m=0}^{M} a_{km} \cdot x(n-m) \left|x(n-m)\right|^k \tag{2.9}$$

where M, K and $a_{k,m}$ are the memory depth, nonlinearity order and coefficients of the model respectively.

2.3.7 Orthogonal Polynomial model

The Orthogonal Polynomial model utilizes the properties of orthogonal polynomial basis function to reduce the condition number, which is order of magnitudes smaller than the conventional polynomial function [25]. For the uniformly distributed $|x|$, the k^{th} order orthogonal polynomial basis function is

$$\psi_k(x) = \sum_{u=1}^{k} (-1)^{u+k} \frac{(k+u)!}{(u-1)!(u+1)!(k-u)!} \left|x\right|^{u-1} x \tag{2.10}$$

The Output is

$$y = \sum_{k=1}^{K} \sum_{u=1}^{k} b_k (-1)^{u+k} \frac{(k+u)!}{(u-1)!(u+1)!(k-u)!} \left|x\right|^{u-1} x \tag{2.11}$$

where K and b_k are the non-linearity order and coefficients of the model respectively.

2.3.8 Envelope-Memory Polynomial Model

The compact envelope-memory polynomial based model was presented in [26]. It can be generalized as a integration between the nested look-up model and memory polynomial [24]. The output of this model is

$$y(n) = \sum_{m=0}^{M} \sum_{k=0}^{K-1} a_{k,m} x(n) \left|x(n-m)\right|^k \tag{2.12}$$

where M, K and $a_{k,m}$ are the memory depth, nonlinearity order and coefficients respectively. As only the magnitude of memory terms $[x(n-1)x(n-2), ..., x(n-M)]$ is required and their complex values are not required. Thus the DPD implementation for this model is simple.

2.3.9 Generalized Memory Polynomial Model

In this model, cross-terms are introduced using the different Volterra basis [27]. Taking delayed variations of equation (2.9) using both negative and positive crossterm time shifts and combining with equation (2.9) results in the GMP model

$$\begin{aligned} y(n) = \sum_{k=0}^{K_a-1} \sum_{l=0}^{L_a-1} a_{kl} x(n-l) \left|x(n-l)\right|^k + \sum_{k=0}^{K_b-1} \sum_{l=0}^{L_b-1} \sum_{m=1}^{M_b} b_{klm} x(n-l) \left|x(n-l-m)\right|^k \\ + \sum_{k=0}^{K_c-1} \sum_{l=0}^{L_c-1} \sum_{m=1}^{M_c} c_{klm} x(n-l) \left|x(n-l+m)\right|^k \end{aligned} \tag{2.13}$$

where K_a, K_b and K_c are the non-linearity orders, and L_a, L_b, M_b, L_c and M_c are the memory depths respectively.

There are various DPD models further proposed like modified Volterra series or dynamic reduced, rational basis and spline-based models [28–31].

2.4 Multi-Band Digital Predistortion

The 5th Generation (5G) network system and services requires the transceiver to simultaneously support the different frequency bands. To satisfy the multi-standard, multi-band requirements of the modern radio base stations, recent advancement in PA design have given

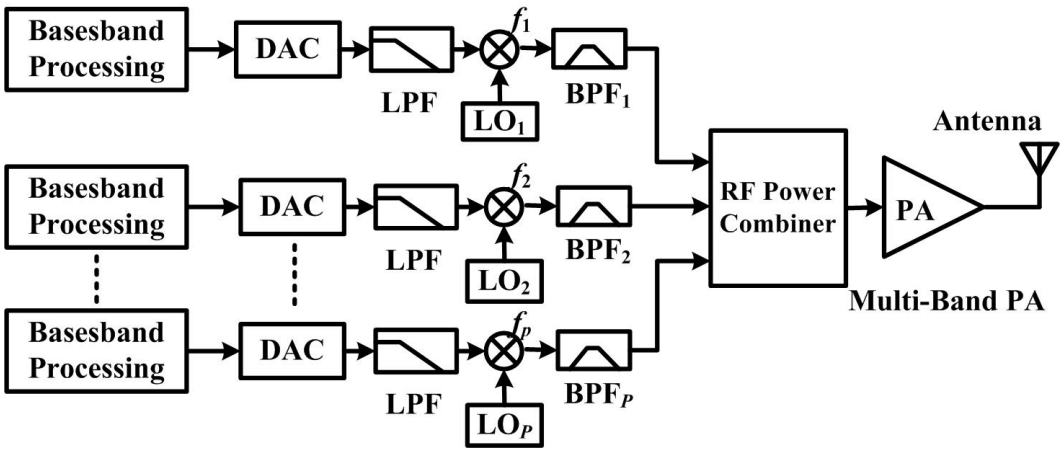

Figure 2.5: Multi-Band RF transmitter architecture [43].

the provision to concurrently drive it with a signal consisting of widely separated bands, permitting to cover multi-band operation with only one amplification stage. Figure 2.5 demonstrates the Multi-Band RF transmitter architecture.

However, when bands are far apart, together they form a wideband signal, which requires impractical high-sampling rate in digital-to-analog converters (DACs) and analog-to-digital converters (ADCs). Therefore multi-band DPD are preferred, where the carrier signals in each band are processed individually. The individual multi-band processing allow utilization of the low-speed ADCs and DACs in each path, such processing is independent of the frequency separation between the bands, which will require lower sampling rates than those used by wideband DPDs. The overview of a few of the DPD models is as follows:

2.4.1 Dual-Band Digital Predistortion (2-D DPD)

The two-dimensional memory polynomial (2D-MP) DPD technique is proposed to linearize the dual-band PA distortions, while using a frequency-selective algorithm with the inclusion of time-selective memory effects [43]. In this technique, each frequency band is processed individually. In concurrent dual-band scenario, two baseband modulated input signals x_1 and x_2 are transmitted at carrier frequencies ω_1 and ω_2 respectively. These carrier frequencies lie in different frequency bands. The outputs of the model is given as

$$y_r(n) = \sum_{m=0}^{M} \sum_{k=0}^{K-1} \sum_{i=0}^{k} c_{m,k,i}^{(r)} \cdot x_r(n-m) \cdot |x_r(n-m)|^{k-i} \cdot |x_s(n-m)|^i \tag{2.14}$$

where $r, s \in \{1, 2\}$ and $r \neq s$, M is the memory depth, $c_{m,k,i}^{(r)}$ are the coefficients and K is the nonlinearity order of the 2D-MP model.

2.4.2 Dual-Band Orthogonal Memory Polynomial (2D-OMP)

In [44, 45], 2D-OMP model is proposed. The output of this model is given as

$$y_r(n)=\sum_{m=0}^{M}\sum_{k=1}^{K}\sum_{i=0}^{k-1} c_{m,k,i}^{(r)} \cdot \gamma_{k,i}(x_r(n-m)\,, x_s(n-m)) \tag{2.15}$$

where $\gamma_{k,i}\left(x_r, x_s\right)=\lambda_{k-i}\left(x_r\right) \times \psi_i\left(x_s\right)$ and

$$\begin{aligned} \lambda_k(x_r)&=\sum_{u=1}^{k}(-1)^{u+k}\tfrac{(k+u)!}{(u-1)!(u+1)!(k-u)!}x_r \cdot |x_r|^{u-1} \\ \psi_i(x_s)&=\sum_{u=0}^{i}(-1)^{u+i}\tfrac{(i+u)!}{(u!)^2(i-u)!}|x_s|^u \end{aligned} \tag{2.16}$$

In [45], it is shown that 2D-OMP model has low condition number for known signal probability density functions (PDFs) such as uniform, truncated exponential and rayleigh distributions.

2.4.3 Low-Complexity 2-D DPD

In order to simplify 2D-MP model, the approach named 2-D Modified Memory Polynomial model was developed by Y.-Jiang Liu *et al.* in [46]. The outputs of low-complexity 2D model are mathematically expressed as :

$$y_1(n) = \sum_{m=0}^{M}\sum_{k=0}^{K-1} h_{km}^{(1)} x_1(n-m) f_{k+1}(|x_1(n-m), x_2(n-m))| \tag{2.17}$$

$$y_2(n) = \sum_{m=0}^{M}\sum_{k=0}^{K-1} h_{km}^{(2)} x_2(n-m) f_{k+1}(|x_2(n-m), x_1(n-m))| \tag{2.18}$$

where K, M and $h_{km}^{(1)}$ & $h_{km}^{(2)}$ are the nonlinearity order, memory depth and model coefficients of each band respectively. $f_{k+1}(|x_1(n-m), x_2(n-m))|$ is derived for odd-order terms (odd numbers of k + 1) and has the following equation

$$f_{k+1}(|x_r|\,, |x_s|) = \begin{cases} 1 & , k=0 \\ |x_r|^2 + 2|x_s|^2 & , k=2 \\ |x_r|^4 + 6|x_r|^2|x_s|^2 + 3|x_s|^4 & , k=4 \\ |x_r|^6 + 12|x_r|^4|x_s|^2 + 18|x_r|^2|x_s|^4 + 4|x_s|^6 & , k=6 \end{cases} \tag{2.19}$$

Similarly $f_{k+1}(|x_1(n-m), x_2(n-m))|$ for even-order terms can be written as

$$f_{k+1}(|x_r|\,, |x_s|) = ||x_r| + j\,|x_s||^k, \qquad k = 1, 3, 5.. \tag{2.20}$$

where $r, s \in \{1, 2\}$ and $r \neq s$. This model can be also identified using least square algorithm. In comparison with the previously described 2D-MP model, this model uses two summations. The total number of coefficients is decreased from $(M + 1)(K)(K + 1)$ to $2(M + 1)(K)$.

There are various dual-band DPD models further proposed such as 2D-rational function based model, 2-D DPD is implemented using combinations of 1-D lookup tables (LUTs) and 2-D cubic splines model [47–49].

2.5 Concurrent Dual-Band DPD Models at Harmonics Frequencies

2.5.1 2D Harmonic Memory Polynomial (2D-HMP) Model

Let us consider two modulated complex baseband input signals x_1 and x_2 being transmitted at carrier frequencies ω_1=$\alpha\omega$ and ω_2=$\beta\omega$ respectively, where $\alpha, \beta \in \mathbb{Z}_+$ and $\alpha \neq \beta$. As illustrated in [42, 50], the 2D-MP model is not sufficient to capture harmonic interferences terms of ultra-wideband PA. For this scenario, the 2D-HMP model is proposed in [42] to capture the harmonic interferences and model the PA output. The outputs of this model are given as:

$$\begin{aligned} y_1(n) &= \sum_{m=0}^{M} V_{m,0}^{1,1}(n-m) \cdot x_1(n-m) \\ &+ \sum_{m=0}^{M_l} \sum_{q=1}^{Q_l} V_{m,q}^{1,2}(n-m) \cdot x_2^{\alpha q}(n-m) \cdot x_1^{*(\beta q-1)}(n-m) \\ &+ \sum_{m=0}^{M_u} \sum_{q=1}^{Q_u} V_{m,q}^{1,3}(n-m) \cdot x_1^{\beta q+1}(n-m) \cdot x_2^{*\alpha q}(n-m) \end{aligned} \tag{2.21}$$

and

$$\begin{aligned} y_2(n) &= \sum_{m=0}^{M} V_{m,0}^{2,1}(n-m) \cdot x_2(n-m) \\ &+ \sum_{m=0}^{M_l} \sum_{q=1}^{Q_l} V_{m,q}^{2,2}(n-m) \cdot x_2^{\alpha q+1}(n-m) \cdot x_1^{*\beta q}(n-m) \\ &+ \sum_{m=0}^{M_u} \sum_{q=1}^{Q_u} V_{m,q}^{2,3}(n-m) \cdot x_1^{\beta q}(n-m) \cdot x_2^{*(\alpha q-1)}(n-m) \end{aligned} \tag{2.22}$$

where $V_{m,q}^{r,p}(n) = V_{m,q}^{r,p}(|x_r(n)|, |x_s(n)|)$, $r, s \in \{1, 2\}$ and $r \neq s$ and $V_{m,q}^{r,p}(|x_r(n)|, |x_s(n)|)$ can be expressed as:

$$V_{m,q}^{r,p}(|x_r(n)|, |x_s(n)|) = \sum_{k=0}^{K-1} \sum_{i=0}^{k} c_{m,q,k,i}^{r,p} \cdot |x_r(n)|^{k-i} \cdot |x_s(n)|^i \tag{2.23}$$

where K is the nonlinearity order, M_l and M_u are the memory depths, Q_l and Q_u are the intermodulation product orders, $c^{r,p}_{m,q,k,i}$ are the coefficients of the lower (r=1) and upper band (r=2). Details of deriving equations (2.21), (2.22) and (2.23) can be found in [42].

The number of coefficients in each band of 2D-HMP model is
$[(M+1)+(M_l+1)\,Q_l+(M_u+1)\,Q_u]\cdot K\,(K+1)\,/2$.

2.5.2 Harmonic 3-D Volterra (H3D-V) model

As a reduced complexity version of 2D-HMP model, the harmonic 3-D volterra (H3D-V) model is proposed to capture the IMD2 and IMD3 terms using spline [42]. This model is expressed as:

$$y_1(n)=\sum_{m=0}^{M_l} V^m_{1,1}(n-m)\cdot x_1(n-m)+V^m_{1,2}(n-m)\cdot x_1^*(n-m)\cdot x_2(n-m) \tag{2.24}$$

$$y_2(n)=\sum_{m=0}^{M_u} V^m_{2,1}(n-m)\cdot x_2(n-m)+V^m_{2,2}(n-m)\cdot x_1^2(n-m) \tag{2.25}$$

where, $V^m_{b,p}(n)=V^m_{b,p}(|x_1(n)|\,,|x_2(n)|\,,\theta_{12}(n))$ with $\theta_{12}(n)=\angle\{x_1^2(n)x_2^*(n)\}$ is evaluated using spline.

2.6 DPD models for MIMO

Figure 2.6 shows the block diagram of a MIMO transmitters. In MIMO transmitters, signals are transmitted at the same carrier frequency in different transmitters' paths from antennas [51–53]. Therefore, if transmitters are not calibrated individually, the effect of multi-branch crosstalk magnifies, when the signal is distorted due to PA nonlinearity. The overview of a few of the DPD models is as follows:

2.6.1 Crossover Memory Polynomial Model (COMPM)

The cross-over memory polynomial model (COMPM) has been proposed to linearize the PA nonlinearities and to mitigate crosstalk [54]. In this model, the output of each transmitter's path is a linear sum of single-input memory polynomial functions. The output of the first transmitter in 2×2 MIMO using this model is

$$\begin{aligned} y_1(n)=&\sum_{m=0}^{M}\sum_{k=0}^{K-1} c^{(1)}_{m,k}\cdot x_1(n-m)\cdot|x_1(n-m)|^k\\ &+\sum_{m=0}^{M}\sum_{k=0}^{K-1} d^{(1)}_{m,k}\cdot x_2(n-m)\cdot|x_2(n-m)|^k \end{aligned} \tag{2.26}$$

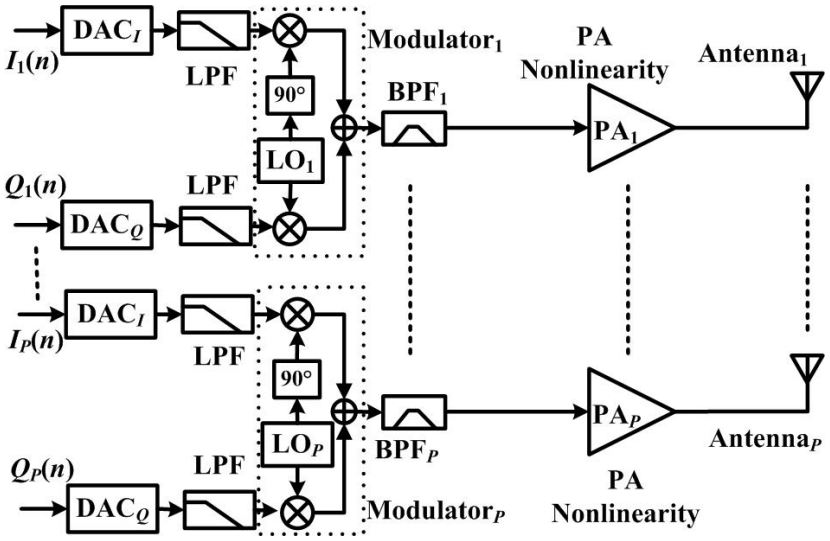

Figure 2.6: Block Diagram of MIMO transmitters.

where M is the memory depth, $x_1(n)$ and $x_2(n)$ are the baseband modulated input signals for the two transmitters, $c_{m,k}^{(1)}$ and $d_{m,k}^{(1)}$ are the coefficients and K is the nonlinearity order of the COMP model. The second output of the 2×2 MIMO transmitters can be obtained easily using a similar expression as in equation (2.26).

2.6.2 Parallel Hammerstein (PH) Model

The Parallel Hammerstein (PH) model provides the output of each transmitter's path as a linear sum of multiple-input memory polynomial functions [55]. The output of the first transmitter in 2×2 MIMO using this model is

$$\begin{aligned} & y_1(n) = f(x_1(n), x_2(n)) \\ & = \sum_{m=0}^{M} \sum_{k=0}^{K-1} \sum_{i=0}^{k} c_{m,k,i}^{(1)} x_1(n-m) \cdot |x_1(n-m)|^{k-i} \cdot |x_2(n-m)|^{i} \\ & + \sum_{m=0}^{M} \sum_{k=0}^{K-1} \sum_{i=0}^{k} d_{m,k,i}^{(1)} x_2(n-m) \cdot |x_1(n-m)|^{k-i} \cdot |x_2(n-m)|^{i} \end{aligned} \tag{2.27}$$

where $c_{m,k,i}^{(1)}$ and $d_{m,k,i}^{(1)}$ are the coefficients of PH model.

There have been a few more models presented for compensation of crosstalk and PA nonlinearities in MIMO transmitters [56–61].

2.7 Conclusions

In this chapter, an overview of the state-of-art DPD models for single-band, multi-band, and MIMO transmitters has been presented.

The single-band DPD models like volterra, MP, OMP and GMP models are complex and rigid in their performance due to high condition number. Similarly dual-band concurrent DPD models are highly complex and have high condition number.

The complexity of COMPM and PH models for MIMO transmitters increases exponentially with the increase of number of branches of MIMO transmitters.

In next chapters, systematic methodologies to design novel DPD algorithms for single-band, multi-band, and MIMO transmitters are presented. The DPD performance, model complexity and numerical stability of these proposed models have been carried out to validate the proposed theories presented in the thesis.

Chapter 3

PCA based effective DPD Technique for Low-Cost FPGA Implementation

3.1 Introduction

As established in the previous chapter, many behavioral methods such as Volterra [22] and MP [23, 24] have been widely used to account for the memory effects present in PA. However, when a wideband signal is used, more number of coefficients are required in their DPD models due to prominent memory effects [32]. As a result, size of ill-conditioned observation (predistorter) data matrix of DPD models increases and have high condition number and dispersion of coefficient leading to numerically unstable solutions. The OMP [25] model is a popular model to improve numerical stability. In [25], OMP model was implemented in 32-bit and 64-bit floating-point processors and the results show that it has better linearization performance than a MP model for lower-bit precision implementation. However, OMP model has two undesirable properties. One, the basis of orthogonality model does not consider memory effects and performance deteriorates when PA memory is taken into account. Second, the stability of the numerical solution is achieved by multiplying the orthogonal matrix to observation matrix, leading to higher computational complexity. Moreover, with the fixed-point arithmetic in lower bits FPGA, model performance diverts drastically from its floating-point based calculated output leading to inefficient implementation. In [62], the Volterra series based model was implemented using the lookup table (LUT) assisted gain indexing and time-division multiplexing for multiplier sharing to save memory size in FPGA. In [63], to reduce the complexity, least square (LS) based model extraction for less training

samples is obtained using a 1-bit ridge regression (1-bit RR) method and errors between the real transmit signal and the training data are reduced by a root mean square (RMS) based coefficients weighing and an averaging. In [64], a theoretical comparison between polynomials and the spline interpolation was presented. It is shown that Lagrange polynomial basis are similar to spline basis and both models can be used interchangeably and be united.

Keeping with the theme of reducing the complexity of DPD model implementation in [62–64], this chapter utilizes PCA as a solution to the numerical stability problem arising in lower bits FPGA. PCA projects correlated high-dimensional observation data matrix to uncorrelated low-dimensional observation data matrix [65]. In [66], the number of coefficients of DPD model was reduced using only larger eigen values. In [67], direct learning approach was used in the MP DPD technique and PCA was applied to reduce the order of observation (predistorter) matrix which was used to update the DPD coefficients. In [68, 69], PCA was implemented in DPD of concurrent dual band envelope tracking PA to reduce the order. In [70], PCA was combined with mesh-selecting method to reduce the order of observation (predistorter) data matrix dimension and reduced the cost of PA using under-sampled ADC. However all the earlier published work utilizing PCA [66–70] focuses only on reduction in matrix dimension which indicates a lower number of coefficients. However, the total FPGA memory size requirement depends on matrix size as well as bit-resolution [45]. This chapter reports the application of PCA for minimizing the FPGA memory size requirement [71]. The relevant metrics are taken as condition number and dispersion of coefficient which have a direct impact on lower bits FPGA implementation. In this chapter, an indirect learning approach is used in MP DPD technique with PCA implementation and it improves their condition number and dispersion coefficient while reducing the order of DPD matrix and keep maintaining the performance of the behavioral model in terms of NMSE and ACEPR.

This chapter is organized as follows: Section 3.2 describes the conventional PA modeling. Section 3.3 describes the PCA implementation in PA behavioral modeling. Section 3.4 describes the measurement setup used for the data extraction and DPD. Section 3.5 describes the MP-PCA modeling performance. Section 3.6 describes the experimental results of DPD, followed by a conclusion.

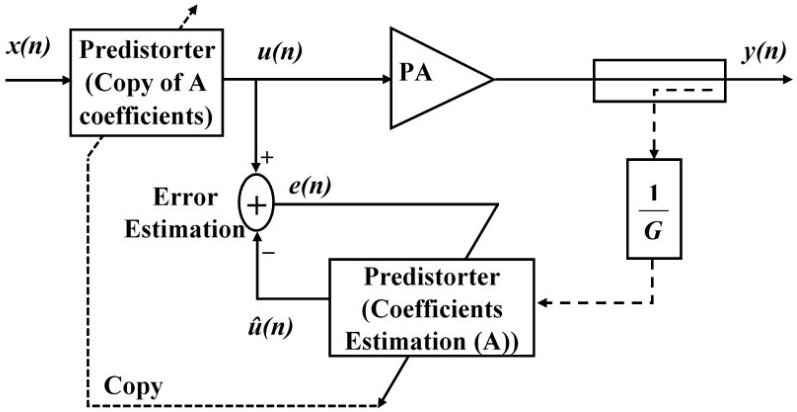

Figure 3.1: Indirect Learning Architecture.

3.2 Conventional PA Modeling

Figure 3.1 shows the indirect learning approach, which is a well established method for the DPD [24]. In Indirect learning architecture, the predistortion function is equivalent to the behavioral model of the PA's inverse transfer function obtained by swapping the input signal by output signal with appropriate small-signal (linear) gain normalization [36]. The input signal $x(n)$ is predistorted by the DPD block and this predistorted signal $u(n)$ is transmitted through the PA. The Output of PA, $y(n)$ normalized by small-signal (linear) gain (G) is provided to the DPD (coefficient estimator) block to generate *û(n)*.

The MP model is extensively used for behavioral modeling and inverse modeling for DPD of PAs/transmitters showing memory effects. Equation (2.9) representing the MP model can be written in matrix form as follows:

$$\mathbf{y} = \mathbf{UA} \tag{3.1}$$

where

- $\mathbf{y} = [y(n), y(n+1), \ldots, y(n+L-1)]^T$ is a $L \times 1$ vector representing the L samples of the output signal.
- $\mathbf{A} = [a_{00}, a_{01}, \ldots, a_{0K}, \ldots, a_{M0}, a_{M1}, \ldots, a_{MK}]^T$ is a $(M+1)(K) \times 1$ vector of MP model coefficients.
- $\mathbf{x} = [x(n), x(n+1), \ldots, x(n+L-1)]^T$ is a $L \times 1$ vector representing the L samples of the input signal.

- $\mathbf{U}$ is a $L \times (M+1)(K)$ observation (predistorter) data matrix shown as in Equation (3.2)

$$\mathbf{U} = \begin{bmatrix} x(n) & \cdots & x(n)|x(n)|^{K-1} & \cdots & x(n-M) & \cdots & x(n-M)|x(n-M)|^{K-1} \\ x(n+1) & \cdots & x(n+1)|x(n+1)|^{K-1} & \cdots & x(n+1-M) & \cdots & x(n+1-M)|x(n+1-M)|^{K-1} \\ x(n+2) & \cdots & x(n+2)|x(n+2)|^{K-1} & \cdots & x(n+2-M) & \cdots & x(n+2-M)|x(n+2-M)|^{K-1} \\ \cdots & \cdots & \cdots & \cdots & \cdots & \cdots & \cdots \\ x(n+L-1) & \cdots & x(n+L-1)|x(n+L-1)|^{K-1} & \cdots & x(n+L-1-M) & \cdots & x(n+L-1-M)|x(n+L-1-M)|^{K-1} \end{bmatrix} \tag{3.2}$$

$\mathbf{U}$ is a vandermonde matrix containing the input signal with memory effects in a geometric progression. Least Square (LS) method [72, 73] is used to extract MP model coefficient vector $\mathbf{A}$. Pseudo-inverse method is used to implement LS extraction as follows:

$$\mathbf{A} = (\mathbf{U}^{\mathrm{H}}\mathbf{U})^{-1}\mathbf{U}^{\mathrm{H}}\mathbf{y} \tag{3.3}$$

3.3 Proposed PCA implementation in PA Modeling

The observed dimensionality of the data matrix is often a lot higher than the true dimensionality [65]. This means we estimate a larger number of parameters (coefficients) than required. PCA reduces the dimensionality of the observation data matrix by projecting the data along the directions, which have the largest variance. These directions are the eigen vectors of the covariance matrix of the observation data matrix. The corresponding eigen value measures the variance of the data along an eigen vector.

For example, if $\mathbf{U}$ is a $L \times (M+1)(K)$ observation data matrix

$\mathbf{R} = \mathbf{U}^{\mathrm{H}}\mathbf{U}$ is its $(M+1)(K) \times (M+1)(K)$ covariance matrix

Using eigen value decomposition, $\mathbf{R} = Q\Lambda Q^{\mathrm{H}}$

where $q_1, q_2, \ldots, q_{(M+1)(K)}$ are the eigen vectors to the corresponding eigen values $\lambda_1, \lambda_2, \ldots,$ $\lambda_{(M+1)(K)}$ of the covariance matrix $\mathbf{R}$ such that $\lambda_1 \geq \lambda_2 \geq \ldots \geq \lambda_{(M+1)(K)}$.

$Q = [q_1, q_2, \ldots, q_{(M+1)(K)}]$ is a $(M+1)(K) \times (M+1)(K)$ matrix consisting of eigen vectors.

$\Lambda = diag(\lambda_1, \lambda_2, ..., \lambda_{(M+1)(K)})$ is a $(M+1)(K) \times (M+1)(K)$ diagonal matrix consisting of eigen values.

Dimensions of the new observation data matrix can be decided from the weight of eigen values e.g. determining how many dimensions are necessary to capture 99.99999999% of

the total data variance. This cumulative percentage of variation for first S Eigen values is known as Threshold T. T is mathematically expressed as

$$T = \frac{\lambda_1 + \lambda_2 + ... + \lambda_S}{\lambda_1 + \lambda_2 + ... + \lambda_{(M+1)(K)}} \times 100 \tag{3.4}$$

Threshold T can be chosen to find a new dimension S. Eigen vectors to the corresponding larger eigen values will be the principal components (new dimensions of data). Principal Components $\mathbf{P}$ would be defined as

$$\mathbf{P} = [q_1, q_2, \ldots, q_S] \tag{3.5}$$

Data are projected to a new low-dimensional space by doing an inner product of $\mathbf{U}$ with principal components $\mathbf{P}$. New observation data matrix $\mathbf{V} = \mathbf{UP}$ and $\mathbf{V}$ is not a vandermonde matrix.

The dimensions of the new observation data matrix $\mathbf{V}$ is reduced from $L \times (M+1)(K)$ to $L \times S$. Thus coefficients are also reduced from $(M+1)(K)$ to S.

Now

$$\mathbf{y} = \mathbf{VB} \tag{3.6}$$

where $\mathbf{B} = [b_0, b_1, \ldots, b_s]^T$ is a $S \times 1$ vector of MP-PCA coefficients and can be calculated using pseudo-inverse method. PCA implementation in MP model is termed as MP-PCA model.

3.4 Measurement Setup

Figure 3.2(a) and Figure 3.2(b) shows the block diagram and the photograph of measurement setup used for PA characterization respectively. The Measurement setup consists of a dual channel transmitter (TSW30SH84), Altera Arria V GT FPGA, transmitter observation receiver (TSW1266), ZN2PD2-50-S+ power splitter/combiner from Mini-Circuits, local oscillator (TSW3065), ZX60-V63+ PA from Mini-Circuits, 15-W continuous Class-AB PA, 10-W driver, and attenuators. Altera Arria V GT kit contains two 5AGTFD7K3 FPGAs and these FPGAs are programmed using Quartus Software. Altera Arria V GT kit is connected to the transmitter and data is transmitted from the FPGA to the transmitter at a sampling rate of 307.2 Msps. The dual channel transmitter TSW30SH84 from Texas Instruments (TI) contains 1.5 GSPS, 16-bit, digital-to-analog converter (DAC) DAC34SH84 and two complex RF

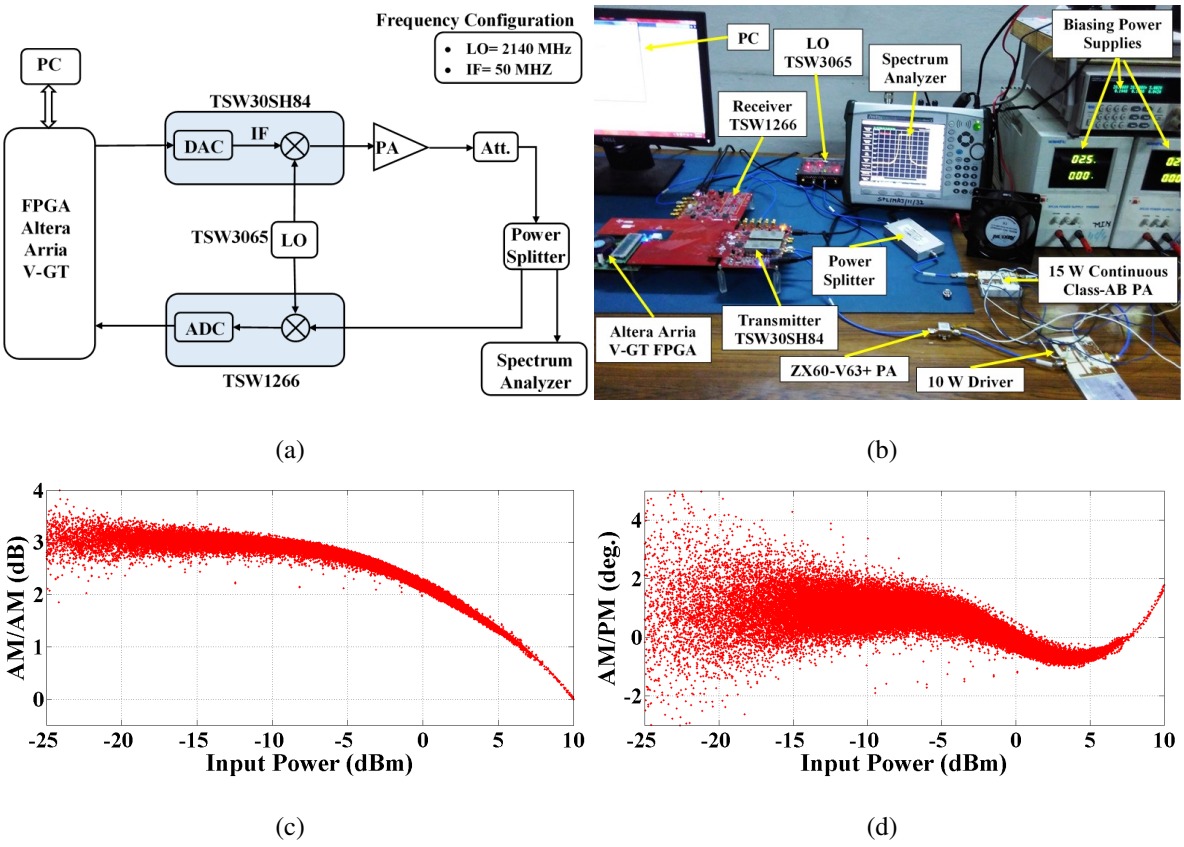

Figure 3.2: Block Diagram of Measurement Setup, (b) Photograph of Measurement Setup, (c) AM/AM characteristics of continuous Class-AB PA and (d) AM/PM characteristics of continuous Class-AB PA.

modulators TRF3705, with output frequency ranging from 300 MHz to 4 GHz. The data are interpolated by a factor of 4 in DAC to a sampling frequency of 1228.8 Msps. The TRF3705 up-converts the signal to RF using a Local oscillator (LO) (TSW3065) and sent to PA. At the receiving end, TSW1266 receiver down-converts the signal at a sampling frequency of 614.4 Msps. A 10 MHz reference clock from LO (TSW3065) synchronizes transmitter and receiver.

3.4.1 Devices and Signals Under Test

A 15-W continuous Class-AB PA is used for establishing the proof of concept. It is driven by ZX60-V63+ PA and 10-W driver. Class-AB PA is a 15 W gallium nitride (GaN) based PA, biased at a drain voltage of 28 V and drain current of 100 mA. ZX60-V63+ PA operates from 0.05 to 6 GHz frequency range and 17.8 dBm output at 1 dB gain compression. The ZX60-V63+ PA can be used in wide variety of applications like base station infrastructure, portable

Table 3.1: Effect of Threshold T on MP-PCA inverse modeling performance

	WCDMA Signal					**LTE Signal**				
Threshold *T* %	99	99.99	99.9999	99.999999	99.99999999	99	99.99	99.9999	99.999999	99.99999999
NMSE (dB)	-26.79	-46.06	-46.38	-48.28	-49.28	-19.63	-43.37	-45.09	-47.67	-48.92
ACEPR (dBc)	-43.53	-46.88	-47.42	-50.60	-53.18	-46.79	-47.31	-48.50	-51.79	-53.50
No. of Coeff.	2	4	7	12	18	2	5	10	15	22
Cond. No.	7.52	44.21	544.42	1.08×10^4	1.54×10^5	8.93	68.88	1.23×10^3	1.28×10^4	1.18×10^5
Disp. Coeff.	9.56	13.19	15.84	56.90	427.65	4.78	6.60	6.94	36.63	291.33

wireless, CATV, DBS, MMDS, wireless LAN, LTE , SATCOM and radar requiring moderate power output, low distortion and 50 ohm matched input/output ports. The practical RF PA performs amplification in three stages. The primary (ZX60-V63+ PA) and driving (10-W PA) stages actually amplify the signal RF power and provide greater than one gains, where as the third (15-W Class-AB PA) stage is used to transfer the signal after amplification and matching with antenna impedance.

The two different signals used for experimentation are 5 MHz WCDMA and 10 MHz LTE signals with PAPR of 9.895 dB and 11.92 dB respectively at 2190 MHz (2140 MHz LO + 50 MHz IF shift). The Amplitude Modulation/Amplitude Modulation (AM/AM) and Amplitude Modulation/Phase Modulation (AM/PM) characteristics of continuous Class-AB PA are shown in Figure 3.2(c) and Figure 3.2(d) respectively. The Class-AB PA has a 3.4 dB gain compression and phase scatter of 3.3°.

3.4.2 Time Alignment

Before sending data in FPGA, it is normalized by its maximum value and changed to hexadecimal format. At the receiver, data is converted from hexadecimal to decimal format and then normalized. The frequency domain cross-correlation method as defined in [40] is used to time align the transmitted and received data.

3.5 Inverse Modeling Performance

3.5.1 Matrix conditioning and Numerical Stability

Ill-conditioned observation data matrix in MP models results in numerical stability. A poorly conditioned matrix makes the pseudo-inverse calculation very sensitive to slight disturbances. The condition number is defined as a ratio of maximum eigen value to the minimum eigen value of observation data matrix [74]. It is expressed as

$$\text{Condition Number} = \frac{\lambda_{\max}}{\lambda_{\min}} \tag{3.7}$$

where $\lambda_{\max}$ and $\lambda_{\min}$ are maximum eigen value and minimum eigen value of observation data matrix respectively.

It is a measure of the transfer of error from the matrix to the LS solutions. At least n digits of precision can be lost in solving the system $\mathbf{y} = \mathbf{UA}$, if a condition number is 10^n [75]. For example, the numerical precision is around 10^{-6} for a single-precision floating-point calculation. Any condition number greater than 10^3 leads to an approximate precision of 10^{-3}. The observation data matrix $\mathbf{U}$ of MP model is badly conditioned Vandermonde matrix with high conditioning number [76,77]. Its pseudo-inverse calculation is very sensitive to the slight disturbances in FPGA setup which may lead to inaccurate results when finite precision calculation is used. But the MP-PCA model observation data matrix $\mathbf{V}$ is not Vandermonde matrix. Thus its condition number is not high as compared to the condition number of MP model.

The OMP model (discussed in chapter-2) has better numerical stability and matrix conditioning than the MP model. However, the basis of orthogonality model does not consider memory effects. So MP-PCA model can perform better than OMP model when memory effect occurs by considering the appropriate value of threshold T such that the ratio of maximum and minimum eigen values can be reduced.

Table 3.1 shows the effect of threshold T % on MP-PCA inverse PA modeling performance parameters for M=4 and K=7. In MP model, NMSE=-49.38 dB and ACEPR=-53.29 dBc are achieved for WCDMA signal. Similarly, NMSE=-49.01 dB and ACEPR=-53.60 dBc are achieved for LTE signal. It is to be noted that for T=99%, NMSE and ACEPR values of MP-PCA model are poor as compared to NMSE and ACEPR values of MP model. For T=99.99999999%, NMSE and ACEPR value of MP-PCA model are nearest to the NMSE and ACEPR value of MP model. Thus we choose T=99.99999999% for our MP-PCA model.

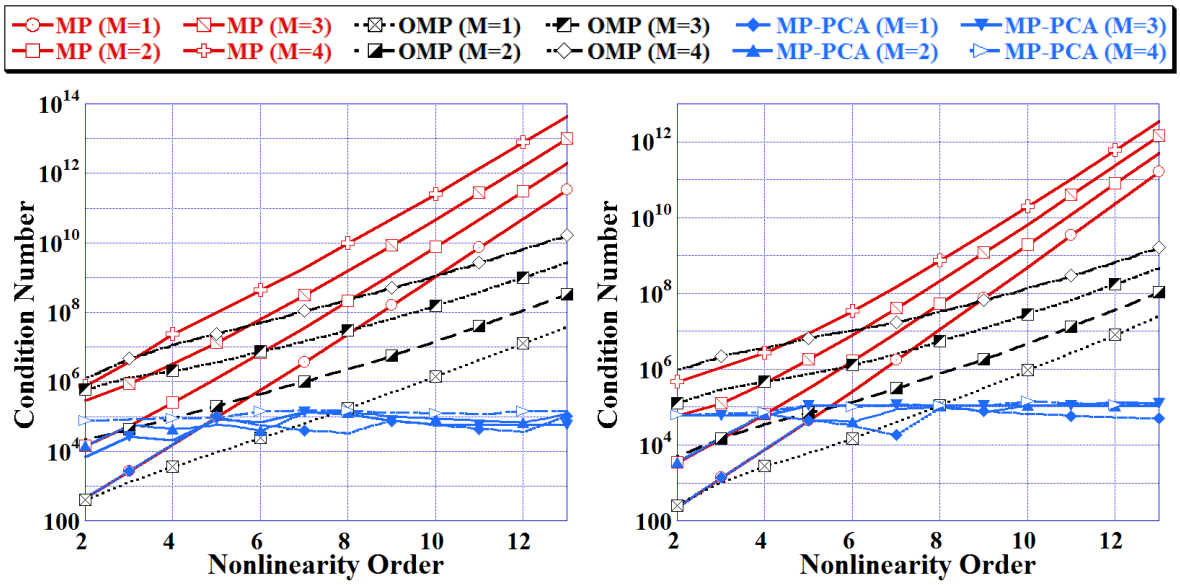

(a) (b)

Figure 3.3: Condition Number for continuous Class-AB PA inverse modeling: (a) WCDMA signal and (b) LTE signal.

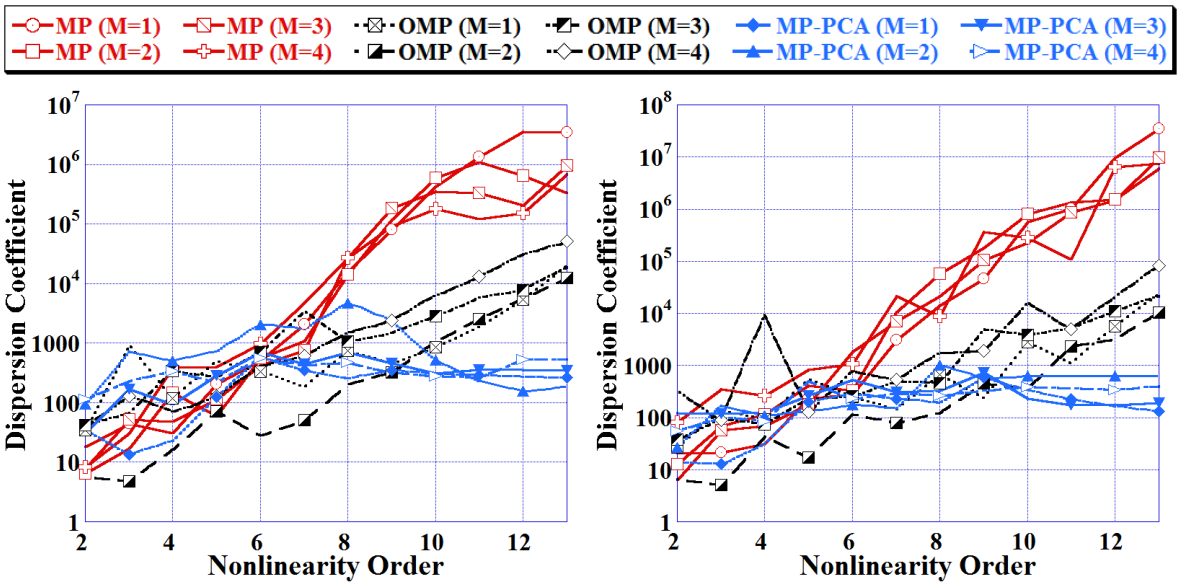

(a) (b)

Figure 3.4: Dispersion Coefficient for continuous Class-AB PA inverse modeling: (a) WCDMA signal and (b) LTE signal.

Figure 3.3(a) and Figure 3.3(b) shows the condition number of observation data matrix of MP model, OMP model and MP-PCA model for continuous Class-AB PA inverse modeling driven by 5 MHz WCDMA and 10 MHz LTE signals respectively. The x-axis of the graph represents nonlinearity order K. As shown in the graph, when nonlinearity order K and

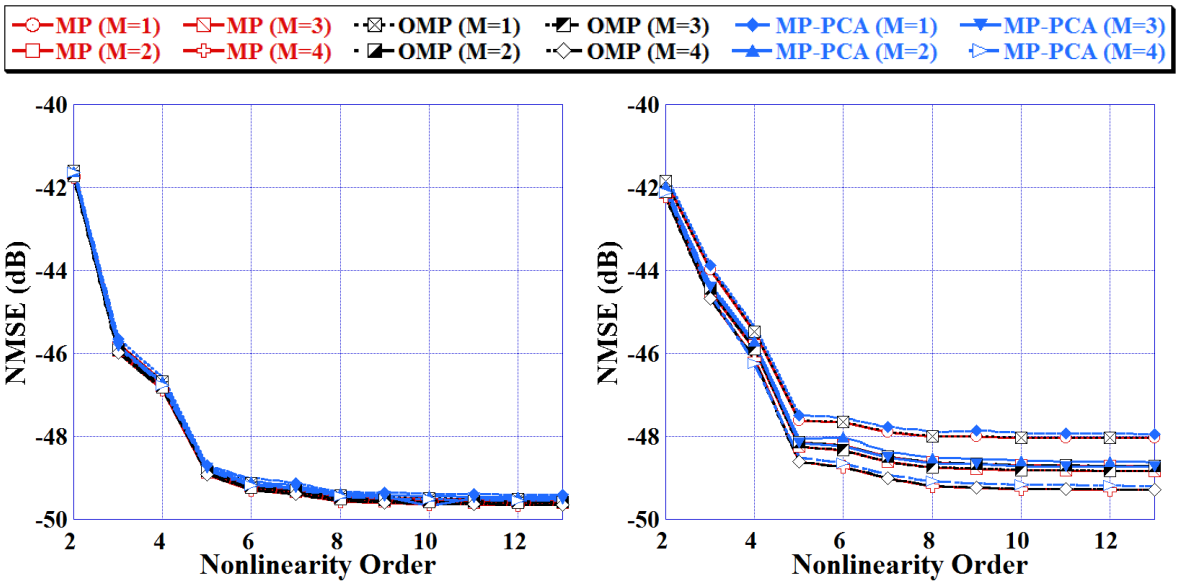

(a) (b)

Figure 3.5: NMSE performances of continuous Class-AB PA inverse modeling: (a) WCDMA signal and (b) LTE signal.

memory depth M are increasing, then condition number is increasing exponentially for both MP model and OMP model. Whereas the condition number of MP-PCA model is converging to maximum 10^5 and it is less than MP model by order of 10^6-10^8 and less than OMP model by order of 7×10^2-10^5 for both the signals. This large difference in condition number is due to the large difference between maximum eigen value and minimum eigen value. In MP-PCA model, this difference is reduced by considering only first S eigen values and discarding the remaining smaller eigen values i.e. λ_{S+1} to $\lambda_{(M+1)(K)}$ by choosing threshold T=99.99999999%.

Dispersion Coefficient is another factor to represent numerical stability and it represents the need for a higher number of bits required to cover the whole domain of coefficients in the digital signal processor. It is defined as a ratio of maximum to minimum absolute coefficient value [78]. It is expressed mathematically as

$$\text{Dispersion Coefficient} = \frac{\max(|a_{mk}|)}{\min(|a_{mk}|)} \tag{3.8}$$

where a_{mk} are the coefficients. The precision level of coefficients in lower-bit fixed-point DSP is compromised, when the coefficients are much dispersed. For example, if dispersion coefficient is 2^n then it will require at least $2n$ bit-resolution without losing any precision.

As shown in the Figure 3.4, when nonlinearity order K and memory depth M are increasing then dispersion coefficient is increasing exponentially for both MP model and OMP

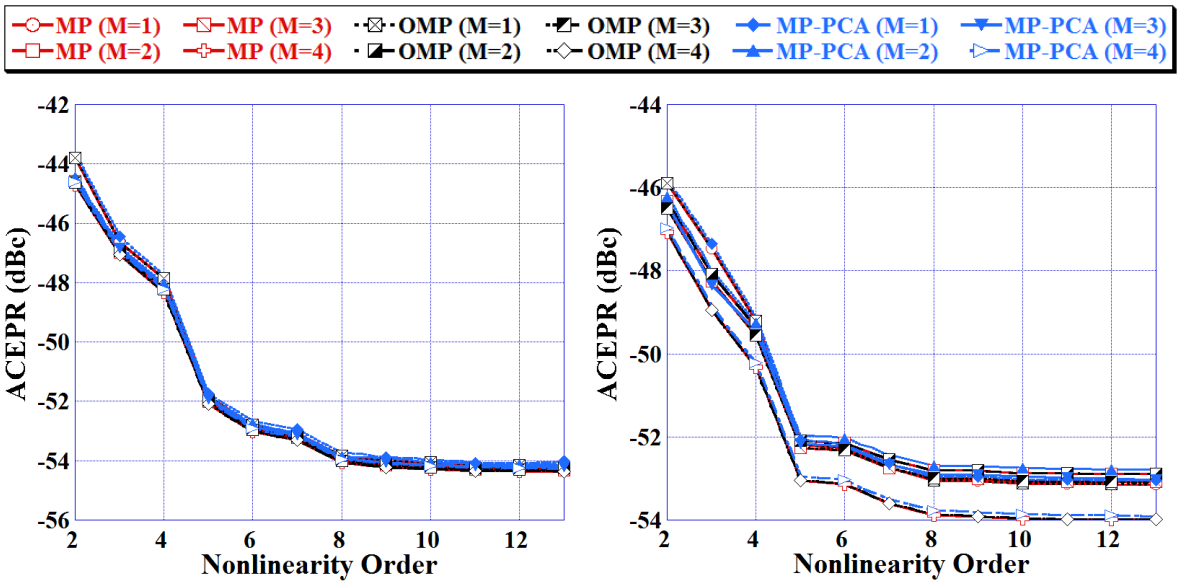

(a) (b)

Figure 3.6: ACEPR performances of continuous Class-AB PA inverse modeling: (a) WCDMA signal and (b) LTE signal.

model. The dispersion coefficient of MP-PCA model for WCDMA signal is converging to maximum 800 approximately and it is less than MP model by order of 10^3 and less than OMP model by order of 10-10^2. Similarly dispersion coefficient of MP-PCA model for LTE signal is converging to maximum 800 approximately and it is less than MP model by order of 10^4 and less than OMP model by order of 10-10^2.

3.5.2 In-Band and Out-of-Band Modeling Performance

Error Performance of a behavioral model is shown by metrics like NMSE and ACEPR.

The In-band distortion present in a signal can measured by normalized mean square error (NMSE). NMSE is used in time-domain modeling [79] and it is given by

$$\text{NMSE (dB)} = 10\log_{10}\left(\frac{\sum_{n=1}^{L}|e(n)|^2}{\sum_{n=1}^{L}|y_{meas}(n)|^2}\right) \tag{3.9}$$

where L is the total number of samples and $e(n) = y_{meas}(n) - y_{est}(n)$ is the error between measured output $y_{meas}(n)$ and the estimated model output $y_{est}(n)$ for any sample n.

Figure 3.5 shows that NMSE results are nearly same for MP model, OMP model and MP-PCA model for memory depth of M=1 to M=4 and nonlinearity order of K=2 to K=13 respectively.

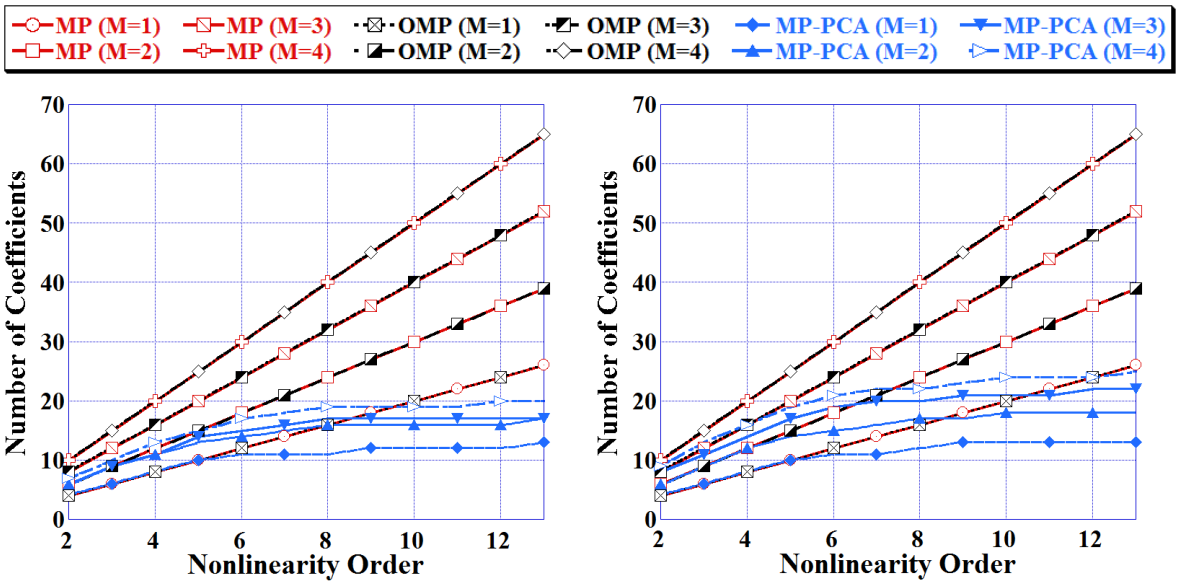

(a) (b)

Figure 3.7: Number of Coefficients required for continuous Class-AB PA inverse modeling: (a) WCDMA signal and (b) LTE signal.

ACEPR is metric for out-of-band modeling performance in frequency domain. It is defined as a ratio of error power in a bandwidth adjacent (left or right or both) to the main channel power [79]. It is given as follows:

$$\text{ACEPR} = \frac{1}{2}\left(\frac{\int_{f_c-\Delta f-\frac{\text{BW}}{2}}^{f_c-\Delta f+\frac{\text{BW}}{2}} |E(f)|^2 df + \int_{f_c+\Delta f-\frac{\text{BW}}{2}}^{f_c+\Delta f+\frac{\text{BW}}{2}} |E(f)|^2 df}{\int_{f_c-\frac{\text{BW}}{2}}^{f_c+\frac{\text{BW}}{2}} |Y_{meas}(f)|^2 df}\right) \tag{3.10}$$

where f_c is the carrier frequency, BW is the bandwidth, Δf is the frequency offset from the carrier frequency, $E(f)$ is the discrete fourier transform of error $e(n)$ and $Y_{meas}(f)$ is the discrete fourier transform of measured output $y_{meas}(n)$.

Figure 3.6 shows that ACEPR (dBc) results are nearly same for all three models for memory depth of M=1 to M=4 and nonlinearity order of K=2 to K=13 respectively.

3.5.3 Computational Complexity

In MP model and OMP model, the number of coefficients increases linearly with an increment in nonlinearity order K and memory depth M. The Number of coefficients in MP model and OMP model are $(M+1)(K)$ [23–25]. Figure 3.7 shows that the number of coefficients are reduced in MP-PCA model with respect to MP model and OMP model for

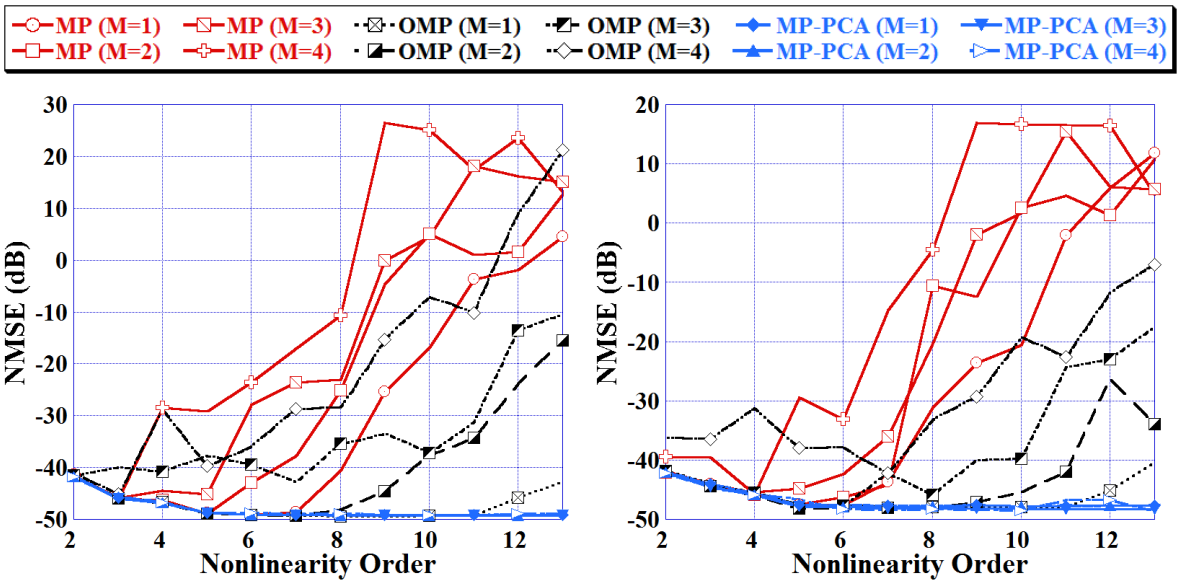

(a) (b)

Figure 3.8: NMSE performances for 16-bit fixed-point calculation of continuous Class-AB PA inverse modeling: (a) WCDMA signal and (b) LTE signal.

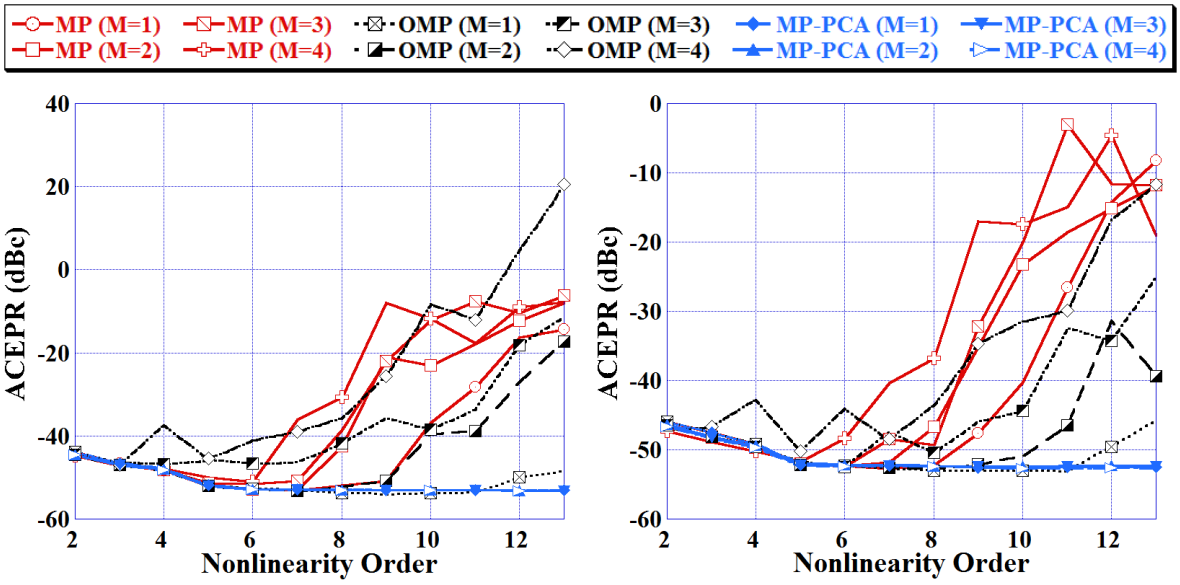

(a) (b)

Figure 3.9: ACEPR performances for 16-bit fixed-point calculation of continuous Class-AB PA inverse modeling: (a) WCDMA signal and (b) LTE signal.

memory depth of M=1 to M=4 and nonlinearity order of K=2 to K=13 respectively. These results are for T=99.99999999%. As the number of coefficients decreases, it would result in a decrease in the size of observation matrix and thus decrease in computation complexity for coefficient extraction.

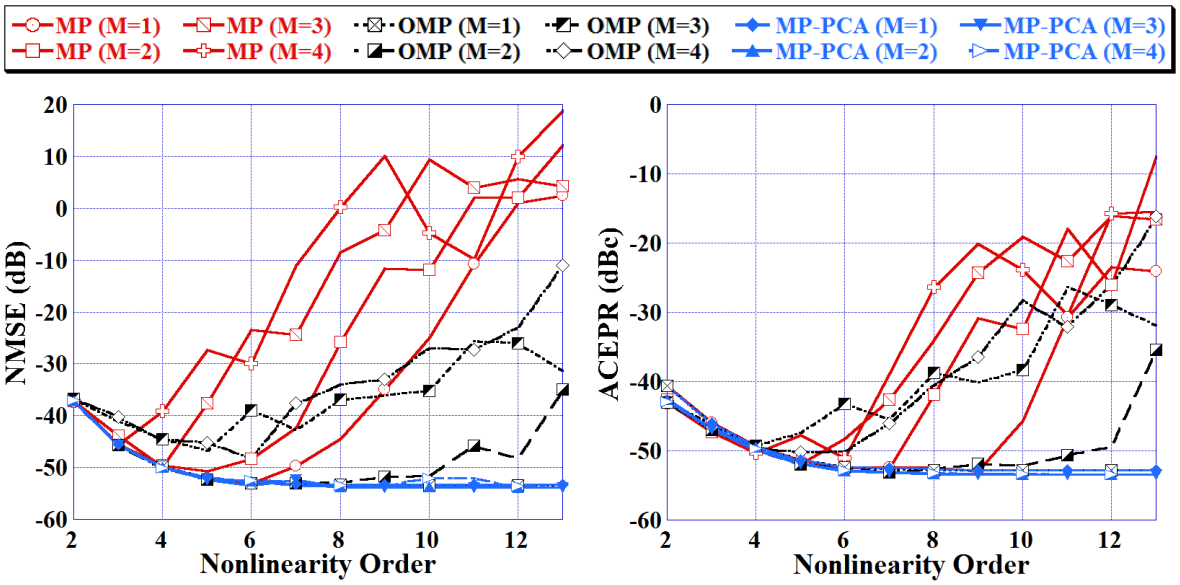

(a) (b)

Figure 3.10: (a) NMSE and (b) ACEPR performances for 16-bit fixed-point calculation of ZX60-V63+ PA inverse modeling for WCDMA signal.

3.5.4 Effect of Fixed-Point Arithmetic at different bit-resolutions

In FPGA, the number of required LUTs depends on the memory size. Memory size required by a model depends on the size of observation (predistorter) matrix and bit resolution [45].

$$Memory\ Size = Matrix\ Size \times Bit\ Resolution \tag{3.11}$$

Earlier in section 3.5.2, MP, OMP and MP-PCA modeling are performed in 64-bit double floating-point DSP. NMSE and ACEPR performances are nearly same for all the three models. In this section, inverse PA modeling performance at different fixed-point bit resolutions is investigated.

When MP, OMP and MP-PCA modeling is performed in 16-bit word length fixed-point DSP. MP-PCA model showed superiority over the MP model and OMP model. Figure 3.8(a) and Figure 3.8(b) shows the NMSE (dB) results for Continuous Class-AB PA inverse modeling of WCDMA signal and LTE signal, when 16-bit fixed-point calculation is performed. In MP-PCA model, NMSE (dB) is decreasing as nonlinearity order K is increasing for both signals. Whereas in MP model and OMP model, NMSE starts increasing sharply as K is increasing from K=7 to K=13 for both the signals.

Figure 3.9(a) and Figure 3.9(b) shows the ACEPR (dBc) results for Continuous Class-AB PA inverse modeling of WCDMA signal and LTE signal when 16-bit fixed-point calculation

Table 3.2: Inverse PA Modeling performances for M=4 and K=7

Model	**WCDMA Signal**				**LTE Signal**			
	NMSE (dB)		**ACEPR (dBc)**		**NMSE (dB)**		**ACEPR (dBc)**	
	64-bit	**16-bit**	**64-bit**	**16-bit**	**64-bit**	**16-bit**	**64-bit**	**16-bit**
MP	-49.38	-17.05	-53.29	-36.10	-49.01	-14.65	-53.60	-40.26
OMP	-49.38	-28.68	-53.29	-38.98	-49.01	-42.23	-53.60	-48.39
GMP	-49.68	19.88	-53.82	-7.71	-49.38	32.58	-54.23	-1.17
MP-PCA	-49.28	-48.84	-53.18	-52.96	-48.92	-48.35	-53.50	-52.43
OMP-PCA	-49.30	-49.29	-53.17	-53.17	-48.98	-48.46	-53.63	-52.85
GMP-PCA	-49.34	-43.92	-53.34	-52.91	-48.85	-48.09	-53.35	-52.45

Table 3.3: Comparison of FPGA's Memory Resource Utilization

	WCDMA Signal						**LTE Signal**					
	MP	**MP-PCA**	**OMP**	**OMP-PCA**	**GMP**	**GMP-PCA**	**MP**	**MP-PCA**	**OMP**	**OMP-PCA**	**GMP**	**GMP-PCA**
No. of Coeff.	35	18	35	25	175	31	35	22	35	29	175	45
Matrix Size	2.29 $\times 10^6$	1.18 $\times 10^6$	2.29 $\times 10^6$	1.64 $\times 10^6$	11.47 $\times 10^6$	2.03 $\times 10^6$	2.29 $\times 10^6$	1.44 $\times 10^6$	2.29 $\times 10^6$	1.90 $\times 10^6$	11.47 $\times 10^6$	2.95 $\times 10^6$
Bit-Res.	24	16	24	16	32	16	24	16	24	16	32	16
Memory Size (MB)	6.88	2.36	6.88	3.28	45.88	4.06	6.88	2.88	6.88	3.80	45.88	5.90

is performed. In MP-PCA model, ACEPR (dBc) is decreasing as nonlinearity order K is increasing for both the signals. Whereas in MP model and OMP model, ACEPR starts increasing sharply as K is increasing from K=7 to K=13 for both the signals.

To demonstrate the effect of fixed-point calculation at different PAs, we have also used ZX60-V63+ PA. Figure 3.10(a) and Figure 3.10(b) shows the NMSE (dB) and ACEPR (dBc) results for ZX60-V63+ PA inverse modeling of WCDMA signal when 16-bit fixed-point calculation is performed. In MP-PCA model, NMSE (dB) and ACEPR (dBc) are decreasing as nonlinearity order K is increasing for WCDMA signal, whereas in MP model and OMP model, both NMSE and ACEPR starts increasing sharply as K is increasing from K=7 to K=13 for WCDMA signal.

Table 3.2 compares the performance of MP model, OMP model, GMP model and PCA models in 64-bit double floating point with 16-bit fixed point calculation for continuous Class-AB PA (M=4 and K=7). In MP-PCA model, 64-bit double floating point and 16-bit fixed point calculation have nearly same NMSE and ACEPR values. While in the cases of MP model, OMP model and GMP model; NMSE and ACEPR values are degraded when the 16-bit fixed-point calculation is performed.

Figure 3.11(a) and Figure 3.11(b) shows the NMSE (dB) and ACEPR (dBc) results for different bit (16, 24, 32, 64) resolutions of continuous Class-AB PA inverse modeling of WCDMA signal for M=4 and K=7. MP-PCA and OMP-PCA models have similar performance at 16-bit resolution, however OMP-PCA model requires more number of mathematical operations (such as addition and multiplication) than the MP-PCA model. OMP and MP models performance converge to MP-PCA performance at 24-bit whereas GMP model performances converge at 32-bit. Similarly, Figure 3.11(c) and Figure 3.11(d) shows the NMSE (dB) and ACEPR (dBc) results for different bit resolutions of continuous Class-AB PA inverse modeling of LTE signal for M=4 and K=7. Again, MP-PCA and OMP-PCA models have similar performance at 16-bit resolution. OMP and MP models performance converge to MP-PCA performance at 24-bit whereas GMP model performances converge at 32-bit.

Table 3.3 shows the comparison of FPGA's memory resource utilization for continuous Class-AB PA inverse modeling of WCDMA signal and LTE signal (M=4, K=7, and L=65536). MP-PCA model shows good linearization performance at 16-bit with lesser number of coefficients than all other models, therefore memory size and number of LUTs required by the MP-PCA model are lesser.

Figure 3.12(a) and Figure 3.12(b) shows Power Spectrum Density (PSD) of measured output (PA output), and error $e(n)$ of MP model, OMP model and MP-PCA model for M=4 and K=7 of continuous Class-AB PA when 16-bit fixed-point calculation and 64-bit double floating-point is performed. As evident from the graph MP-PCA model's error performance is similar to MP model and OMP model's error performances in the 64-bit double floating-point calculation, whereas MP-PCA model's error performance is better than MP model and OMP model's error performances in 16-bit fixed-point calculation. Based on modeling performances, according to indirect DPD method, it is anticipated that the effect will be visible in predistortion performance too.

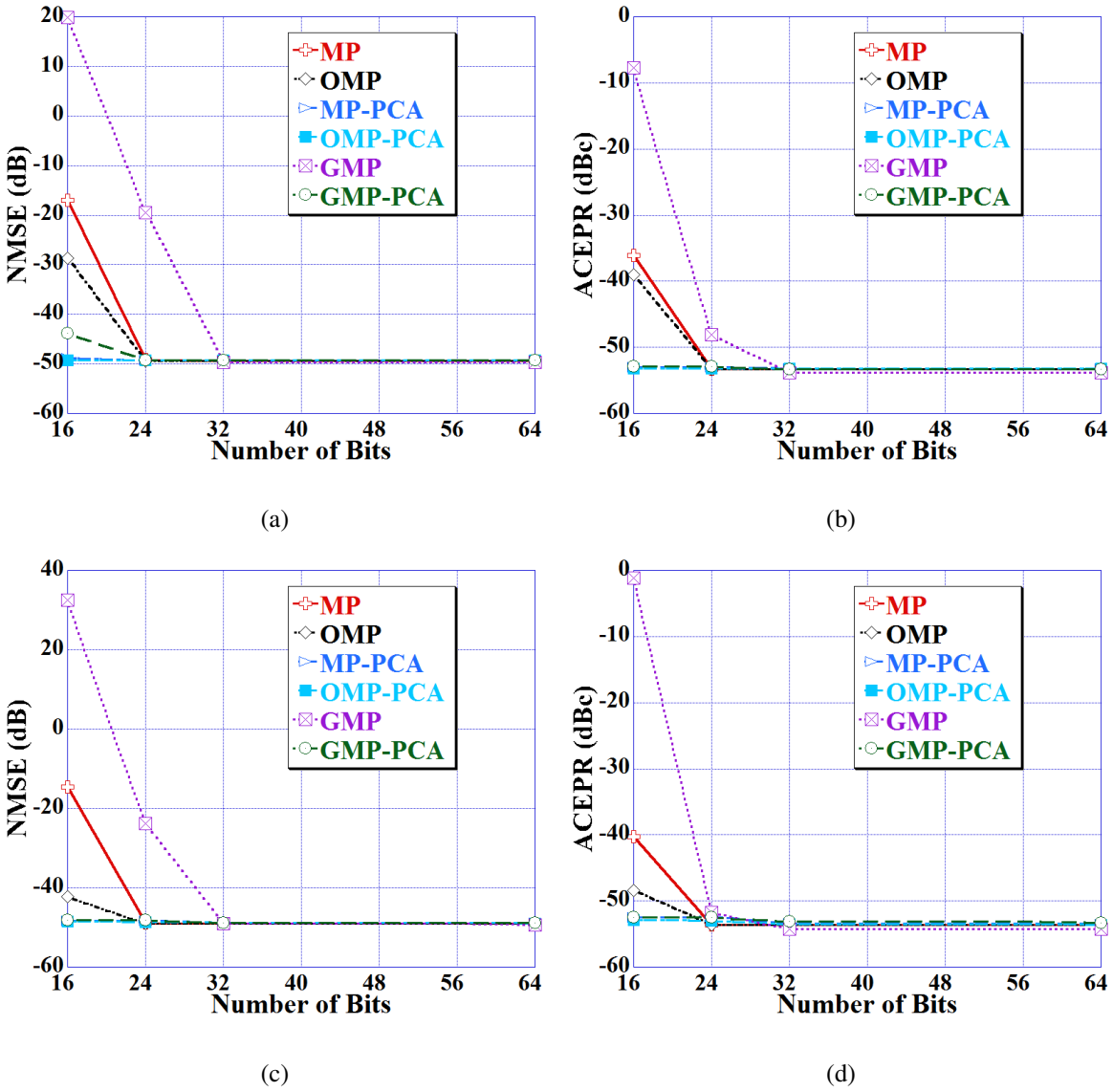

Figure 3.11: Performances for different bit resolutions of continuous Class-AB PA inverse modeling: (a) NMSE performances for WCDMA signal, (b) ACEPR performances for WCDMA signal, (c) NMSE performances for LTE signal and (d) ACEPR performances for LTE signal.

3.6 Digital Predistortion Results

Linearization performance of DPD technique is measured in terms of Adjacent Channel Power Ratio (ACPR) and NMSE. NMSE is the normalized mean square error between the transmitted and received signals [30]. It is measured for an in-band transmission error because the square of a signal provides higher deviation and hence higher correction for high power data. As useful signal is within band, correction is applied mostly on in-band data. It also provides error deviation for both negative and positive error. Also the square of an error

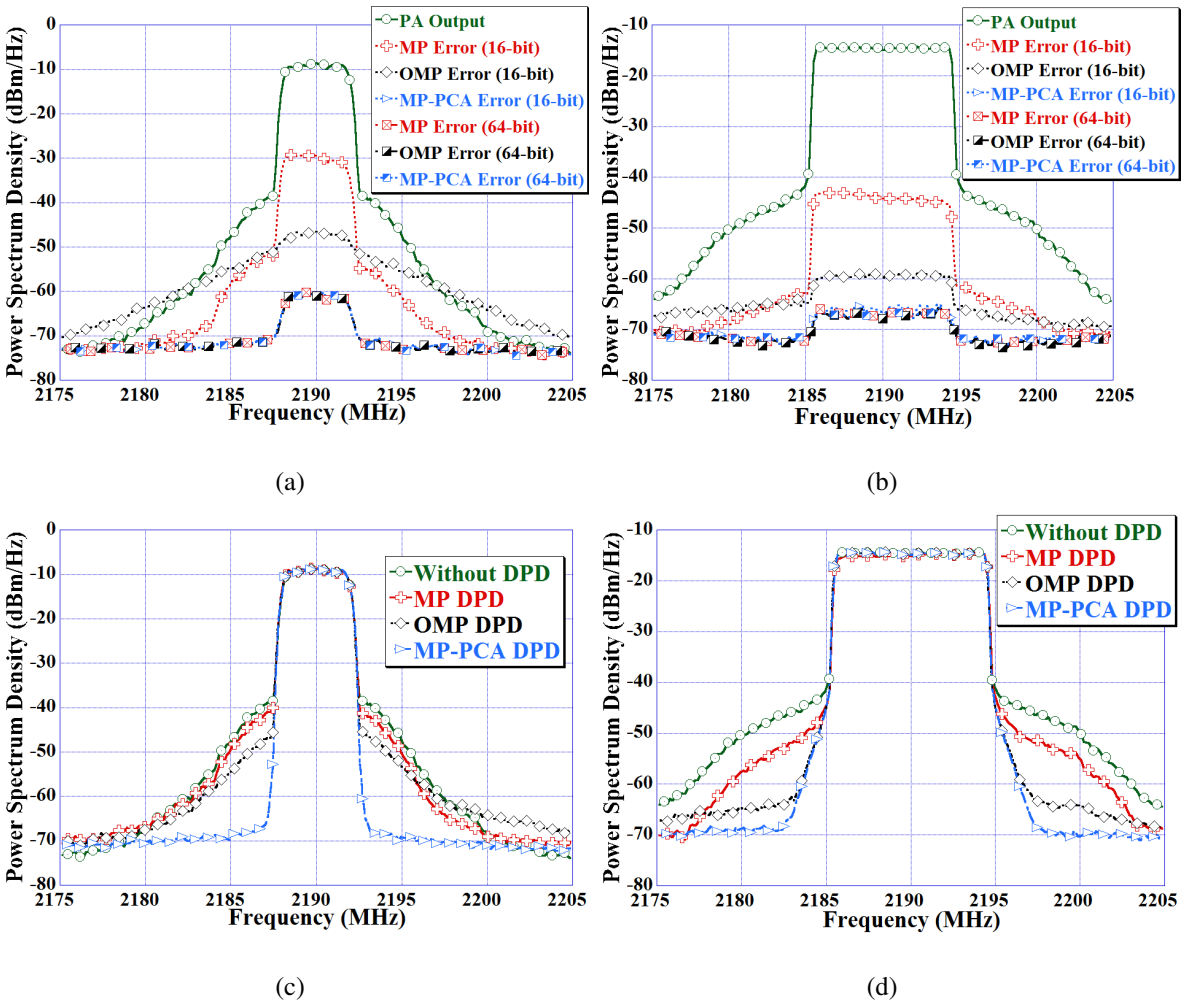

Figure 3.12: PSD of MP model, OMP model and MP-PCA model errors and DPD: (a) Error Spectra for 16-bit fixed-point and 64-bit double floating-point calculation of WCDMA Signal, (b) Error Spectra for 16-bit-fixed-point and 64-bit double floating-point calculation of LTE signal, (c) DPD Spectra for 16-bit fixed-point calculation of WCDMA signal and (d) DPD Spectra for 16-bit fixed-point calculation of LTE signal.

Table 3.4: MP DPD, OMP DPD and MP-PCA DPD performances for 16-bit fixed point calculation

	WCDMA Signal				**LTE Signal**			
	Without DPD	**MP DPD**	**OMP DPD**	**MP-PCA DPD**	**Without DPD**	**MP DPD**	**OMP DPD**	**MP-PCA DPD**
NMSE (dB)	-11.51	-18.33	-26.27	-37.11	-11.22	-21.54	-34.08	-36.90
ACPR (dBc)	-30.59	-32.12	-38.46	-53.27	-27.26	-31.23	-47.74	-52.14

have one global minima. It is given by

$$\text{NMSE (dB)} = 10\log_{10}\left(\frac{\sum_{n=1}^{L}|y_{meas}(n)-x(n)|^2}{\sum_{n=1}^{L}|x(n)|^2}\right) \tag{3.12}$$

where $x(n)$ is the complex baseband input signal and $y_{meas}(n)$ is the measured baseband output.

ACPR is defined as a ratio of adjacent channel power (left or right or mean of both) to the main channel power in the frequency domain [30]. It is measurable for an out-of-band transmission error and spectral regrowth. It is given as follows:

$$\text{ACPR} = \frac{1}{2}\left(\frac{\int_{f_c-\Delta f-\frac{BW}{2}}^{f_c-\Delta f+\frac{BW}{2}}|Y(f)|^2df + \int_{f_c+\Delta f-\frac{BW}{2}}^{f_c+\Delta f+\frac{BW}{2}}|Y(f)|^2df}{\int_{f_c-\frac{BW}{2}}^{f_c+\frac{BW}{2}}|Y(f)|^2df}\right) \tag{3.13}$$

where Δf is the frequency offset from the carrier frequency, BW is the bandwidth, f_c is the carrier frequency, and $Y(f)$ is the discrete fourier transform of measured baseband output $y_{meas}(n)$.

Figure 3.12(c) and Figure 3.12(d) shows PSD of MP model, OMP model and MP-PCA model DPD for M=4 and K=7 of continuous Class-AB PA when the 16-bit fixed-point calculation is performed. It is clear from the graph, MP-PCA model DPD performance is better than MP model and OMP model DPD performances.

Table 3.4 shows the DPD performances of the models in terms of ACPR and NMSE for M=4 and K=7 of continuous Class-AB PA when the 16-bit fixed-point calculation is performed. In MP-PCA DPD, the NMSE improves from -11.51 dB to -37.11 dB and -11.22 dB to -36.90 dB for WCDMA and LTE signals respectively i.e. improvement of 25.6 dB and 25.68 dB. In MP DPD, the NMSE improves by 6.82 dB and 10.32 dB for WCDMA and LTE signals respectively. In OMP DPD, the NMSE improves by 14.76 dB and 22.86 dB for WCDMA and LTE signals respectively.

In MP-PCA DPD, the ACPR improves by 22.68 dBc and 24.88 dBc WCDMA and LTE signals respectively. In MP DPD, the ACPR improves by 1.53 dBc and 3.97 dBc for WCDMA and LTE signals respectively. In OMP DPD, the ACPR improves by 7.87 dBc and 20.48 dBc for WCDMA and LTE signals respectively.

It is evident that with 16-bit fixed-point calculation, MP and OMP DPD does not perform as good as MP-PCA DPD.

3.7 Conclusion

In this chapter, benefits of using PCA on the single-band MP model observation (predistorter) data matrix as opposed to various polynomial based models are investigated. The results show that the proposed MP-PCA requires lesser memory size and number of LUTs in FPGA. MP-PCA has comparable linearization performance in terms of NMSE and ACEPR in high precision (64-bit) double floating-point calculation but with a reduced number of coefficients, condition number and dispersion coefficient with the conventional MP model and OMP model. Inverse modeling performances in terms of NMSE and ACEPR were better in PCA based model when the 16-bit fixed-point calculation was performed. Also the linearization performances in terms of NMSE and ACPR were better in PCA based model when the 16-bit fixed-point calculation was performed. Thus the proposed model utilizing PCA allows implementation of digital predistortion scheme in low-cost FPGA as compared to MP model, OMP model, and GMP models.

The next chapter deals with the the complexity and numerical stability of DPD nodels for CA signals. A novel DPD technique is presented for intra-band and inter-band CA signals.

Chapter 4

DPD technique for low resource consumption using Carrier Aggregated 4G/5G Signals

4.1 Introduction

In the last 2 decades, DPD technique had emerged as an effective technique for linearization of PA using already available FPGA or digital signal processor in the base-station. The major challenges in the implementation of DPD are wider bandwidth support, multi-band operation, power consumption and hardware cost of digital signal processor or FPGA. Wide bandwidth signals tend to stimulate the memory effects within the PA requiring memory correction to be included in the DPD [66]. However, if in the pursuit of additional memory correction the number of basis waveforms used is over-specified relative to the measurable output signal bandwidth, the estimation of the memory coefficients will be ill-conditioned. There are non-linear DPD models available for both single-band and concurrent dual-band PA linearization. The better conditioning of these DPD models would result in lower-bit FPGA implementation. Moreover, a lower-bit FPGA would eventually reduce the implementation cost.

In the previous chapter, PCA is proposed for 16-bit fixed-point FPGA implementation of DPD for single-carrier LTE and WCDMA signals [71]. This chapter proposes use of ICA for enhacing the numerical stability of the state-of-the-art DPD models for intra-band and inter-band CA signals [86, 87]. Figure 4.1 shows that the ultra-wideband [80–82] and multi-

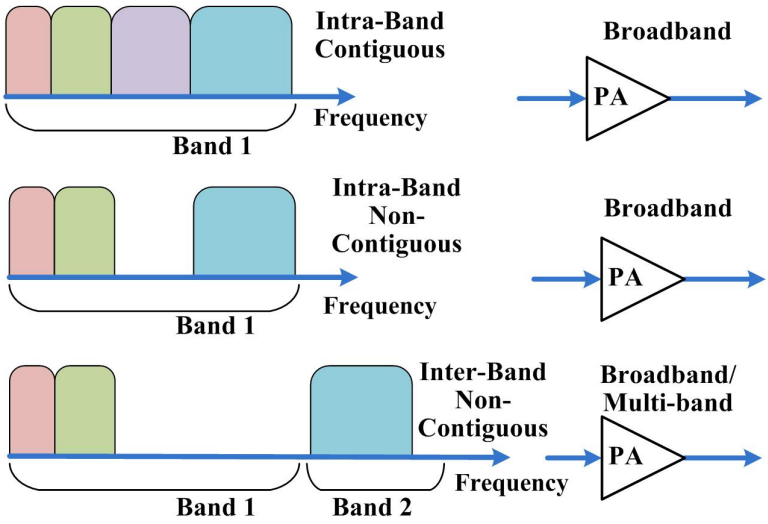

Figure 4.1: CA of signals for efficient utilization of spectrum.

band [83,84] PAs are needed to meet CA's high bandwidth and complex digital modulation's PAPR requirements. The high PAPR of CA signal and multi-band operation gives rise to nonlinear distortions like CMDs and IMDs in PA's output.

PCA is generally used for up to second-order statistics while ICA can be used for higher-order statistics [85]. ICA technique is used to separate different signals. When data becomes very noisy due to the non-linear mixing of signals then ICA technique is preferred over PCA. This situation is similar to the non-linear distortions generated by PA for intra-band and inter-band CA signals.

ICA technique is proposed for 12-bit fixed-point FPGA implementation of DPD for intra-band and inter-band CA signals. The application of ICA technique upon MP model reduces model complexity and improves numerical stability of the DPD model for CA signals. Thus proposed MP-ICA requires least FPGA's memory size, reduced coefficient extraction burden and reduced complexity.

The rest of the chapter is organized as follows: Section 4.2 proposes the application of ICA to any model where coefficients are linear with respect to the basis function without loss of generality e.g. MP model. Section 4.3 describes the measurement testbeds used for DPD of intra-band and inter-band CA signals respectively. Section 4.4 provides the results of inverse modeling and DPD of the models, effect of lower-bit fixed-point arithmetic and efficiency. Section 4.5 presents the conclusion of the chapter.

4.2 Proposed Independent Component Analysis (ICA) method for DPD

The non-linear distortions generated by PA for intra-band and inter-band CA signals results in intermixing of in-band carrier components (CC) of CA signal as well as in-band IMDs. The output of PA becomes very noisy and it does not follow second-order statistics like a gaussian distribution [88]. The steps followed by fast ICA technique are as follows [85]:

1. Let $\mathbf{U}$ is a $(M+1)(K)\times L$ observation data matrix
   where, L is number of input samples.

2. Center the data matrix $\mathbf{U}$ around its mean value
   $\mathbf{U} \leftarrow \mathbf{U} - \mathrm{E}\{\mathbf{U}\}$

3. Whiten the data $\mathbf{U}$ matrix
   $\mathbf{W} = \mathbf{Q}\mathbf{\Lambda}^{-1/2}\mathbf{Q}^H\mathbf{U}$
   where, $\mathbf{Q}\mathbf{\Lambda}\mathbf{Q}^H = \mathrm{E}\left\{\mathbf{U}\mathbf{U}^H\right\}$

4. Initialize a random matrix $\mathbf{p}$ whose dimension is $S\times(M+1)(K)$ and $\mathbf{p}$ is such that
   $\|\mathbf{p}\| = 1$

5. Update $\mathbf{p}$

   a. $\mathbf{p} \leftarrow \mathrm{E}\{\mathbf{W}f(\mathbf{p}\mathbf{W})\} - \mathrm{E}\{f'(\mathbf{p}\mathbf{W})\}\mathbf{p}$
      where, $f(y) = y^3$

   b. $\mathbf{p} \leftarrow \mathbf{p}/\|\mathbf{p}\|$

6. The independent component matrix
   $\mathbf{V} = (\mathbf{p}\mathbf{W})^T$

7. $\mathbf{y} = \mathbf{V}\mathbf{D}$
   where $\mathbf{D} = [d_0, d_1, \cdots, d_s]^T$ is a $S\times 1$ vector of ICA-based coefficients and can be calculated using the pseudo-inverse method.

8. Using the pseudo-inverse method $\hat{\mathbf{D}}$ is extracted as
   $\hat{\mathbf{D}} = \left(\mathbf{V}^H\mathbf{V}\right)^{-1}\mathbf{V}^H\mathbf{y} = \mathbf{V}^+\mathbf{y}$

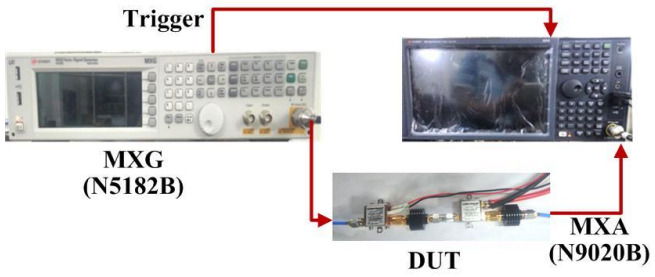

Figure 4.2: Measurement Testbed I.

After extracting the coefficients, the inverse modeling performance is evaluated in terms of NMSE and ACEPR [79].

For the case of MP model, the dimensions of the observation matrix $\mathbf{V}$ of MP-ICA model is reduced from the $L{\times}(M{+}1)(K)$ to $L{\times}S$. The pruning percentage $(1{-}S/((M{+}1)(K)))\times 100$ of MP-ICA is selected such that MP-ICA's inverse modeling performance NMSE must be nearly equal to MP's NMSE performance.

It is to be noted that the proposed method is significantly different from the PCA method. PCA projects the data along the eigen vectors, which have the highest variance. The eigen value of the covariance matrix of the observation matrix measures the variance of the data along an eigen vector. The steps followed by PCA technique are already defined in previous chapter. It is applied upon MP and 2D-MP model and termed as MP-PCA and 2D-MP-PCA. The pruning percentage of MP-PCA is selected such that MP-PCA's inverse modeling performance NMSE must be nearly equal to MP's NMSE performance.

PCA technique uses covariance i.e. it is based on second-order statistics/Gaussian distribution. While Fast-ICA uses fourth-order statistics i.e. it identifies components for non-gaussian signals too. Therefore, PCA technique is inadequate and ICA can be applied to identify the independent components of intermixed CA noisy signals. The observation matrix $\mathbf{V}$ of MP-ICA does not have nonlinear geometric terms thus its condition number would be reduced leading to numerical stability of the solution.

4.3 Measurement Testbed

We have used two measurement testbed. First measurement testbed is used for intra-band contiguous and intra-band non-contiguous CA LTE signals. It consists of vector signal generator (VSG), PAs, and vector signal analyzer (VSA). Second measurement testbed is used

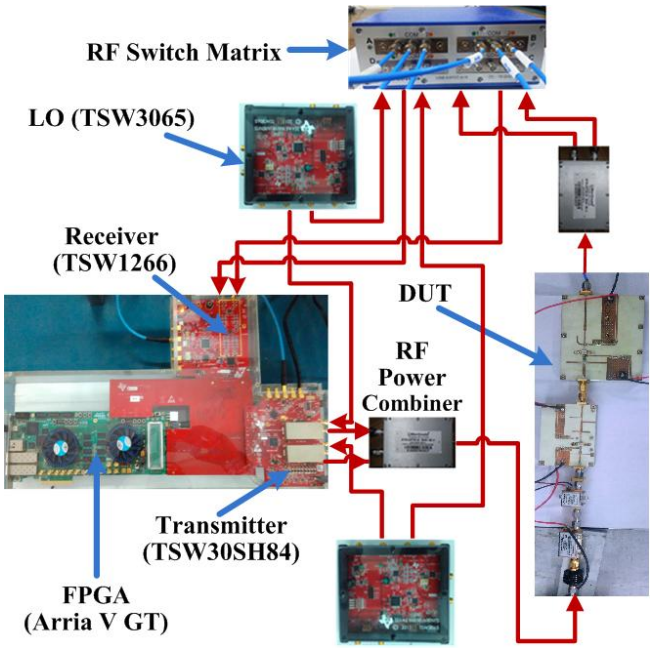

Figure 4.3: Measurement Testbed II.

for inter-band non-contiguous CA LTE signals. It is a FPGA-based transceiver.

4.3.1 Measurement Testbed for Intra-Band CA

Figure 4.2 shows the first measurement testbed. It consists of a Keysight "MXG N5182B" VSG), Keysight "MXA N9020B" VSA, two mini-circuit PAs and attenuators.

In intra-band contiguous case, 111 CA LTE signal contains CCs of 3 MHz, 5 MHz, and 10 MHz. 111 CA LTE signal has a bandwidth of 18 MHz, PAPR of 11.27 dB and it is transmitted at 2 GHz with a sampling rate of 92.16 Msps.

In intra-band non-contiguous case, 1101 CA LTE signal contains CCs of 3 MHz, 5 MHz and 10 MHz. There is a spacing of 20 MHz between second and third CCs. 1101 CA LTE signal has a bandwidth of 38 MHz, PAPR of 11.39 dB and it is transmitted at 2 GHz with a sampling rate of 184.32 Msps.

The RF signal generated by VSG are passed through two mini-circuit PAs in cascade. These two PAs are ZX60-V63+ and ZX60-V82+. ZX60-V63+ PA and ZX60-V82+ PA have 17.8 dBm and 20 dBm output power respectively at 1 dB gain compression. ZX60-V63+ PA and ZX60-V82+ PA have output frequency ranging from 0.05 to 6 GHz and 0.02 to 6 GHz respectively. The output of PA is attenuated and then captured at VSA. VSA is synchronized with VSG using triggering. The output signal captured at VSA is down-converted into a

baseband signal. The baseband output signal is then processed using the Matlab software.

4.3.2 Measurement Testbed for Inter-Band CA

Figure 4.3 shows the second measurement testbed. This concurrent dual-band setup is used for inter-band non-contiguous CA LTE signals. The measurement testbed II consists of an Altera Arria V GT FPGA, dual channel transmitter (TSW30SH84), RF switch matrix, transmitter observation receiver (TSW1266), ZX60-2411BM-S+ and ZX60-V62+ PAs from Mini-Circuits, 15–W driver PA, 25–W class AB PA, local oscillators (LO) (TSW3065), ZN2PD2-50-S+ RF power combiner/splitter from Mini-Circuits and attenuators.

The pre-programmed Altera Arria V GT FPGA transmits the data to the dual-channel transmitter (TSW30SH84) at a sampling frequency of 307.2 MHz. The DAC further interpolates the data by a factor of 4 to a sampling rate of 1228.8 MHz. The TRF3705 up-converts the output signal from DAC to RF using LO (TSW3065). From the first RF channel output of transmitter, 11 CA (3 MHz, 5 MHz) LTE signal of bandwidth 8 MHz and PAPR of 9.61 dB is transmitted at 1.75 GHz (lower band or LB). From the second RF channel output of transmitter, single carrier LTE signal of bandwidth 10 MHz and PAPR of 11.15 dB is transmitted at 2.05 GHz (upper band or UB). These two RF signals are combined using a RF power combiner and passed through PAs.

ZX60-2411BM-S+, ZX60-V62+ and 15–W PAs are used as driver PAs to 25–W class AB PA. ZX60-2411BM-S+ PA and ZX60-V62+ PA have 24 dBm and 19 dBm output power respectively at 1 dB gain compression. ZX60-2411BM-S+ PA and ZX60-V62+ PA have output frequency ranging from 0.8 to 2.4 GHz and 0.05 to 6 GHz respectively. 15–W driver-PA is biased at a drain voltage of 28 V and drain current of 90 mA. 25–W Class-AB is a gallium nitride (GaN) based PA, biased at a drain voltage of 28 V and drain current of 134 mA.

RF switch matrix is used for proper selection of band (LB or UB) and its corresponding LO. The selected RF output and LO are then provided to the receiver (TSW1266) from the RF switch matrix. The output signal captured at receiver is down-converted into a baseband signal by ADC at a sampling frequency of 614.4 MHz. A 10 MHz reference clock is provided by LO to synchronize both transmitter and receiver.

Table 4.1: Numerical Stability metrics for Intra-Band

Case		**MP**	**OMP**	**MP-PCA**	**MP-ICA**
Contiguous	**Cond. No. (dB)**	80.76	63.08	49.63	3.64
	Disp. Coeff. (dB)	52.74	35.74	28.11	24.41
	No. of Coeff.	45	45	32	32
Non-Contiguous	**Cond. No. (dB)**	80.49	60.93	48.98	3.60
	Disp. Coeff. (dB)	56.12	38.57	29.55	25.90
	No. of Coeff.	45	45	32	32

4.4 Results

4.4.1 Inverse Modeling Results

Table 4.1 shows the metrics for numerical stability of different inverse models for both intra-band contiguous and intra-band non-contiguous CA LTE signals. The MP-ICA model has least condition number and dispersion coefficient with respect to other models. This indicates that MP-ICA model is more numerically stable than other non-linear inverse models. The pruning percentage of coefficients for ICA and PCA is 30%.

Figure 4.4(a) and Figure 4.4(b) shows the I and Q value of coefficients of MP-ICA model and MP-PCA model of Intra-band contiguous CA LTE signal and Intra-band non-contiguous CA LTE signal respectively. As shown in Figure 4.4, the I and Q values of coefficients of MP-PCA model are much dispersed as compared to the I and Q values of coefficients of MP-ICA model, that's why in the figure coefficients of MP-ICA are seen to be around zero. For better visualization, the absolute of coefficients are also plotted in semi logarithmic scale in Figure 4.4(c) and Figure 4.4(d).

In this section, the coefficient extraction is performed in 64-bit double floating-point DSP. Figure 4.5 and Figure 4.6 shows the inverse modeling performance of MP-ICA model for CA signals with respect to change in memory depth M and nonlinearity order K. M is varied from 1 to 4 and K is varied from 3 to 13. It can be observed from the above Figure 4.5 that for two different test signals, although convergence curves shape may differ slightly, final convergence values of K and M values are similar, i.e. K=9 and M=4. Therefore, once K and M values are found iteratively, they define order and memory depth of the PA and are

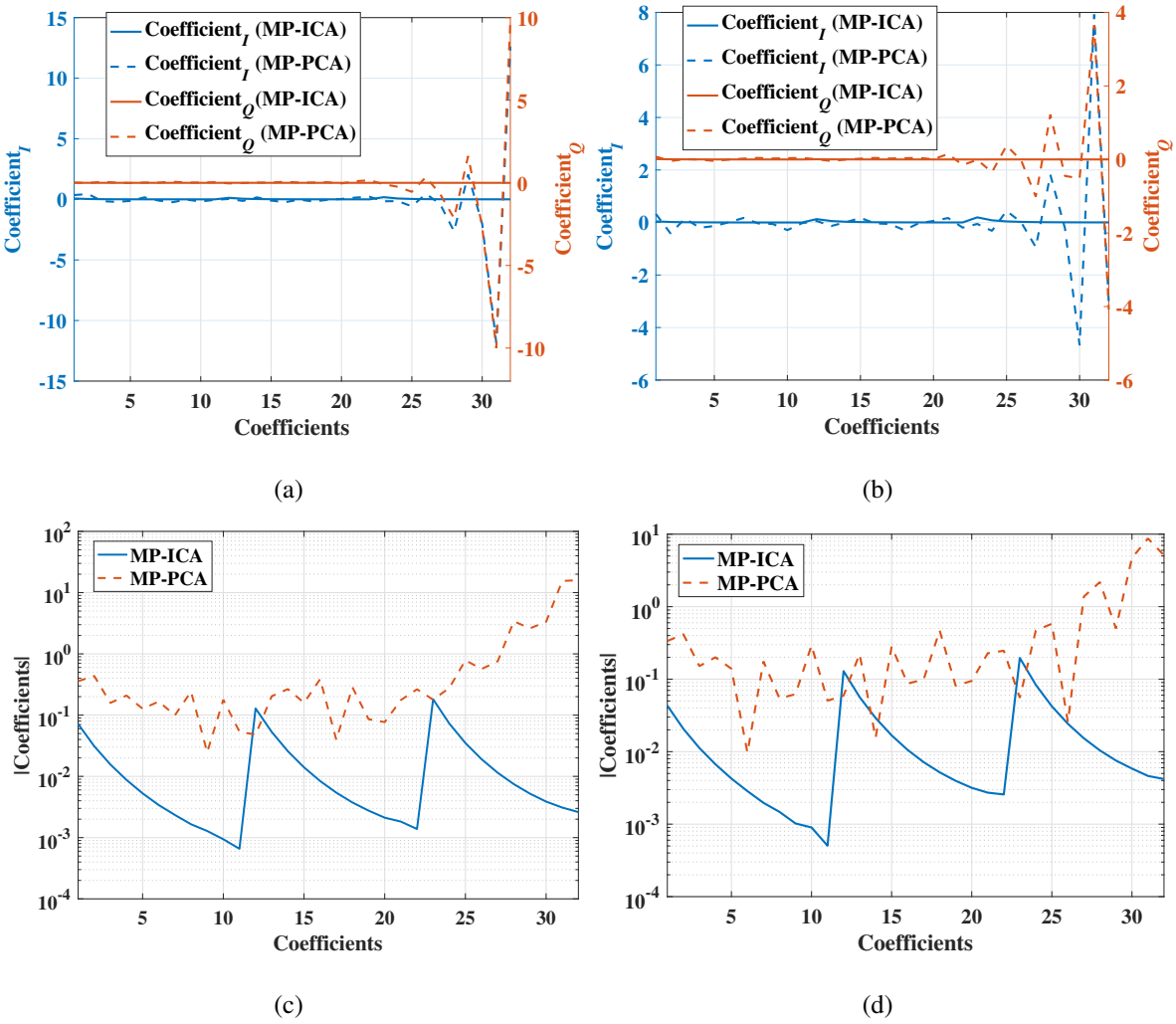

Figure 4.4: (a) I and Q coefficients of MP-ICA model and MP-PCA model of Intra-band contiguous CA LTE signal, (b) I and Q of coefficients of MP-ICA model and MP-PCA model of Intra-band non-contiguous CA LTE signal, (c) Absolute value of coefficients of MP-ICA model and MP-PCA model of Intra-band contiguous CA LTE signal and (d) Absolute value of coefficients of MP-ICA model and MP-PCA model of Intra-band non-contiguous CA LTE signal.

kept constant. However while topology of model is fixed, coefficients are updated to keep track of small fluctuations.

Table 4.2 shows inverse modeling performance for intra-band contiguous and intra-band non-contiguous CA LTE signals (L= 184320, K=9 and M=4) of all the DPD models. From Table 4.2, it is clear that all the models have nearly same NMSE and ACEPR values at 64-bit double floating-point DSP.

Table 4.3 shows the metrics for numerical stability of different inverse models for inter-band non-contiguous CA LTE signals. The 2D-MP-ICA inverse model has least condition

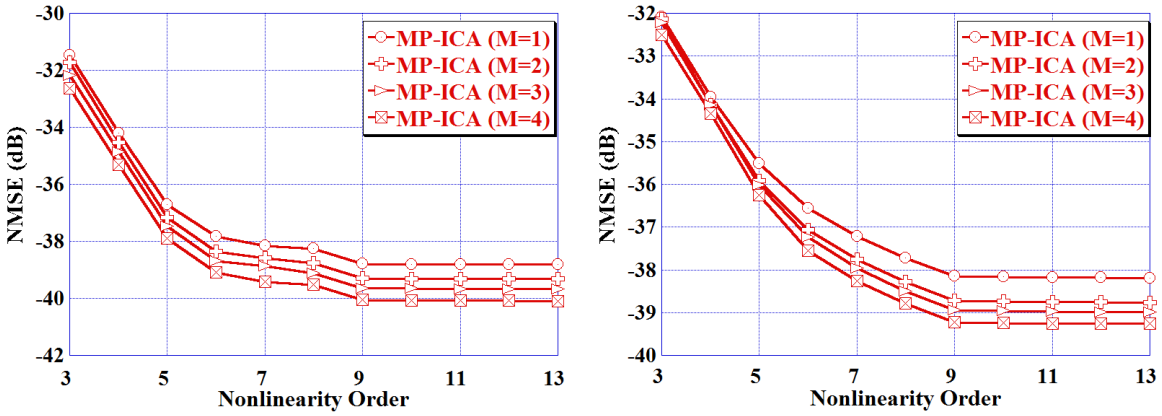

(a) (b)

Figure 4.5: Effect of Memory Depth (M) and Nonlinearity Order (K) on inverse modeling for (a) Intra-band contiguous CA LTE signal and (b) Intra-band non-contiguous CA LTE signal.

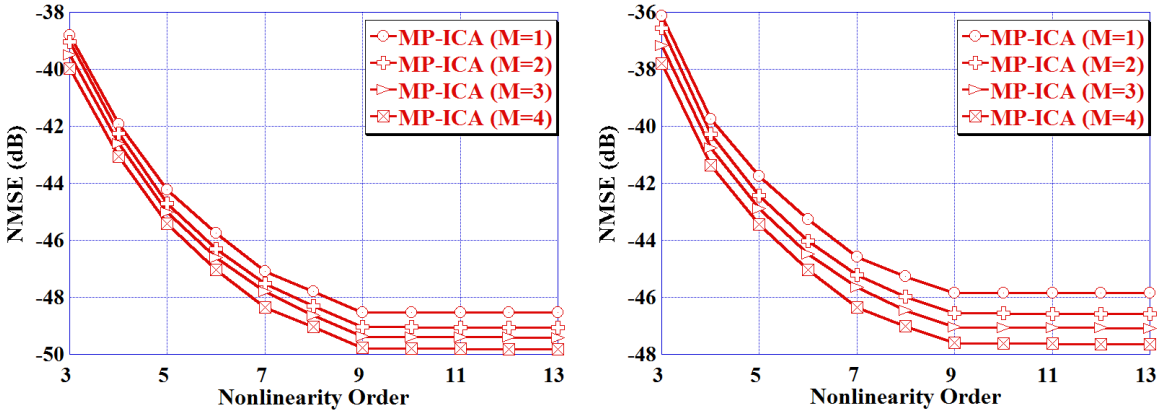

(a) (b)

Figure 4.6: Effect of Memory Depth (M) and Nonlinearity Order (K) on inverse modeling for (a) LB of Inter-band non-contiguous CA LTE signal and (b) UB of Inter-band non-contiguous CA LTE signal.

number and dispersion coefficient with respect to other dual-band inverse models. The pruning percentage of coefficients for dual-band ICA and PCA is 30%. Table 4.4 shows that inverse modeling performance for inter-band non-contiguous CA LTE signals (L= 131072, K=9 and M=4). From Table 4.4, concurrent dual-band inverse models have nearly same NMSE and ACEPR values for their respective bands (LB or UB) at 64-bit double floating-point DSP.

Table 4.2: Effect of different bit-resolutions on Inverse Modeling Performances for Intra-Band

Model	Bit-Res.	Contiguous		Non-Contiguous	
		NMSE (dB)	ACEPR (dBc)	NMSE (dB)	ACEPR (dBc)
MP	12	2.38	-11.12	2.42	-11.12
	16	-4.69	-16.77	-4.58	-13.94
	24	-40.38	-53.26	-38.61	-50.85
	32	-40.51	-56.85	-39.08	-54.15
	64	-40.64	-57.66	-39.25	-54.27
OMP	12	-6.61	-18.64	-8.22	-18.18
	16	-10.28	-23.66	-11.25	-21.25
	24	-40.24	-57.06	-38.47	-53.67
	32	-40.56	-57.17	-39.14	-53.82
	64	-40.64	-57.66	-39.25	-54.27
MP-PCA	12	-33.87	-48.25	-28.80	-43.41
	16	-40.19	-54.23	-38.23	-52.85
	24	-40.33	-56.53	-38.43	-53.52
	32	-40.58	-56.63	-38.81	-53.94
	64	-40.63	-57.07	-39.24	-54.24
MP-ICA	12	-40.43	-57.18	-39.05	-53.02
	16	-40.45	-57.40	-39.07	-52.95
	24	-40.52	-57.61	-39.17	-54.13
	32	-40.62	-57.67	-39.22	-54.21
	64	-40.64	-57.66	-39.25	-54.27

4.4.2 Inverse Modeling Results in lower-bit fixed-point arithmetic

In this section, the coefficient extraction is performed in various different lower-bit fixed-point DSP. When condition number of observation (predistorter) matrix and dispersion of coefficient are large, then applying lower-bit fixed-point arithmetic upon observation matrix and coefficients, would result in numerically unstable solutions.

Table 4.2 also shows inverse modeling performance in 12, 16, 24 and 32 bits for both

Table 4.3: Numerical Stability metric for Inter-Band Non-Contiguous

Model	**LB**			**UB**		
	Cond. No. (dB)	**Disp. Coeff. (dB)**	**No. of Coeff.**	**Cond. No. (dB)**	**Disp. Coeff. (dB)**	**No. of Coeff.**
2D-MP	116.40	52.28	225	115.56	57.69	225
2D-OMP	98.12	37.11	225	102.58	41.52	225
2D-MP-PCA	53.86	38.60	156	53.98	33.95	156
2D-MP-ICA	39.44	33.62	156	39.46	32.07	156

intra-band contiguous and intra-band non-contiguous CA LTE signals. MP-ICA has good NMSE and ACEPR performances even at 12-bit fixed-point resolution due to its low condition number and dispersion coefficient. MP-PCA has unsatisfactory NMSE and ACEPR values at 12-bit fixed-point resolution and converges to MP-ICA performance at 16-bit fixed-point resolution.

Both MP and OMP models have unsatisfactory NMSE and ACEPR values at 12-bit and 16-bit resolutions and converge to MP-ICA performance at 24-bit fixed-point resolution.

Table 4.4 also shows inverse modeling performance in 12, 16, 24 and 32 bits for inter-band non-contiguous CA LTE signals. 2D-MP-ICA has good NMSE and ACEPR values even at 12-bit fixed-point resolution for both the bands due to its low condition number and dispersion coefficient. 2D-MP-PCA has unsatisfactory NMSE and ACEPR values at 12-bit fixed-point resolution and converges to 2D-MP-ICA performance at 16-bit fixed-point resolution.

Both 2D-MP and 2D-OMP models have unsatisfactory NMSE and ACEPR values at 12-bit, 16-bit and 24-bit resolutions and converge to 2D-MP ICA performance at 32-bit fixed-point resolution.

4.4.3 Digital Predistortion Results

The different predistorted signals are generated using coefficients extracted in earlier section 4.4.1 for different models. Table 4.5 shows the DPD results of intra-band contiguous and intra-band non-contiguous case for the predistorted signals generated at 64-bit double floating-point DSP (L=184320, K=9 and M=4). As seen from the Table 4.5, the lineariza-

Table 4.4: Effect of different bit-resolutions on Inverse Modeling Performances for Inter-Band Non-Contiguous

Model	Bit-Res.	LB		UB	
		NMSE (dB)	ACEPR (dBc)	NMSE (dB)	ACEPR (dBc)
2D-MP	12	-0.12	-14.69	-2.26	-23.54
	16	-5.48	-26.67	-6.84	-26.69
	24	-16.30	-35.33	-4.01	-35.64
	32	-49.52	-54.25	-44.76	-52.52
	64	-49.77	-54.31	-47.59	-52.51
2D-OMP	12	-7.14	-27.73	-5.69	-24.65
	16	-9.39	-28.27	-7.55	-28.23
	24	-38.83	-46.77	-40.51	-46.80
	32	-49.11	-53.28	-47.17	-51.95
	64	-49.14	-53.40	-47.29	-52.09
2D-MP-PCA	12	-22.52	-43.46	-25.14	-44.62
	16	-42.43	-48.88	-43.24	-48.62
	24	-47.06	-50.85	-45.65	-50.07
	32	-47.18	-51.04	-45.84	-50.04
	64	-47.33	-51.17	-45.97	-50.10
2D-MP-ICA	12	-47.68	-53.13	-46.00	-51.44
	16	-48.79	-54.21	-46.97	-52.38
	24	-49.53	-54.24	-47.45	-52.40
	32	-49.71	-54.29	-47.55	-52.44
	64	-49.79	-54.32	-47.59	-52.51

tion performance in terms of NMSE and ACPR for all the DPD models are nearly equal at 64-bit double floating-point DSP.

Table 4.6 shows the DPD results of inter-band non-contiguous case for the predistorted signals generated at 64-bit double floating-point DSP (L=131072, K=9 and M=4). As seen from the Table 4.6, the linearization performance in terms of NMSE and ACPR for all the DPD models are nearly equal for both bands respectively at 64-bit double floating-point DSP.

Table 4.5: Effect of different bit-resolutions on DPD Performances for Intra-Band

Model	**Bit-Res.**	**Contiguous**		**Non-Contiguous**	
		NMSE (dB)	**ACPR (dBc)**	**NMSE (dB)**	**ACPR (dBc)**
W/O DPD	N/A	-6.44	-33.35	-6.13	-31.59
MP DPD	12	-2.49	-10.44	-2.62	-15.85
	16	-8.19	-30.49	-8.14	-29.40
	24	-38.52	-50.38	-36.32	-52.58
	32	-38.57	-50.47	-36.26	-52.46
	64	-38.60	-53.08	-36.19	-51.85
OMP DPD	12	-9.30	-32.96	-9.04	-31.44
	16	-12.33	-34.29	-14.13	-35.52
	24	-38.39	-51.79	-36.12	-51.60
	32	-38.41	-51.24	-36.11	-51.64
	64	-38.64	-54.46	-36.15	-51.85
MP-PCA DPD	12	-31.88	-48.95	-26.10	-47.77
	16	-38.24	-49.98	-36.13	-51.35
	24	-38.26	-50.14	-36.12	-51.18
	32	-38.28	-50.24	-36.14	-51.42
	64	-38.63	-54.28	-36.16	-51.50
MP-ICA DPD	12	-38.42	-52.93	-36.20	-52.30
	16	-38.46	-52.92	-36.14	-52.05
	24	-38.43	-52.28	-36.17	-51.90
	32	-38.38	-52.72	-36.21	-51.98
	64	-38.64	-54.49	-36.24	-52.38

4.4.4 Digital Predistortion Results in lower-bit fixed-point arithmetic

In this section, the different predistorted signals are generated using coefficients extracted earlier in section 4.4.2 for different models at different lower-bit fixed-point resolutions. Table 4.5 also shows the DPD results of intra-band contiguous and intra-band non-contiguous case at 12, 16, 24 and 32 bits fixed-point DSP. As seen from the Table 4.5, the MP-ICA DPD has good NMSE and ACPR performances even at 12-bit fixed-point resolution. It is

Table 4.6: Effect of different bit-resolutions on DPD Performances for Inter-Band Non-Contiguous

Model	Bit-Res.	LB		UB	
		NMSE (dB)	ACPR (dBc)	NMSE (dB)	ACPR (dBc)
W/O DPD	N/A	-17.17	-33.32	-11.76	-31.80
2D-MP DPD	12	-1.06	-14.85	-3.21	-12.34
	16	-19.54	-35.76	-18.84	-36.17
	24	-32.79	-44.32	-29.93	-42.69
	32	-41.48	-51.30	-38.27	-50.62
	64	-41.49	-52.31	-38.30	-50.71
2D-OMP DPD	12	-14.01	-26.94	-16.51	-35.13
	16	-20.39	-36.51	-21.46	-37.54
	24	-31.78	-39.00	-31.32	-38.89
	32	-41.36	-51.19	-38.33	-50.60
	64	-41.48	-52.17	-38.29	-50.57
2D-MP-PCA DPD	12	-32.85	-45.27	-23.85	-43.43
	16	-39.46	-50.06	-37.29	-50.64
	24	-40.04	-50.09	-37.28	-50.57
	32	-40.11	-49.95	-37.29	-50.39
	64	-40.15	-50.12	-37.27	-50.56
2D-MP-ICA DPD	12	-41.18	-51.80	-38.22	-48.89
	16	-41.31	-51.33	-38.25	-50.52
	24	-41.42	-51.31	-38.29	-50.70
	32	-41.45	-51.28	-38.30	-50.59
	64	-41.47	-52.24	-38.32	-50.78

due to fact that the effect of inverse modeling will be visible in linearization performance (NMSE and ACPR) of DPD results. MP-PCA DPD has unsatisfactory performance at 12-bit fixed-point resolution and converges to MP-ICA DPD performance at 16-bit fixed-point resolution.

Both MP and OMP DPD models have unsatisfactory NMSE and ACPR values at 12-

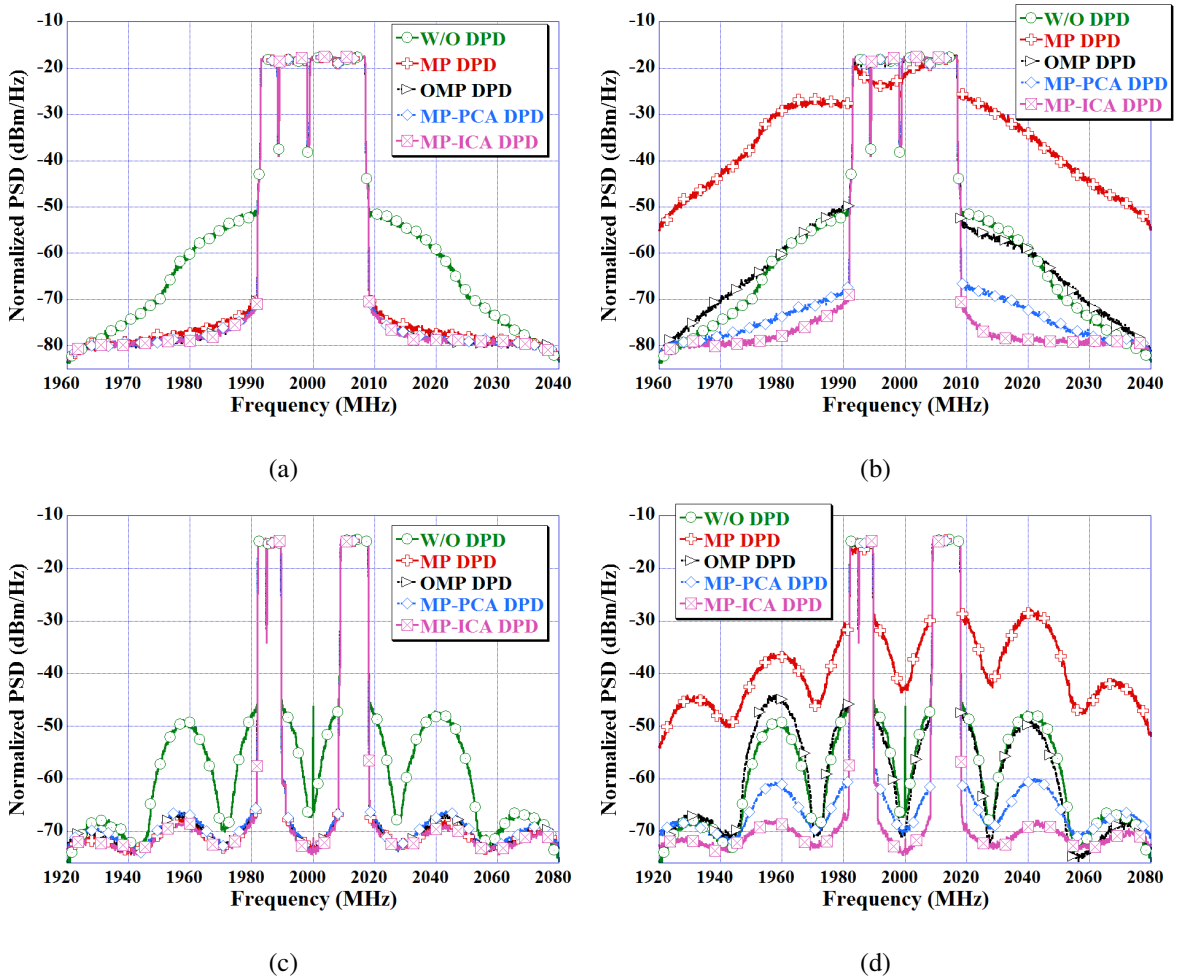

Figure 4.7: Frequency Power Spectra of various DPD model at (a) 64-bit floating-point for intra-band contiguous CA LTE signal, (b) 12-bit fixed-point DSPs for intra-band contiguous CA LTE signal, (c) 64-bit floating-point for intra-band non-contiguous CA LTE signal and (d) 12-bit fixed-point DSPs for intra-band non-contiguous CA LTE signal.

Table 4.7: Comparison of FPGA's Memory Resource for Intra-Band

Model	**Contiguous**			**Non-Contiguous**		
	Matrix Size ($\times 10^6$)	**Bit-Res.**	**Memory Size (MB)**	**Matrix Size** ($\times 10^6$)	**Bit-Res.**	**Memory Size (MB)**
MP	8.29	24	24.88	8.29	24	24.88
OMP	8.29	24	24.88	8.29	24	24.88
MP-PCA	5.90	16	11.80	5.90	16	11.80
MP-ICA	5.90	12	8.85	5.90	12	8.85

Table 4.8: Comparison of FPGA's Memory Resource for Inter-Band Non-Contiguous

Model	LB			UB		
	Matrix Size ($\times 10^6$)	**Bit-Res.**	**Memory Size (MB)**	**Matrix Size ($\times 10^6$)**	**Bit-Res.**	**Memory Size (MB)**
2D-MP	29.49	32	117.96	29.49	32	117.96
2D-OMP	29.49	32	117.96	29.49	32	117.96
2D-MP-PCA	20.45	16	40.89	20.45	16	40.89
2D-MP-ICA	20.45	12	30.67	20.45	12	30.67

bit and 16-bit resolutions and converge to MP-ICA DPD performance at 24-bit fixed-point resolution.

Figure 4.7(a) and Figure 4.7(b) shows the normalized power spectral density (PSD) of intra-band contiguous CA LTE signal at 64-bit floating-point and 12-bit fixed-point DSPs. Similarly, Figure 4.7(c) and Figure 4.7(d) shows the frequency power spectra of intra-band non-contiguous CA LTE signal at 64-bit floating-point and 12-bit fixed-point DSPs. From the graphs, it is clear that ACPR's performance of MP-ICA DPD model is better than other DPD model at 12-bit fixed-point DSP.

Table 4.6 also shows the DPD results of inter-band non-contiguous case at 12, 16, 24 and 32 bits fixed-point DSP. As seen from the Table 4.6, the 2D-MP-ICA DPD has good NMSE and ACPR performances even at 12-bit fixed-point resolution for both the bands. 2D-MP-PCA DPD has unsatisfactory performance at 12-bit fixed point resolution and converges to 2D-MP-ICA DPD performance at 16-bit fixed point resolution.

Both 2D-MP and 2D-OMP models have unsatisfactory NMSE and ACPR values at 12-bit, 16-bit and 24-bit resolutions and converge to 2D-MP-ICA DPD performance at 32-bit fixed-point resolution.

Figure 4.8(a) and Figure 4.8(b) shows the frequency power spectra of LB at 64-bit floating-point and 12-bit fixed-point DSP. Similarly, Figure 4.9(a) and Figure 4.9(b) shows the frequency power spectra of UB at 64-bit floating-point and 12-bit fixed-point DSP. From the graphs, it is clear that ACPR's performance of 2D-MP-ICA DPD model is better than other DPD model at 12-bit fixed-point DSP.

The bit-resolution of each sample and size of observation (predistorter) matrix determines

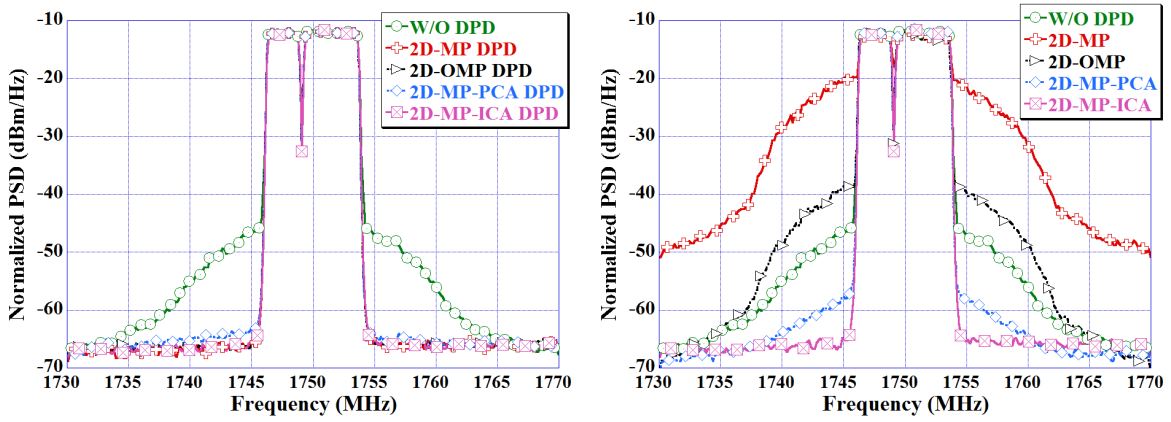

(a) (b)

Figure 4.8: Frequency Power Spectra of various DPD model at (a) 64-bit floating-point for LB of inter-band non-contiguous CA LTE signal, and (b) 12-bit fixed-point DSPs for LB of inter-band non-contiguous CA LTE signal.

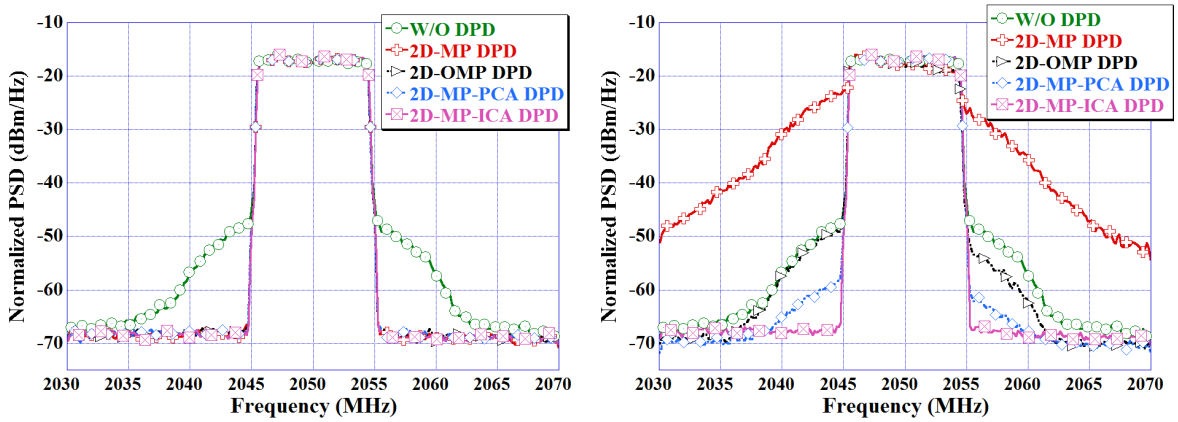

(a) (b)

Figure 4.9: Frequency Power Spectra of various DPD model at (a) 64-bit floating-point for UB of inter-band non-contiguous CA LTE signal, and (b) 12-bit fixed-point DSPs for UB of inter-band non-contiguous CA LTE signal.

the FPGA's memory size required by a DPD model [45, 71].

As ICA technique shows good linearization performance at 12-bit resolution. Table 4.7 and Table 4.8 show ICA based DPD model requires least memory size (Mega Byte or MB) for intra-band and inter-band CA respectively.

4.4.5 Digital Predistortion and Efficiency

Figure. 4.10 shows the measured ACPR, average output power and corresponding power added eficiency (PAE) of without DPD signal and MP-ICA DPD signal for all CA cases

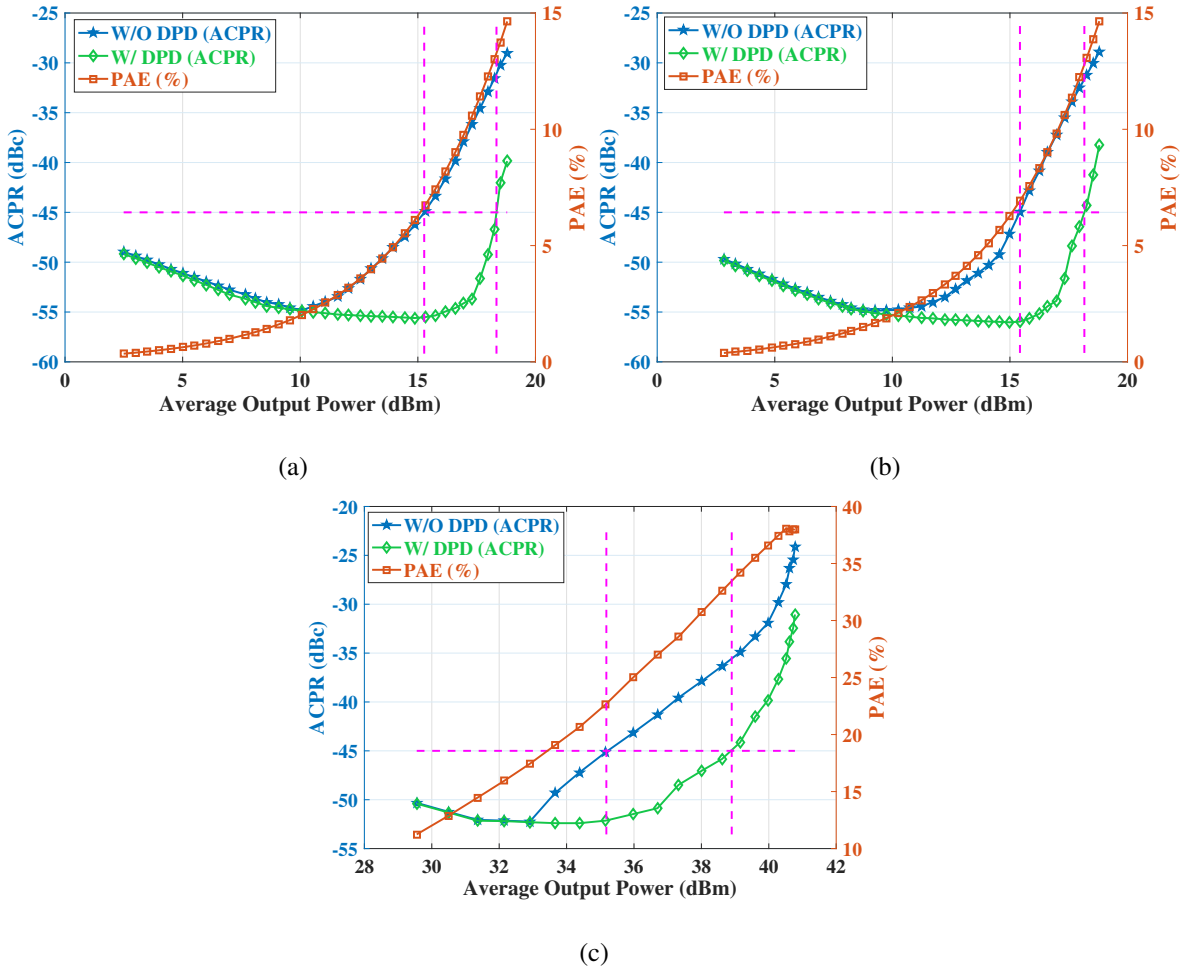

Figure 4.10: Measured ACPR, average output power and PAE for (a) Intra-band contiguous CA LTE signal, (b) Intra-band non-contiguous CA LTE signal and (c) Inter-band non-contiguous CA LTE signal.

to demonstrate the proposed DPD's performance. The same measurement DUT (PA) is used for Intra-band contiguous CA and Intra-band non-contiguous CA case as mentioned in section 4.3.1. Whereas the DUT (PA) mentioned in section 4.3.2 is used for inter-band non-contiguous CA.

The acceptable ACPR performance of -45 dBc is used as a threshold. From Figure. 4.10(a), when ACPR≃-45 dBc, the average output power of without DPD signal is 15.27 dBm and MP-ICA DPD signal is 18.34 dBm for intra-band contiguous CA case. The PAE is increased from 6.67% to 13.27% for ACPR≃-45 dBc.

From Figure. 4.10(b), when ACPR≃-45 dBc, the average output power of without DPD signal is 15.43 dBm and MP-ICA DPD signal is 18.17 dBm for intra-band non-contiguous CA case. The PAE is increased from 6.92% to 12.79%.

From Figure. 4.10(c), when ACPR≃-45 dBc, the average output power of without DPD

signal is 35.18 dBm and 2D-MP-ICA DPD signal is 39.8 dBm for inter-band non-contiguous CA case. The PAE is increased from 22.70% to 33.47%.

With the proposed ICA algorithm, these performance are achieved even for 12 bit fixed-point DSPs, where state-of-the-art DPD models provide it for 64-bit DSPs.

4.5 Conclusion

This chapter presents ICA based non-linear polynomial DPD model for linearization of multi-band PA using CA signals. The proposed ICA based DPD model is implemented in 12-bit fixed point DSP and shows good linearization results. Due to that, the ICA based DPD model has least memory resource utilization with reduced coefficient extraction burden. This is beneficial for 5G wireless communication where the resources might be shared between many hardware devices.

In this chapter, the ICA based DPD model is presented for concurrent dual-band operation at uncorrelated carrier frequencies. The next chapter deals with the concurrent multi-band DPD models operating at harmonic frequencies. In the next chapter, novel DPD models are presented to compensate the additional IMDs and CMDs generated when carrier frequencies are at harmonic frequencies.

Chapter 5

Digital Predistortion for concurrent multi-band transmission at harmonic frequencies

5.1 Introduction

Recently research in PA design focuses towards ultra-wideband application [80–82] and while supporting various generation signals, harmonics of one carrier signal may interfere with the frequency range of another carrier signal. This is shown in Figure 5.1(b), when the second carrier signal is transmitted at the harmonic frequency of the first carrier signal and cannot be filtered out. Different scenarios of frequencies allocations by 3GPP standard will be used to better illustrate the problem and the need to mitigate the problem of inter-band distortion as well as its impact on the quality of the downlink (DL) signal and /or uplink (UL) signal at the input of or output of the RF front-end. For example, in inter-band carrier aggregation (CA), the harmonics generated from E-UTRA Band 29 DL (717–728 MHz) may interfere with band 4 DL (2110–2155 MHz) over the North American region [93]. Similarly, the harmonics generated from E-UTRA Band 28 UL (703–748 MHz) may interfere with band 21 UL (1447.9–1462.9) and band 11 UL (1427.9–1447.9 MHz) over the Asian region [94]. Similarly, the harmonics generated from E-UTRA Band 8 DL (925–960 MHz) may interfere with band 3 DL (1805–1880 MHz) over the European region. In the forthcoming 5G communication system, the frequency bands operation would extend from 3.5 GHz to 6 GHz in sub-6 GHz radio frequency or possibly to 30–100 GHz in millimeter-

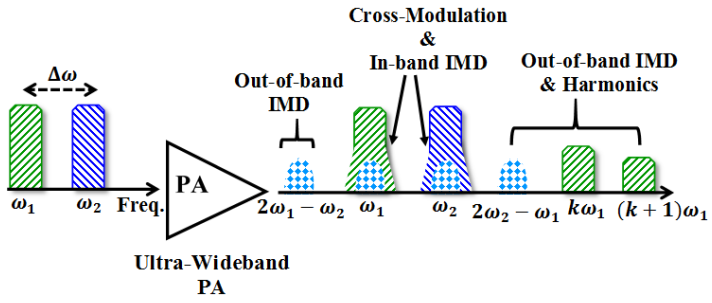

(a)

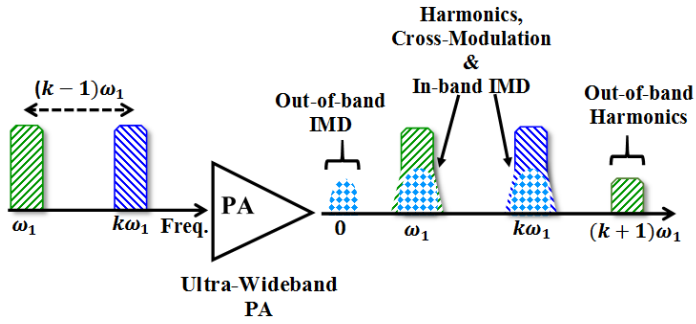

(b)

Figure 5.1: Scenarios in Concurrent dual-band transmitters (a) When two carrier frequencies are separated by 100-500 MHz and (b) When second carrier signal is transmitted at a harmonic frequency of the first carrier signal.

wave frequency band. This might result in further increase in harmonic interference. In this scenario, these models [43, 47–49, 95] are insufficient to capture the harmonic interference. In [96], the third-order harmonics of the envelope-tracking PA is canceled using non-linear kernels. In [42], the 2D-HMP model is proposed for behavioral modeling and DPD of the interference from harmonics in concurrent dual-band transmitters. The 2D-HMP model was able to linearize the ultra-wideband PA and remove the non-linear distortions such as in-band IMDs, harmonic interferences and CMDS in concurrent dual-band transmitters. Since there are four summations in each band of 2D-HMP model, a large number of coefficients are required. This led to increase in the computational complexity, the coefficient extraction burden and the cost of FPGA's memory resource in real-time applications.

This chapter presents the less complex 2D-CHMP model for efficient DPD implementation [97]. The 2D-CHMP model is constructed by simplifying the envelope terms of 2D-HMP models. In the proposed 2D-CHMP model, there are three summations in each band, thus the number of coefficients required and size of observation (predistorter) matrix are decreased. It also processes each band and therefore sampling rate requirements for ADCs and

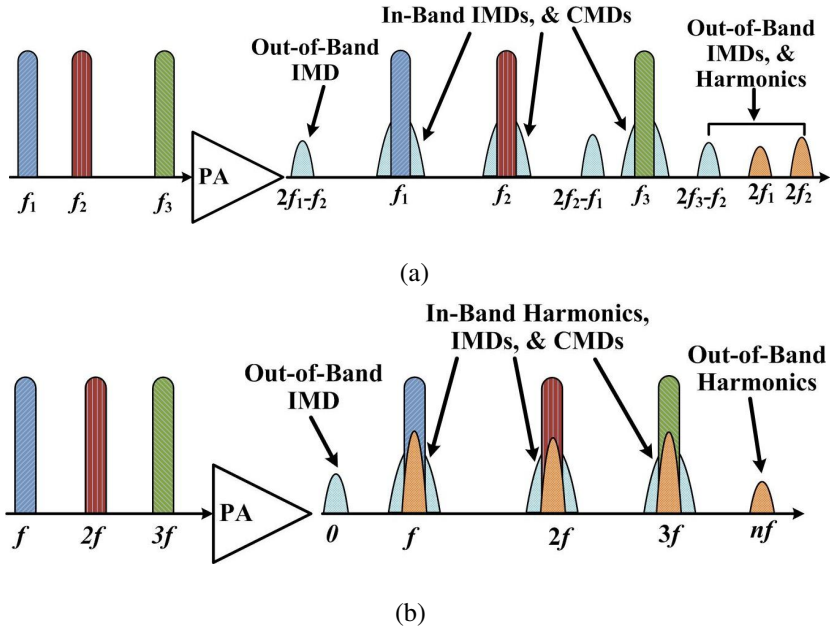

Figure 5.2: (a) Generally studied scenario, when three carrier frequencies are uncorrelated i.e. not at harmonic frequencies and (b) Scenario when three carrier frequencies are at harmonic frequencies.

DACs are reduced. As it also considers in-band IMDs, harmonic interferences and CMDs, thus it has similar linearization performance as the 2D-HMP model. The application of PCA upon 2D-CHMP, results in further reduction in matrix size with lower-bit (16-bit) fixed-point FPGA implementation. Thus proposed method reduces computational complexity, the coefficient extraction burden and the FPGA's memory resource.

In this chapter, the analysis of harmonic distortions is further extended to concurrent tri-band transmitter. In concurrent tri-band transmitter, three-dimensional memory polynomial (3D-MP) was proposed to linearize for the scenario as shown in Figure 5.2(a) [98]. This model was modified to 3D Phase aligned Pruned Volterra Model (3D-PAV) in [99] for better linearization of PA. There are few more DPD models proposed to linearize concurrent tri-band transmitter [100–102]. However, in these papers [98–102], carrier signals are not transmitted at the harmonic frequencies in the concurrent tri-band transmitter as shown in Figure 5.2(a). In that scenario, out-of-band IMDs and harmonic terms can be filtered out. If carrier signals are transmitted at harmonic frequencies as shown in Figure 5.2(b), in addition to in-band CMDs and IMDs, inband harmonic distortions would also be present at the output of tri-band PA. This chapter further presents novel 3D-HMP and 3D-HVS DPD models for behavioral modeling and linearization of a concurrent tri-band transmitter operating at har-

monic frequencies [103]. The proposed models include the IMD terms which are generating the harmonic distortions in the concurrent tri-band transmitter. These proposed models aim to linearize PA in presence of in-band IMDs, CMDs and harmonic distortions.

This chapter is organized as follows: Section 5.2.1 describes the 2D-HMP model. Section 5.2.2 proposes the 2D-CHMP model. Section 5.2.3 describes the steps involved in the determination and performance of the 2D-CHMP model. Section 5.2.4 compares complexity between 2D-CHMP and 2D-HMP models. Section 5.2.5 describes the measurement testbeds used for dual-band/ultra-wideband PA characterization, data extraction and DPD respectively. Section 5.2.6 reports the results of inverse modeling performances of the dual-band DPD models and effect of lower-bit fixed-point arithmetic. Section 5.2.7 reports the measured results of DPD. Section 5.3.1 describes the state-of-the-art Tri-Band DPD Models. Section 5.3.2 provides analysis of the harmonic distortions in concurrent tri-band transmitter. Section 5.3.3 defines the 3D-HMP and 3D-HVS DPD models. Section 5.3.4 describes the measurement testbed used for tri-band PA characterization and DPD respectively. Section 5.3.5 reports the results of behavioral modeling and DPD performances of different models. Section 5.4 gives the conclusion of the chapter.

5.2 Concurrent Dual-Band DPD Models at Harmonics Frequencies

5.2.1 Proposed 2D Curtailed Harmonic Memory Polynomial Model

Let us consider a single-band conventional MP model [24]

$$y(n) = \sum_{m=0}^{M} \sum_{k=0}^{K-1} c_{m,k} \cdot x(n-m) \cdot |x(n-m)|^k \tag{5.1}$$

where M, K and $c_{m,k}$ are the memory depth, nonlinearity order and coefficients of the model respectively.

To analyze the PA output, let us simplify only odd-order memoryless non-linearities up to the seventh term:

$$y(n) = c_{0,0}x + c_{0,2}x|x|^2 + c_{0,4}x|x|^4 + c_{0,6}x|x|^6 \tag{5.2}$$

Considering the case of harmonics interference, the modulated input signal is given as

$$x = x_1 e^{j\omega_1 nT} + x_2 e^{j\omega_2 nT} = x_1 e^{\alpha j\omega nT} + x_2 e^{\beta j\omega nT} \tag{5.3}$$

where x_1 and x_2 are the two modulated complex baseband input signals being transmitted at carrier frequencies ω_1=$\alpha\omega$ and ω_2=$\beta\omega$ respectively, where $\alpha, \beta \in \mathbb{Z}_+$ and $\alpha \neq \beta$.

By substituting equation (5.3) in equation (5.2), we get

$$\begin{aligned}
y(n) &= (c_{0,0}x_1 + c_{0,2}x_1|x_1|^2 + 2c_{0,2}x_1|x_2|^2 + c_{0,4}x_1|x_1|^4 \\
&+6c_{0,4}x_1|x_1|^2|x_2|^2 + 3c_{0,4}x_1|x_2|^4 + c_{0,6}x_1|x_1|^6 \\
&+12c_{0,6}x_1|x_1|^4|x_2|^2 + 18c_{0,6}x_1|x_1|^2|x_2|^4 + 4c_{0,6}x_1|x_2|^6)e^{\alpha j\omega nT} \\
&+(c_{0,0}x_2 + c_{0,2}x_2|x_2|^2 + 2c_{0,2}x_2|x_1|^2 + c_{0,4}x_2|x_2|^4 \\
&+6c_{0,4}x_2|x_2|^2|x_1|^2 + 3c_{0,4}x_2|x_1|^4 + c_{0,6}x_2|x_2|^6 \\
&+12c_{0,6}x_2|x_2|^4|x_1|^2 + 18c_{0,6}x_2|x_2|^2|x_1|^4 + 4c_{0,6}x_2|x_1|^6)e^{\beta j\omega nT} \\
&+(c_{0,2}x_1^2x_2^* + 2c_{0,4}x_1^2x_2^*|x_1|^2 + 3c_{0,4}x_1^2x_2^*|x_2|^2 \\
&+3c_{0,6}x_1^2x_2^*|x_1|^2|x_2|^2 + 3c_{0,6}x_1^2x_2^*|x_2|^4)e^{(2\alpha-\beta)j\omega nT} \\
&+(c_{0,2}x_2^2x_1^* + 2c_{0,4}x_2^2x_1^*|x_2|^2 + 3c_{0,4}x_2^2x_1^*|x_1|^2 \\
&+3c_{0,6}x_2^2x_1^*|x_2|^2|x_1|^2 + 3c_{0,6}x_2^2x_1^*|x_1|^4)e^{(2\beta-\alpha)j\omega nT} \\
&+(c_{0,4}x_1^3x_2^{*2} + 3c_{0,6}x_1^3x_2^{*2}|x_1|^2 + 4c_{0,6}x_1^3x_2^{*2}|x_2|^2)e^{(3\alpha-2\beta)j\omega nT} \\
&+(c_{0,4}x_2^3x_1^{*2} + 3c_{0,6}x_2^3x_1^{*2}|x_2|^2 + 4c_{0,6}x_2^3x_1^{*2}|x_1|^2)e^{(3\beta-2\alpha)j\omega nT} \\
&+(c_{0,6}x_1^4x_2^{*3})e^{(4\alpha-3\beta)jwnT} + (c_{0,6}x_2^4x_1^{*3})e^{(4\beta-3\alpha)j\omega nT}
\end{aligned} \tag{5.4}$$

These terms $2\alpha-\beta$, $2\beta-\alpha$, $3\alpha-2\beta$, $3\beta-2\alpha$, $4\alpha-3\beta$ and $4\beta-3\alpha$ are neither equal to α and nor equal to β when $\alpha \neq \beta$. Therefore the out-of-band IMD terms at $(2\alpha-\beta)\,\omega$, $(2\beta-\alpha)\,\omega$, $(3\alpha-2\beta)\,\omega$, $(3\beta-2\alpha)\,\omega$, $(4\alpha-3\beta)\,\omega$ and $(4\beta-3\alpha)\,\omega$ can be filtered out and thus the output signals at $\alpha\omega$ and $\beta\omega$ are given as

$$\begin{aligned}
y_1(n) &= c_{0,0}x_1 + c_{0,2}x_1(|x_1|^2 + 2|x_2|^2) + c_{0,4}x_1(|x_1|^4 + 6|x_1|^2|x_2|^2 \\
&+3|x_2|^4) + c_{0,6}x_1(|x_1|^6 + 12|x_1|^4|x_2|^2 + 18|x_1|^2|x_2|^4 + 4|x_2|^6)
\end{aligned} \tag{5.5}$$

and

$$\begin{aligned}
y_2(n) &= c_{0,0}x_2 + c_{0,2}x_2(|x_2|^2 + 2|x_1|^2) + c_{0,4}x_2(|x_2|^4 + 6|x_2|^2|x_1|^2 \\
&+3|x_1|^4) + c_{0,6}x_2(|x_2|^6 + 12|x_2|^4|x_1|^2 + 18|x_2|^2|x_1|^4 + 4|x_1|^6)
\end{aligned} \tag{5.6}$$

Equations (5.5) and (5.6) considers only odd-order memoryless non-linearities. To further include even-order memoryless non-linearities to the output of model, even-order memoryless non-linearities also need to be simplified. Even-order memoryless non-linearities can be written in terms of odd-order memoryless non-linearities and further simplified as equation (5.2). These are even-order memoryless non-linearities:

$$\begin{aligned}
&c_{0,1}x|x| + c_{0,3}x|x|^3 + c_{0,5}x|x|^5 + c_{0,7}x|x|^7 \\
&= \left(c_{0,1}x + c_{0,3}x|x|^2 + c_{0,5}x|x|^4 + c_{0,6}x|x|^6\right) \cdot |x|
\end{aligned} \tag{5.7}$$

The terms inside the first parenthesis of equation (5.7) can be simplified similarly as equation (5.2). The term $|x|$ can be replaced by a generalized term $\left||x_r| + jd_g^r\,|x_s|\right|$ where d_g^r ($r \in \{1,2\}$) is the real-valued generalized coefficients for lower band (LB) and upper band (UB) respectively.

By combining even-order terms with odd-order terms from equations (5.5) and (5.6) and also considering memory terms, results in generalized 2D-Curtailed HMP (2D-CHMP) [97] model whose output signals are

$$\begin{aligned} y_1(n) &= \sum_{m=0}^{M}\sum_{k=0}^{K-1} c_{m,0,k}^{1,1}\cdot x_1(n-m)\cdot G_k^1(n-m) \\ &+ \sum_{m=0}^{M_l}\sum_{q=1}^{Q_l}\sum_{k=0}^{K-1} c_{m,q,k}^{1,2}\cdot x_2^q(n-m)\cdot x_1^{*(2q-1)}(n-m)\cdot G_k^1(n-m) \\ &+ \sum_{m=0}^{M_u}\sum_{q=1}^{Q_u}\sum_{k=0}^{K-1} c_{m,q,k}^{1,3}\cdot x_1^{2q+1}(n-m)\cdot x_2^{*q}(n-m)\cdot G_k^1(n-m) \end{aligned} \tag{5.8}$$

and

$$\begin{aligned} y_2(n) &= \sum_{m=0}^{M}\sum_{k=0}^{K-1} c_{m,0,k}^{2,1}\cdot x_2(n-m)\cdot G_k^2(n-m) \\ &+ \sum_{m=0}^{M_l}\sum_{q=1}^{Q_l}\sum_{k=0}^{K-1} c_{m,q,k}^{2,2}\cdot x_2^{q+1}(n-m)\cdot x_1^{*2q}(n-m)\cdot G_k^2(n-m) \\ &+ \sum_{m=0}^{M_u}\sum_{q=1}^{Q_u}\sum_{k=0}^{K-1} c_{m,q,k}^{2,3}\cdot x_1^{2q}(n-m)\cdot x_2^{*(q-1)}(n-m)\cdot G_k^2(n-m) \end{aligned} \tag{5.9}$$

where $G_k^r(n) = G_k^r(|x_r(n)|\,,|x_s(n)|)$, $r,s \in \{1,2\}$ and $r \neq s$ and $G_k^r(|x_r(n)|\,,|x_s(n)|)$ can be expressed as:

$$G_k^r(|x_r|\,,|x_s|) = \begin{cases} 1 & ,k=0 \\ \left||x_r| + jd_g^r\,|x_s|\right| & ,k=1 \\ |x_r|^2 + 2|x_s|^2 & ,k=2 \\ \left(|x_r|^2 + 2|x_s|^2\right)\cdot\left(\left||x_r| + jd_g^r\,|x_s|\right|\right) & ,k=3 \\ |x_r|^4 + 6|x_r|^2|x_s|^2 + 3|x_s|^4 & ,k=4 \\ \left(|x_r|^4 + 6|x_r|^2|x_s|^2 + 3|x_s|^4\right)\cdot\left(\left||x_r| + jd_g^r\,|x_s|\right|\right) & ,k=5 \\ |x_r|^6 + 12|x_r|^4|x_s|^2 + 18|x_r|^2|x_s|^4 + 4|x_s|^6 & ,k=6 \\ \left(|x_r|^6 + 12|x_r|^4|x_s|^2 + 18|x_r|^2|x_s|^4 + 4|x_s|^6\right)\cdot \\ \qquad\qquad \times\left(\left||x_r| + jd_g^r\,|x_s|\right|\right) & ,k=7 \end{cases} \tag{5.10}$$

Using inductive reasoning, $G_k^r(|x_r(n)|\,,|x_s(n)|)$ can be mathematically expressed as:

$$G_k^r(|x_r|\,,|x_s|) = \begin{cases} \sum_{i=0}^{k/2}\binom{k/2+1}{i}\binom{k/2}{i}|x_r|^{k-2i}|x_s|^{2i} & ,k \text{ is even} \\ \left(\sum_{i=0}^{(k-1)/2}\binom{(k-1)/2+1}{i}\binom{(k-1)/2}{i}|x_r|^{k-1-2i}|x_s|^{2i}\right)\cdot & \\ \qquad\qquad \times\left(\left||x_r| + jd_g^r\,|x_s|\right|\right) & ,k \text{ is odd} \end{cases} \tag{5.11}$$

where $\binom{k}{i} = \frac{k!}{i!(k-i)!}$.

5.2.2 Determination of 2D-CHMP Model parameters

Indirect learning approach is a well-established method for the DPD [24]. In the Indirect learning architecture (ILA), DPD requires inverse modeling of PA. The determination of the 2D-CHMP model follows two steps: First, set the value of d_g^r from the range 0 to 2 and then using LS method to extract the model coefficients $c_{m,q,k}^{r,p}$.

After determination, the performance of inverse modeling of the proposed model is evaluated in terms of metrics like ACEPR and NMSE. NMSE and ACEPR are considered as a measure of in-band and out-of-band modeling performance respectively [79].

In determination, employing the general sweep of d_g^r for a constant step size of Δd_g^r=0.25 over the range 0 to 2 and then using minimum NMSE as criteria to choose the d_g^r, increases the computational complexity. Instead, binary search algorithm [104] can be used to find the value of d_g^r for each band which gives the minimum value of NMSE (dB). The steps followed in the binary search algorithm are as follows:

1. Start
2. Set $d_{left}^r = 0$, $d_{right}^r = 2$,
   $\Delta d_g^r = (d_{right}^r - d_{left}^r)/2 = 1$,
   $d_{middle}^r = (d_{right}^r + d_{left}^r)/2 = 1$
3. Set $d_g^r = d_{middle}^r$, extract the model coefficients $c_{m,q,k}^{r,p}$ and calculate NMSE_{middle}^r
4. Set $\Delta d_g^r = \Delta d_g^r/2$,
   $d_{left}^r = d_{middle}^r - \Delta d_g^r$,
   $d_{right}^r = d_{middle}^r + \Delta d_g^r$
5. Set $d_g^r = d_{left}^r$, extract the model coefficients $c_{m,q,k}^{r,p}$ and calculate NMSE_{left}^r
6. Set $d_g^r = d_{right}^r$, extract the model coefficients $c_{m,q,k}^{r,p}$ and calculate NMSE_{right}^r
7. Compare NMSE_{left}^r, NMSE_{middle}^r & NMSE_{right}^r, assign minimum NMSE as NMSE_{min}^r and assign corresponding value of d_g^r as d_{g-min}^r
8. Set $\text{NMSE}_{middle}^r = \text{NMSE}_{min}^r$,
   $d_{middle}^r = d_{g-min}^r$

Table 5.1: Comparison of the number of coefficients in a band

Model	Number of Coefficients in a Band
2D-HMP	$[(M+1)+(M_l+1)\,Q_l+(M_u+1)\,Q_u]\cdot K\,(K+1)\,/2$
2D-CHMP	$[(M+1)+(M_l+1)\,Q_l+(M_u+1)\,Q_u]\cdot K$

9. If $\Delta d_g^r \leq 0.25$ then:
   $\text{NMSE}_{min}^r = \text{NMSE}_{middle}^r$,
   $d_g^r = d_{middle}^r$
   Else: Go to Step 4

10. Stop

We have set the condition $\Delta d_g^r \leq \Delta d_{g-min}^r$ (Δd_{g-min}^r=0.25) to exit from this algorithm, i.e. step size should not be less than 0.25. It is shown later in Section 5.2.5, that further decreasing the minimum step size Δd_{g-min}^r from 0.25 does not improve the minimum value of NMSE.

5.2.3 Computational Complexity comparison between 2D-HMP and 2D-CHMP Models

Table 5.1 shows the comparison of the number of coefficients in a band (LB or UB), where the proposed 2D-CHMP model has complexity $O(n^3)$ as compared to $O(n^4)$ of the 2D-HMP model in terms of coefficients. The number of coefficients in the 2D-CHMP model is $(K+1)\,/2$ times less than the number of coefficients in the 2D-HMP model.

In the Indirect learning architecture of DPD, generally at least 2 or 3 LS iterations are needed to converge to the best DPD performance. To implement LS extraction, the pseudo-inverse method is used for matrix inversion. Taking an example of 2 LS iterations, 4 matrix pseudo inversions are required for the 2D-HMP model (2 for LB and 2 for UB) and the matrix size is $L \times \{[(M+1)+(M_l+1)\,Q_l+(M_u+1)\,Q_u]\cdot K\,(K+1)\,/2\}$, where L is the number of input samples. According to the binary search algorithm in the 2D-CHMP model, there are 5 matrix pseudo inversions in a band until the condition $\Delta d_g^r \leq 0.25$ is satisfied. Once d_g^r is calculated in the first iteration, then there is no need for binary search algorithm in the second iteration. Thus, it only needs one more matrix pseudo in-

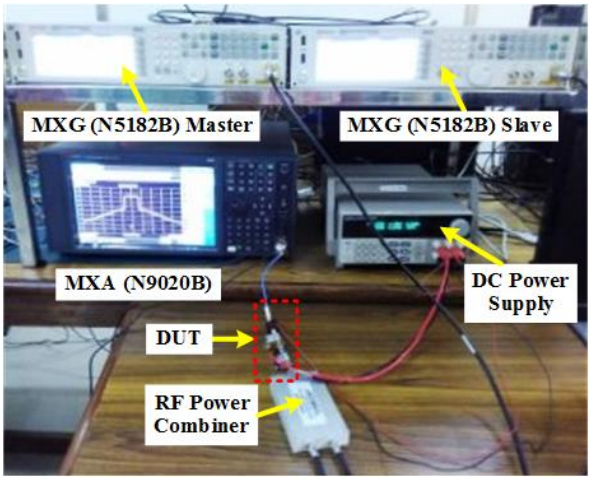

Figure 5.3: Measurement Setup Testbed II.

version for each band in a second LS iteration. In total, the 2D-CHMP model requires 12 matrix inversions (5+1 for LB and 5+1 for UB), but the matrix size is much lower $L \times \{[(M+1)+(M_l+1)\,Q_l+(M_u+1)\,Q_u]\cdot K\}$. The total computational complexity in the model's determination can be assessed as a product of the matrix size and number of the matrix pseudo inversion [95]. Generally at least nonlinearity order $K \geq 5$ is required, we have

$$\begin{aligned} &12L \times \{[(M+1)+(M_l+1)\,Q_l+(M_u+1)\,Q_u]\cdot K\} \leq \\ &4L \times \{[(M+1)+(M_l+1)\,Q_l+(M_u+1)\,Q_u]\cdot K\,(K+1)\,/2\} \end{aligned} \tag{5.12}$$

Thus the total computational complexity when determining the proposed 2D-CHMP model is lesser or equal to the 2D-HMP model. The total complexity of the proposed 2D-CHMP model is reduced by a factor of $(4/12)\times(K+1)\,/2$=$(K+1)\,/6$.

If 3 LS iterations are required in DPD, the 6 matrix pseudo inversions are required for the 2D-HMP model (3 for LB and 3 for UB). The 2D-CHMP model requires 14 matrix inversions (5+1+1 for LB and 5+1+1 for UB). Thus the total complexity of the proposed 2D-CHMP model is reduced by a factor of $(6/14)\times(K+1)\,/2 = 3\,(K+1)\,/14$.

5.2.4 Measurement Testbed for Concurrent Dual-Band DPD

We have used two measurement testbed. First measurement testbed is a FPGA-based transceiver and second measurement testbed consists of VSGs and VSA, which are conventionally used in earlier published literature [43].

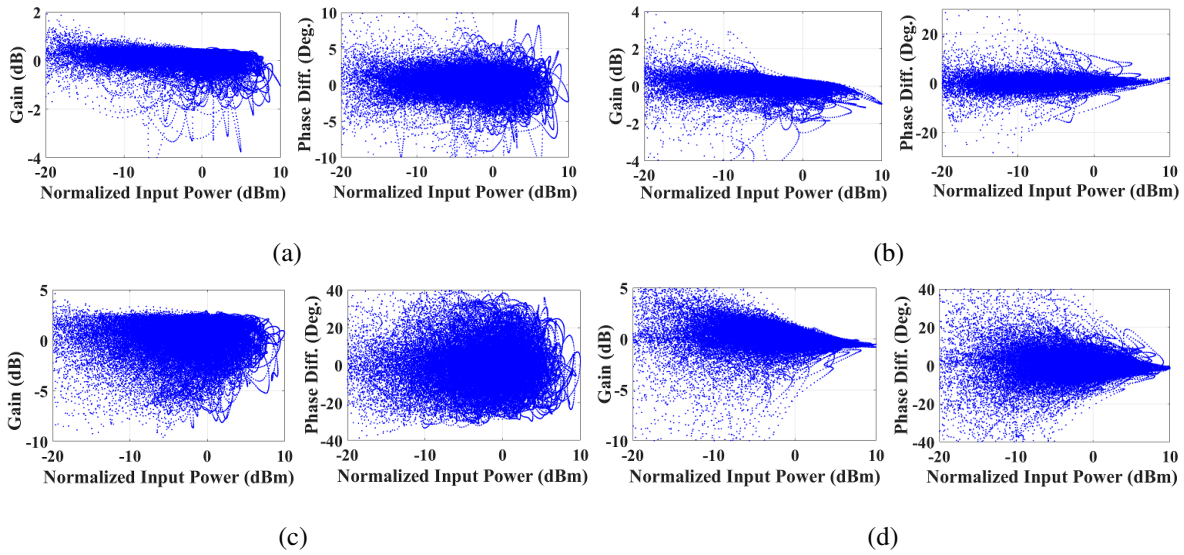

Figure 5.4: AM/AM and AM/PM characteristics of (a) ZX60-14012L+ PA at LB, (b) ZX60-14012L+ PA at UB, (c) CLF1G0060-10 PA at LB and (d) CLF1G0060-10 PA at UB

5.2.4.1 Measurement Testbed I

The transceiver of first measurement testbed is same as shown in Figure 4.3 in previous chapter. The measurement testbed consists of an Altera Arria V GT FPGA, dual channel transmitter (TSW30SH84), transmitter observation receiver (TSW1266), ZX60-14012L+ ultra-wideband PA from Mini-Circuits, CLF1G0060-10 ultra-wideband PA from NXP, local oscillator (TSW3065), RF switch matrix, ZN2PD2-50-S+ power combiner/splitter from Mini-Circuits and attenuators. The FPGA transmits the data to the transmitter at a sampling frequency of 307.2 Msps. The DAC further interpolates the data by a factor of 4 to a sampling rate of 1228.8 Msps. The signal is up-converted to RF by TRF3705 using local oscillators (LO) (TSW3065) and sent to a PA.

Two different ultra-wideband PAs are used in the first measurement setup: 1) ZX60-14012L+ is an ultra-wideband PA whose frequency range from 300 kHz to 14 GHz and 11.5 dBm output power at 1 dB gain compression; 2) CLF1G0060-10 is a 10 W GaN HEMT based ultra-wideband PA whose frequency range is from DC to 6 GHz and 36 dBm output power at 1 dB gain compression.

10 MHz LTE signal with a PAPR of 11.95 dB at 1956.8 MHz (LO_2=1880 MHz + IF_2 shift=76.8 MHz) and 5 MHz WCDMA signal with a PAPR of 10.05 dB at 978.4 MHz (LO_1=940 MHz + IF_1 shift=38.4 MHz) are used to drive the PA. Figure 5.4 shows Amplitude Modulation/Amplitude Modulation (AM/AM) and Amplitude Modulation/Phase Modula-

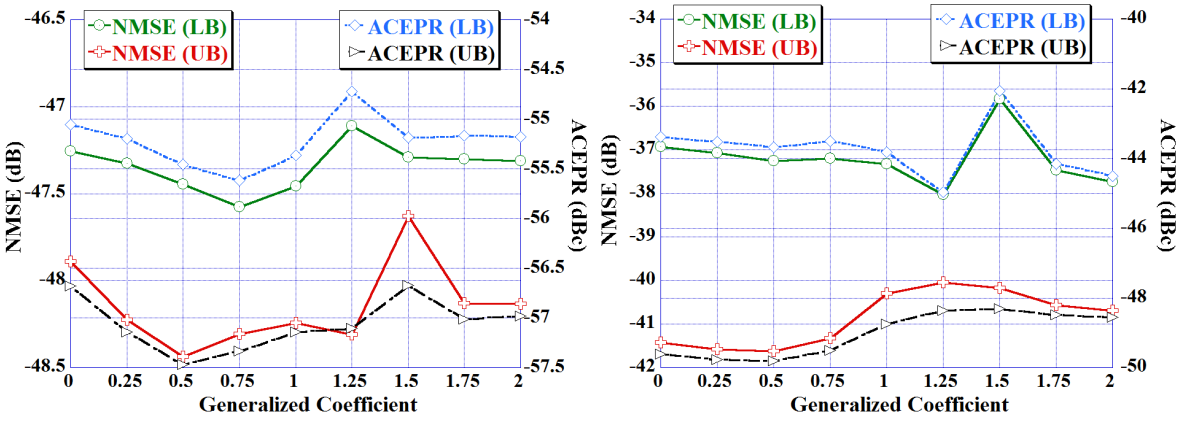

(a) (b)

Figure 5.5: Inverse Modeling performance for different values of generalized coefficient d_g^r at LB and UB for (a) ZX60-14012L+ PA and (b) CLF1G0060-10 PA.

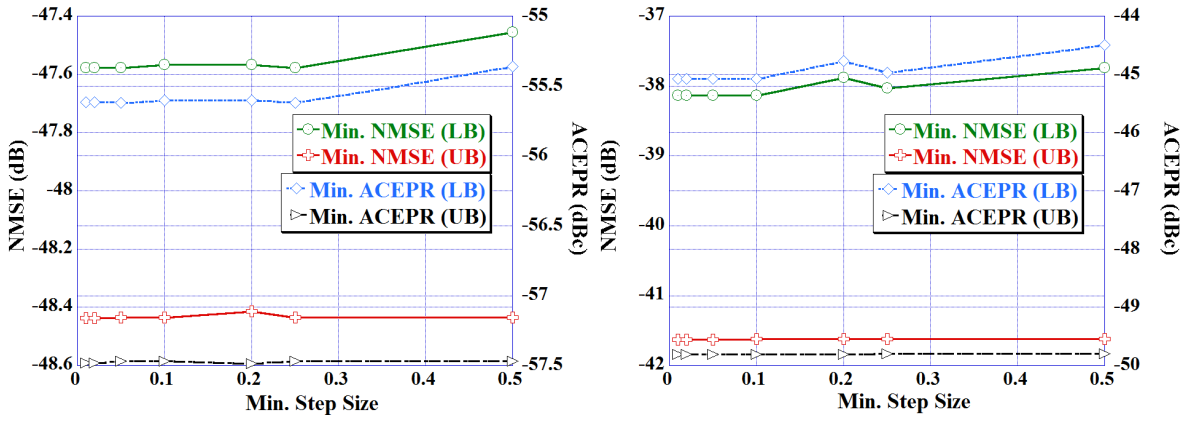

(a) (b)

Figure 5.6: NMSE_{min}^r and ACEPR_{min}^r values obtained using binary search algorithm for different values of min. step size Δd_{g-min}^r at LB and UB for (a) ZX60-14012L+ PA and (b) CLF1G0060-10 PA.

tion (AM/PM) characteristics of ZX60-14012L+ PA and CLF1G0060-10 PA at LB and UB respectively. As from graphs, it can be seen that there is severe distortion in the output signal at both the bands. Actually, these distortions result from the IMD and harmonic interference which falls at frequencies $\alpha\omega$ and $\beta\omega$. The non-linear IMD terms like $x_2^{\alpha q}(n) \cdot x_1^{*(\beta q-1)}(n)$ and $x_1^{\beta q+1}(n) \cdot x_2^{*\alpha q}(n)$ lie at $\alpha\omega$ and interfere with $x_1(n)$. Similarly, the non-linear IMD terms like $x_2^{\alpha q+1}(n) \cdot x_1^{*\beta q}(n)$ and $x_1^{\beta q}(n) \cdot x_2^{*(\alpha q-1)}(n)$ lie at $\beta\omega$ and interfere with $x_2(n)$.

At the receiver (TSW1266), proper selection of one frequency band (harmonic or fundamental frequency band) and its corresponding LO is required. For that purpose, switch matrix is used. The received signal is then down-converted by ADC at a sampling frequency

Table 5.2: Inverse Modeling Performances for different PAs

PA	Model	LB			UB		
		NMSE (dB)	ACEPR (dBc)	No. of Coeff.	NMSE (dB)	ACEPR (dBc)	No. of Coeff.
I	**2D-HMP**	-48.11	-56.09	540	-49.24	-57.89	540
	2D-HMP-PCA	-47.73	-55.83	215	-48.78	-57.62	222
	2D-CHMP	-47.58	-55.62	120	-48.44	-57.47	120
	2D-CHMP-PCA	-47.47	-55.50	80	-48.35	-57.33	84
II	**2D-HMP**	-39.12	-46.22	540	-43.33	-51.35	540
	2D-HMP-PCA	-38.67	-45.81	247	-42.98	-51.08	249
	2D-CHMP	-38.03	-44.97	120	-41.62	-49.80	120
	2D-CHMP-PCA	-37.87	-44.69	85	-41.56	-49.66	86

of 614.4 Msps. A 10 MHz reference clock is provided by LO (TSW3065) to synchronize the transmitter and receiver. The received signal is then stored in FPGA's memory which can be further processed using Matlab.

5.2.4.2 Measurement Testbed II

Figure 5.3 shows the second measurement testbed. It consists of two VSGs (Keysight MXG "N5182B"), VSA (Keysight MXA "N9020B"), two ZX60-V63+ PAs, RF power combiner/splitter from Mini-Circuits and attenuators. These two VSGs are time synchronized with each other and also synchronized with VSA. 10 MHz LTE-OFDM signal with a PAPR of 10.7 dB and 20 MHz LTE-OFDM signal with a PAPR of 10.82 dB are transmitted at 1.2 GHz and 2.4 GHz respectively. These two RF signals are combined together using ZN2PD2-50-S+ power combiner and passed through two ZX60-V63+ PAs in cascade. ZX60-V63+ PA has an operating frequency range from 0.05 to 6 GHz and 17.8 dBm output power at 1 dB gain compression. The output of PA is attenuated and then captured at VSA.

5.2.5 Inverse Modeling Performance

Figure 5.5(a) and Figure 5.5(b) shows the inverse modeling performance of the 2D-CHMP model in terms of NMSE and ACEPR for different values of generalized coefficient d_g^r at

LB (978.4 MHz) and UB (1956.8 MHz) for ZX60-14012L+ and CLF1G0060-10 PA (K=8, Q_l=Q_u=Q=1 and M_l=M_u=M=4) respectively.

Figure 5.6(a) shows the NMSE$^r_{min}$ and ACEPR$^r_{min}$ values obtained using binary search algorithm as explained earlier in Section 5.2.2 for different values of minimum step size Δd^r_{g-min} at LB and UB for ZX60-14012L+ PA. Figure 5.6(b) is for CLF1G0060-10 PA (K=8, Q_l=Q_u=Q=1, and M_l=M_u=M=4). Figure 5.6 shows that NMSE$^r_{min}$ and ACEPR$^r_{min}$ are varying when Δd^r_{g-min} is varying from 0.5 to 0.25. While NMSE$^r_{min}$ and ACEPR$^r_{min}$ are not much improving when Δd^r_{g-min} is decreasing from 0.25. Therefore, the optimum value of Δd^r_{g-min} can be chosen as 0.25 for both PAs inverse modeling.

Using a Binary search algorithm with the condition $\Delta d^r_g \leq 0.25$ (Δd^r_{g-min}=0.25), d^r_g is determined for a minimum value of NMSE. For ZX60-14012L+ PA, the results are d^1_g=0.75, NMSE$^1_{min}$=-47.58 dB, ACEPR$^1_{min}$=-55.62 dBc, d^2_g=0.5, NMSE$^2_{min}$=-48.44 dB, ACEPR$^2_{min}$= -57.47 dBc. For CLF1G0060-10 PA, the results are d^1_g=1.25, NMSE$^1_{min}$=-38.03 dB, ACEPR$^1_{min}$ =-44.97 dBc, d^2_g=0.5, NMSE$^2_{min}$=-41.62 dB, ACEPR$^2_{min}$=-49.80 dBc.

5.2.5.1 PCA implementation for further complexity reduction and improving Numerical Stability

To further reduce the matrix size, PCA as defined in [50] is applied on both the 2D-HMP and 2D-CHMP models, and termed as 2D-HMP-PCA and 2D-CHMP-PCA. PCA also improves the numerical stability of the model.

The numerical instability of a model results from ill-conditioned observation (predistorter) matrix and dispersion of coefficients.

Table 5.2 compares the inverse modeling performance for ZX60-14012L+ PA (I) and CLF1G0060-10 PA (II) of first measurement set-up. The results are for K=8, Q_l=Q_u=Q=1 and M_l=M_u=M=4. While applying PCA, threshold T=99.99999999% is chosen for which NMSE and ACEPR values of the proposed 2D-CHMP-PCA model has similar performances as compared to the 2D-HMP model with reduced complexity. The number of coefficients is reduced for both PAs in both bands (LB or UB).

Figure 5.7(a) shows Power Spectrum Density (PSD) of measured output (PA output) $y_{meas}(n)$ and various model's error at LB (978.4 MHz) and UB (1956.8 MHz) respectively for ZX60-14012L+ PA (K=8, Q_l=Q_u=Q=1 and M_l=M_u=M=4). Figure 5.7(b) is for CLF1G0060-10 PA. From the graph and Table 5.2, it is clear that the ACEPR performance of

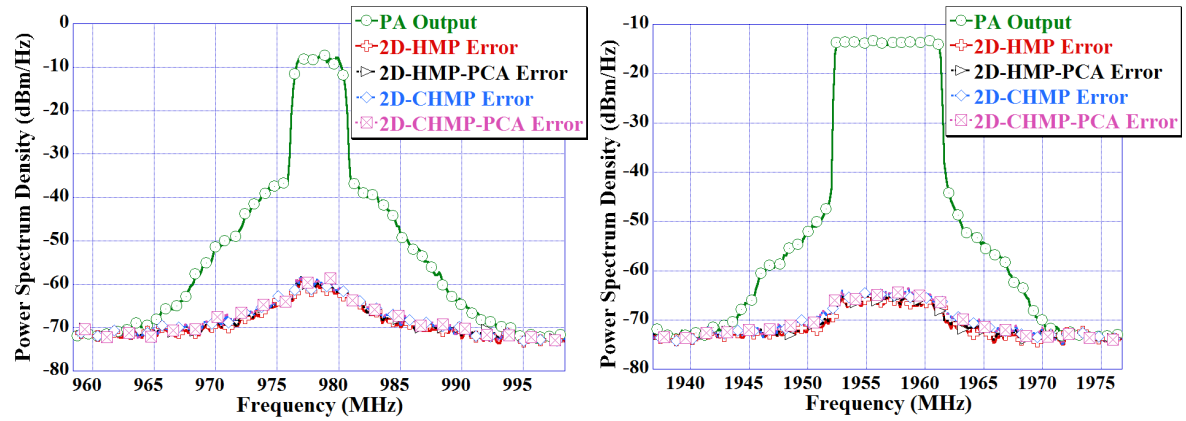

(a)

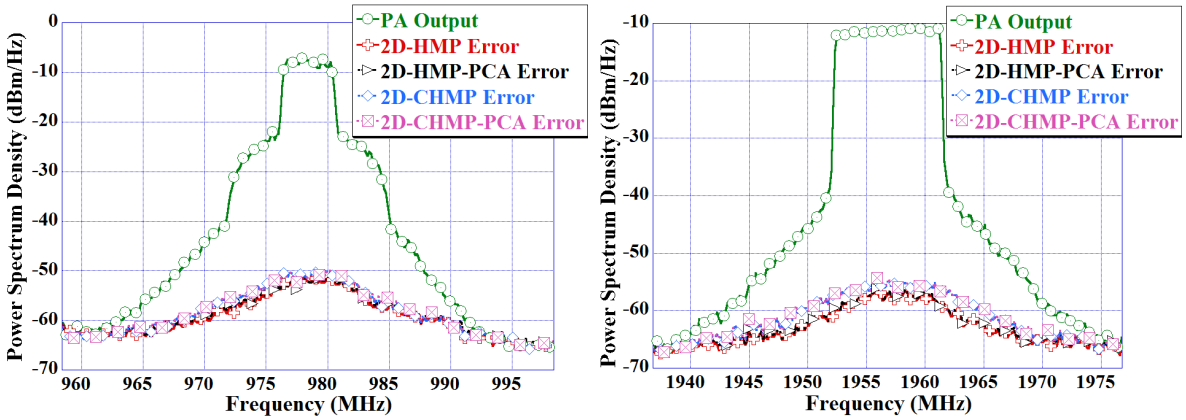

(b)

Figure 5.7: Power Spectrum Density (PSD) of various model's error for (a) ZX60-14012L+ PA at LB and UB respectively, (b) CLF1G0060-10 PA at LB and UB respectively

the proposed 2D-CHMP-PCA model is almost similar to the 2D-HMP model for both PAs.

Table 5.3 compares the condition number and dispersion coefficient of all the models for ZX60-14012L+ PA (I) and CLF1G0060-10 PA (II) of first measurement set-up. 2D-HMP-PCA and 2D-CHMP-PCA models are numerically stable with reduced condition number and dispersion coefficients.

5.2.5.2 Effect of lower-bit Fixed-Point Arithmetic

Earlier in Section 5.2.5.1, the inverse modeling is performed in 64-bit double floating-point DSP. In this section, the inverse modeling is performed at different fixed-point bit-resolutions. As seen from the table 5.3, 2D-HMP and 2D-CHMP models have high condition number and dispersion coefficient. The combination of high condition number and dispersion coefficient will results in large truncation error while extracting coefficients in

Table 5.3: Comparison of Numerical Stability for different Models

PA	Model	LB		UB	
		Cond. No. (dB)	**Disp. Coeff. (dB)**	**Cond. No. (dB)**	**Disp. Coeff. (dB)**
I	**2D-HMP**	112.76	60.83	112.41	55.84
	2D-HMP-PCA	55.93	41.85	55.31	32.83
	2D-CHMP	80.53	30.09	77.58	34.91
	2D-CHMP-PCA	51.79	27.99	51.96	30.29
II	**2D-HMP**	109.26	60.49	108.04	56.79
	2D-HMP-PCA	55.65	33.37	55.67	29.92
	2D-CHMP	79.40	28.14	75.55	35.82
	2D-CHMP-PCA	51.46	32.48	52.28	27.57

the lower-bit fixed-point environment. These effects can be seen in Figure 5.8(a) and Figure 5.8(b). Figure 5.8(a) and Figure 5.8(b) shows the inverse modeling performance in terms of NMSE and ACEPR for different fixed-point bit (16, 24, and 32) resolutions at LB (978.4 MHz) and UB (1956.8 MHz) for ZX60-14012L+ PA and CLF1G0060-10 PA respectively of first measurement set-up. 2D-HMP-PCA and 2D-CHMP-PCA models have good performance at 16-bit resolution, however 2D-HMP-PCA model requires more number of coefficients than the 2D-CHMP-PCA model. 2D-CHMP model has poor performance at 16-bit resolution and converges to 2D-CHMP-PCA performance at 24-bit resolution. 2D-HMP model performance converges at 32-bit resolution. The PCA-based model shows good performance at 16-bit due to lower condition number and dispersion coefficients.

5.2.6 DPD Results

Linearization performance of DPD technique is measured in terms of ACPR and NMSE [30]. The inverse modeling performance can be seen in DPD as well. The coefficients extracted while performing inverse modeling for different models in Section 5.2.5.1 are used to generate predistorted signal for different models. These predistorted signals are passed through PA to produce linearized outputs. Table 5.4 shows the DPD performances performed in 64-bit double floating-point DSP for ZX60-14012L+ PA of first measurement set-up. 2D-

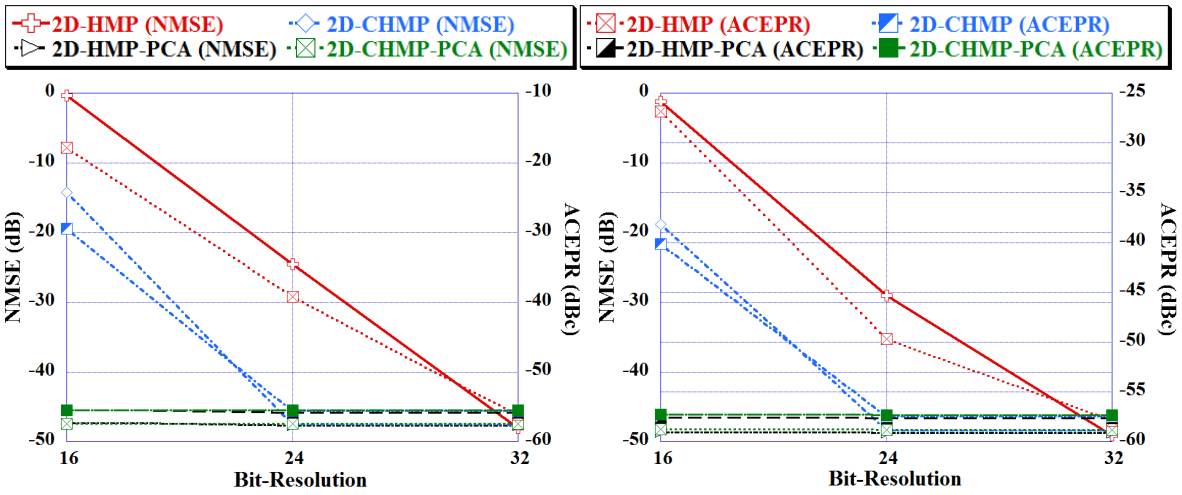

(a)

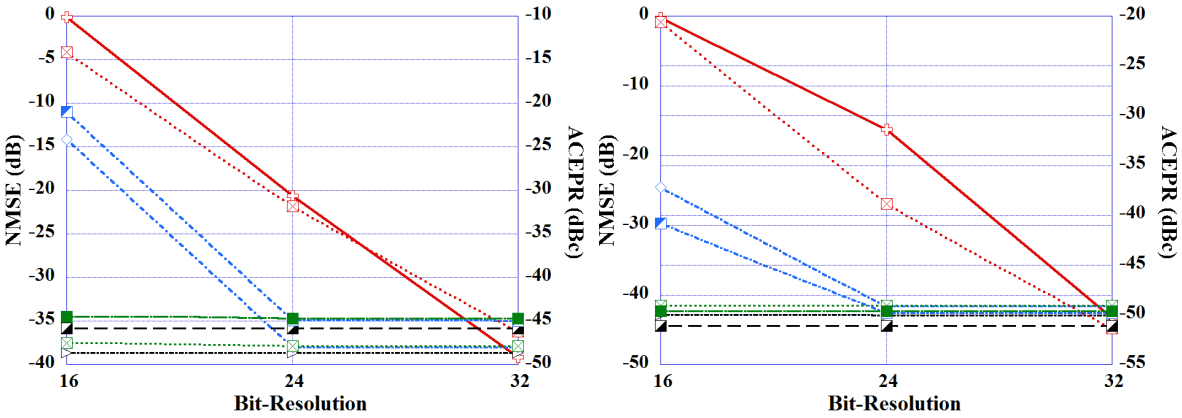

(b)

Figure 5.8: Effect of different bit-resolutions on Inverse Modeling Performance of (a) ZX60-14012L+ PA at LB and UB respectively (b) CLF1G0060-10 PA at LB and UB respectively

Table 5.4: DPD Performances in both bands for ZX60-14012L+ PA

Model	LB			UB		
	NMSE (dB)	ACPR (dBc)	No. of Coeff.	NMSE (dB)	ACPR (dBc)	No. of Coeff.
W/O DPD	-15.24	-28.58	N/A	-16.69	-32.74	N/A
2D-HMP DPD	-40.95	-52.68	540	-41.70	-53.53	540
2D-HMP-PCA DPD	-40.61	-52.41	215	-40.38	-53.09	222
2D-CHMP DPD	-40.44	-52.04	120	-40.25	-53.20	120
2D-CHMP-PCA DPD	-40.10	-51.89	80	-39.96	-53.03	84

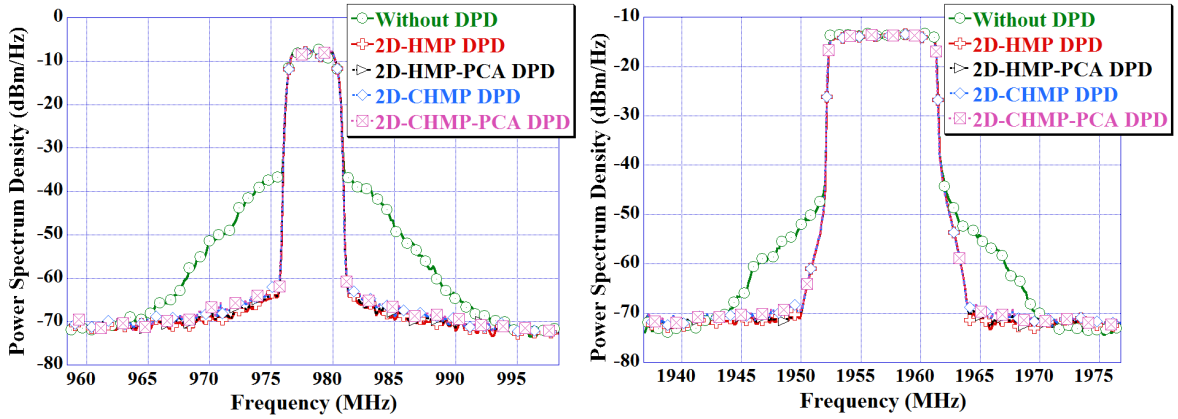

(a) (b)

Figure 5.9: PSD of various model's DPD for ZX60-14012L+ PA at (a) LB and (b) UB.

Table 5.5: DPD Performances in both bands for ZX60-V63+ PA

Model	**LB**			**UB**		
	NMSE (dB)	**ACPR (dBc)**	**No. of Coeff.**	**NMSE (dB)**	**ACPR (dBc)**	**No. of Coeff.**
W/O DPD	-16.53	-28.21	N/A	-18.21	-30.59	N/A
2D-HMP DPD	-36.23	-48.89	540	-39.68	-50.92	540
2D-HMP-PCA DPD	-35.86	-48.67	215	-39.49	-50.81	222
2D-CHMP DPD	-35.41	-48.38	120	-39.02	-50.47	120
2D-CHMP-PCA DPD	-35.26	-48.08	80	-38.89	-50.08	84

HMP DPD improves the NMSE from -15.24 dB to -40.95 dB and -16.69 dB to -41.70 dB for LB and UB respectively i.e. improvement of 25.71 dB and 25.01 dB. In 2D-CHMP-PCA DPD, the NMSE improves by 24.86 dB and 23.27 dB for LB and UB respectively.

In 2D-HMP DPD, ACPR improves by 24.10 dBc and 20.79 dBc. In 2D-CHMP-PCA DPD, the ACPR improves by 23.31 dBc and 20.29 dBc for LB and UB respectively.

It is to be noted here that these results are for L=65536, K=8, Q_l=Q_u=Q=1, M_l=M_u=M=4 and three LS iterations are taken in performing DPD. Thus total computational complexity is reduced by a factor of $3\left(K+1\right)/14 = 1.93$ by using the proposed 2D-CHMP DPD technique with almost same linearization accuracy. Also, the total number of coefficients of the 2D-CHMP model is $\left(K+1\right)/2 = 4.5$ times lesser than the 2D-HMP model.

Figure 5.9(a) and Figure 5.9(b) shows PSD of measured output without DPD, 2D-HMP

Table 5.6: Effect of different bit-resolutions on DPD Performance

Set-Up	Model	Bit-Res.	LB		UB	
			NMSE (dB)	ACPR (dBc)	NMSE (dB)	ACPR (dBc)
I	**2D-HMP**	16	-5.47	-21.34	-7.21	-27.25
		24	-24.48	-40.38	-28.31	-44.99
		32	-40.94	-52.64	-41.51	-53.46
	2D-HMP-PCA	16	-40.42	-52.27	-40.13	-53.01
		24	-40.53	-52.38	-40.35	-53.04
		32	-40.60	-52.41	-40.37	-53.06
	2D-CHMP	16	-16.87	-32.95	-25.44	-43.33
		24	-40.34	-51.97	-40.21	-53.14
		32	-40.44	-52.01	-40.23	-53.16
	2D-CHMP-PCA	16	-40.05	-51.82	-39.68	-52.95
		24	-40.08	-51.84	-39.92	-53.01
		32	-40.10	-51.87	-39.95	-53.03
II	**2D-HMP**	16	-10.53	-21.91	-11.32	-25.76
		24	-21.48	-37.35	-29.72	-39.09
		32	-36.23	-48.87	-39.58	-50.88
	2D-HMP-PCA	16	-35.71	-48.52	-39.25	-50.45
		24	-35.83	-48.61	-39.42	-50.67
		32	-35.84	-48.66	-39.47	-50.77
	2D-CHMP	16	-14.87	-26.35	-20.30	-32.34
		24	-35.36	-48.35	-38.93	-50.21
		32	-35.41	-48.38	-38.97	-50.46
	2D-CHMP-PCA	16	-35.15	-47.97	-38.64	-49.86
		24	-35.24	-48.02	-38.81	-50.04
		32	-35.26	-48.08	-38.86	-50.08

DPD, 2D-HMP-PCA DPD, 2D-CHMP-PCA DPD, and 2D-CHMP-PCA DPD at LB (978.4 MHz) and UB (1956.8 MHz) respectively, for ZX60-14012L+ PA performed in 64-bit double floating-point DSP. ACPR linearization performance of the proposed 2D-CHMP-PCA DPD

Table 5.7: Comparison of FPGA's Memory Resource

Model	**LB**			**UB**		
	Matrix Size ($\times 10^6$)	**Bit-Res.**	**Memory Size (MB)**	**Matrix Size ($\times 10^6$)**	**Bit-Res.**	**Memory Size (MB)**
2D-HMP	35.39	32	141.56	35.39	32	141.56
2D-HMP-PCA	14.09	16	28.18	14.55	16	29.10
2D-CHMP	7.86	24	23.59	7.86	24	23.59
2D-CHMP-PCA	5.24	16	10.49	5.51	16	11.01

is almost similar to the 2D-HMP DPD.

Table 5.5 shows the DPD performances performed in 64-bit double floating-point DSP for ZX60-V63+ PA of second measurement set-up. Again, 2D-HMP DPD and 2D-CHMP-PCA DPD have almost similar linearization performance.

The coefficients extracted while performing inverse modeling for different models in Section 5.2.5.2 at different fixed-point bit-resolutions are used to generate predistorted signal for different models. Table 5.6 shows the DPD performances performed at different fixed-point bit (16, 24, and 32) resolutions for both measurement set-ups. 2D-HMP-PCA and 2D-CHMP-PCA DPD have good performance at 16-bit resolution, however 2D-HMP-PCA model requires more number of coefficients than the 2D-CHMP-PCA model. 2D-CHMP DPD performance converges to 2D-CHMP-PCA DPD performance at 24-bit resolution whereas 2D-HMP DPD performance converges at 32-bit resolution.

The FPGA's memory size required by a model depends on the size of observation (predistorter) matrix and bit-resolution of each sample [45, 71].

As 2D-CHMP-PCA model requires least coefficient i.e. least matrix size and has good linearization performance at 16-bit resolution. Therefore it can be seen in Table 5.7 that the proposed 2D-CHMP-PCA model required least memory size.

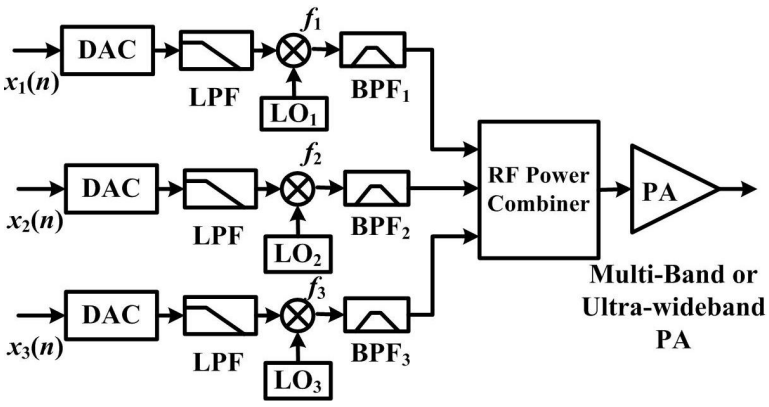

Figure 5.10: Block Diagram of Concurrent Tri-band Transmitter.

5.3 Concurrent Tri-Band DPD Models at Harmonics Frequencies

Figure 5.10 shows the block diagram of the concurrent tri-band transmitter. In the concurrent tri-band transmitter, three different carrier signals are modulated and up-converted at different frequencies. After that, they are combined by a RF power combiner and fed to a multi-band or ultra-wideband PA.

5.3.1 State-of-the-art Tri-Band Digital Predistortion Models

In [98], three-dimensional memory polynomial (3D-MP) was proposed to linearize concurrent tri-band transmitter. In the 3D-MP model [98], the output of a lower-band (LB) is

$$y_1(n) = \sum_{m=0}^{M} \sum_{k=0}^{K-1} \sum_{j=0}^{k} \sum_{i=0}^{j} c_{m,k,j,i}^{(1)} x_1(n-m) |x_1(n-m)|^{k-j} \times |x_2(n-m)|^{j-i} |x_3(n-m)|^{i} \tag{5.13}$$

where M is the memory depth, $c_{m,k,j,i}^{(1)}$ are the coefficients, $x_1(n)$, $x_2(n)$ and $x_3(n)$ are the baseband modulated input signals, $y_1(n)$ is the baseband modulated output of the LB using 3D-MP model and K is the nonlinearity order. The outputs of middle-band (MB) and upper-band (UB) can be easily obtained using a similar expression as in equation (5.13).

The 3D-MP model was modified to 3D Phase aligned Pruned Volterra Model (3D-PAV) in [99] for better linearization of PA. In the 3D-PAV [99], the baseband bi-dimensional model was constructed considering only the input carrier signals and the IMD components that fall

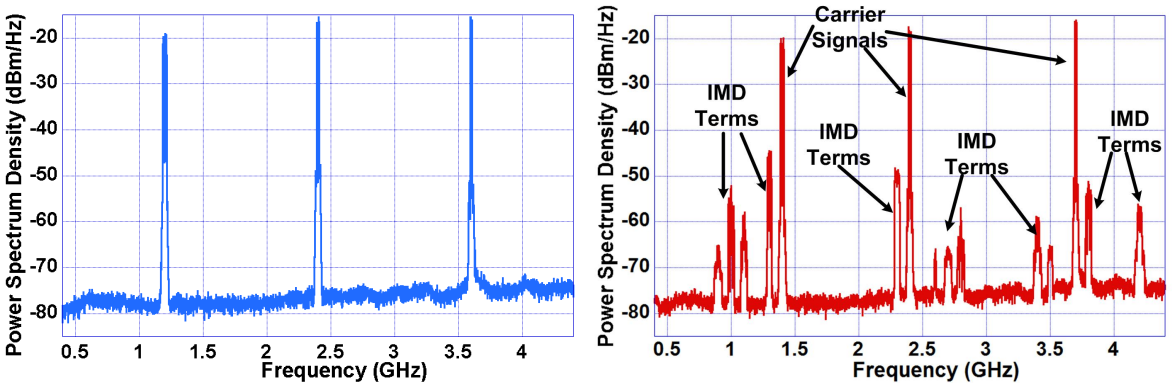

(a) (b)

Figure 5.11: (a) Output of PA when three carrier signals are transmitted at Harmonic Frequencies and (b) Output of PA when first and third carrier signals are shifted from their Harmonic Frequencies.

within the three fundamental frequency bands. The output of a lower-band (LB) is

$$\begin{aligned} y_1(n) = & \sum_{k=0}^{K-1}\sum_{j=0}^{k}\sum_{i=0}^{j} c_{k,j,i,0}^{(1)} x_1(n)\,|x_1(n)|^{k-j}|x_2(n)|^{j-i}|x_3(n)|^{i} \\ & + \sum_{k=0}^{K-1}\sum_{j=0}^{k}\sum_{i=0}^{j}\sum_{m_1=0}^{M_1}\sum_{m_2=0}^{M_2} c_{k,j,i,1}^{(1)} x_1^2(n-m_1)\,x_1^*(n-m_2) \\ & \times|x_1(n-m_1)|^{k-j}|x_2(n-m_1)|^{j-i}|x_3(n-m_1)|^{i} \\ & + \sum_{k=0}^{K-1}\sum_{j=0}^{k}\sum_{i=0}^{j}\sum_{m_1=0}^{M_1}\sum_{m_2=0}^{M_2} c_{k,j,i,2}^{(1)} x_1(n-m_1)\,x_2^*(n-m_2)\,x_2(n-m_1) \\ & \times|x_1(n-m_1)|^{k-j}|x_2(n-m_1)|^{j-i}|x_3(n-m_1)|^{i} \\ & + \sum_{k=0}^{K-1}\sum_{j=0}^{k}\sum_{i=0}^{j}\sum_{m_1=0}^{M_1}\sum_{m_2=0}^{M_2} c_{k,j,i,3}^{(1)} x_1(n-m_1)\,x_3^*(n-m_2)\,x_3(n-m_1) \\ & \times|x_1(n-m_1)|^{k-j}|x_2(n-m_1)|^{j-i}|x_3(n-m_1)|^{i} \end{aligned} \tag{5.14}$$

where M_1 and M_2 are the memory depths and $c_{k,j,i,1}^{(1)}$ are the coefficients of the 3D-PAV model.

However, in these literatures [98, 99], carrier signals are not transmitted at the harmonic frequencies as shown in Figure 5.2.

5.3.2 Analysis of Harmonic Distortions

Figure 5.11(a) shows the output of a PA where three modulated complex input signals x_1, x_2, x_3 are transmitted at carrier frequencies f_1=f=1.2 GHz, f_2=2f=2.4 GHz and f_3=3f=3.6 GHz. The distortions fall at the harmonic frequencies. In order to analyze these distortions, we have shifted first and third carrier signals to be able to observe and quantify the

Table 5.8: IMDs terms in Concurrent Tri-Band Transmitter

Freq. (GHz)	**IMD Terms**	**Freq. (GHz)**	**IMD Terms**
0.9	$x_3(n)\,x_1^{*2}(n)\,e^{j(\omega_3-2\omega_1)nT}$	2.7	$x_1(n)\,x_3(n)\,x_2^{*}(n)\,e^{j(\omega_1+\omega_3-\omega_2)nT}$
1	$x_2(n)\,x_1^{*}(n)\,e^{j(\omega_2-\omega_1)nT}$	2.8	$x_1^{2}(n)\,e^{j(2\omega_1)nT}$
1.1	$x_2^{2}(n)\,x_3^{*}(n)\,e^{j(2\omega_2-\omega_3)nT}$	3.4	$x_2^{2}(n)\,x_1^{*}(n)\,e^{j(2\omega_2-\omega_1)nT}$
1.3	$x_3(n)\,x_2^{*}(n)\,e^{j(\omega_3-\omega_2)nT}$	3.5	$x_2^{3}(n)\,x_3^{*}(n)\,e^{j(3\omega_2-\omega_3)nT}$
2.3	$x_3(n)\,x_1^{*}(n)\,e^{j(\omega_3-\omega_1)nT}$	3.8	$x_1(n)\,x_2(n)\,e^{j(\omega_1+\omega_2)nT}$
2.6	$x_3^{2}(n)\,x_2^{*2}(n)\,e^{j(2\omega_3-2\omega_2)nT}$	4.2	$x_1^{3}(n)\,e^{j(3\omega_1)nT}$

harmonic distortions. This frequency shift is kept small compared to carrier frequency i.e. $\Delta \ll f$ for better observation. Now, three modulated complex input signals x_1, x_2, x_3 are transmitted at carrier frequencies f_1=f+Δ_1=1.2+0.2=1.4 GHz, f_2=2f=2.4 GHz and f_1=3f+Δ_2=3.6+0.1=3.7 GHz respectively. Figure 5.11(b) shows the IMDs generated around these carrier signals. The IMDs are at 0.9, 1, 1.1, 1.3, 2.3, 2.6, 2.7, 2.8, 3.4, 3.5, 3.8 and 4.2 GHz. Table 5.8 shows the IMDs corresponding to these frequencies.

In practical scenarios of harmonic CA modulated signals, some of the IMDs and CMDs generated by the PA would fall within or nearby the bands of the carriers of the input signals. To illustrate the above, the IMD terms $\omega_3-2\omega_1$, $\omega_2-\omega_1$, $2\omega_2-\omega_3$ and $\omega_3-\omega_2$ fall close by ω_1. Similarly, these IMD terms $\omega_3-\omega_1$, $2\omega_3-2\omega_2$, $\omega_1+\omega_3-\omega_2$ and $2\omega_1$ fall close by ω_2. Similarly, these IMD terms $2\omega_2-\omega_1$, $3\omega_2-\omega_3$, $\omega_1+\omega_2$ and $3\omega_1$ fall close by ω_3. When the shift from first and third harmonic is 0, i.e. ω_1=ω , ω_2=2ω , ω_3=3ω , then these IMD terms fall directly on ω, 2ω and 3ω frequencies.

5.3.3 Proposed 3D Harmonic Memory Polynomial (3D-HMP) and Volterra Spline (3D-HVS) Models for Harmonic Distortions

The 3D-MP and 3D-PAV models do not contain these IMD terms and thus would be insufficient to capture harmonic distortions when the three modulated complex input signals are transmitted at harmonic frequencies ω_1=ω , ω_2=2ω and ω_3=3ω.

By including the above IMD terms in the model, the outputs of the transmitter would be

$$\begin{aligned} y_1(n) &= \sum_{m=0}^{M} x_1(n-m)\, H_0^{(1)}(n-m) + \sum_{m=0}^{M} x_3(n-m)\, x_2^*(n-m)\, H_1^{(1)}(n-m) \\ &+ \sum_{m=0}^{M} x_2(n-m)\, x_1^*(n-m)\, H_2^{(1)}(n-m) + \sum_{m=0}^{M} x_3(n-m)\, x_1^{*2}(n-m)\, H_3^{(1)}(n-m) \\ &+ \sum_{m=0}^{M} x_2^2(n-m)\, x_3^*(n-m)\, H_4^{(1)}(n-m) \end{aligned} \tag{5.15}$$

$$\begin{aligned} y_2(n) &= \sum_{m=0}^{M} x_2(n-m)\, H_0^{(2)}(n-m) + \sum_{m=0}^{M} x_3(n-m)\, x_1^*(n-m)\, H_1^{(2)}(n-m) \\ &+ \sum_{m=0}^{M} x_3^2(n-m)\, x_2^{*2}(n-m)\, H_2^{(2)}(n-m) + \sum_{m=0}^{M} x_1^2(n-m)\, H_3^{(2)}(n-m) \\ &+ \sum_{m=0}^{M} x_1(n-m)\, x_3(n-m)\, x_2^*(n-m)\, H_4^{(2)}(n-m) \end{aligned} \tag{5.16}$$

$$\begin{aligned} y_3(n) &= \sum_{m=0}^{M} x_3(n-m)\, H_0^{(3)}(n-m) + \sum_{m=0}^{M} x_1(n-m)\, x_2(n-m)\, H_1^{(3)}(n-m) \\ &+ \sum_{m=0}^{M} x_2^2(n-m)\, x_1^*(n-m)\, H_2^{(3)}(n-m) + \sum_{m=0}^{M} x_1^3(n-m)\, H_3^{(3)}(n-m) \\ &+ \sum_{m=0}^{M} x_2^3(n-m)\, x_3^*(n-m)\, H_4^{(3)}(n-m) \end{aligned} \tag{5.17}$$

where $H_p^{(r)}(n-m)$=$H_p^{(r)}(|x_1(n-m)|, |x_2(n-m)|, |x_3(n-m)|)$, p denotes the IMD term, $r \in \{1,\ 2,\ 3\}$ denotes the LB, MB and UB.

For the proposed 3D-HMP model,

$$H_p^{(r)}(n-m) = \sum_{k=0}^{K-1} \sum_{j=0}^{k} \sum_{i=0}^{j} d_{m,k,j,i,p}^{(r)} |x_1(n-m)|^{k-j} |x_2(n-m)|^{j-i} |x_3(n-m)|^i \tag{5.18}$$

where $d_{m,k,j,i,p}^{(r)}$ are the coefficients for the p^{th} IMD term of r^{th} band of the 3D-HMP model.

To model the nonlinearity, instead of polynomial, cubic splines can also be used, which is notified as 3D-HVS model

$$H_p^{(r)}(n-m) = \sum_{k=0}^{K_S} \sum_{j=0}^{K_S} \sum_{i=0}^{K_S} d_{m,k,j,i,p}^{(r)} \varphi_{kji}(|x_1(n-m)|, |x_2(n-m)|, |x_3(n-m)|) \tag{5.19}$$

where

$$\begin{aligned} \varphi_{kji}(|x_1(n)|, |x_2(n)|, |x_3(n)|) = \sum_{u=0}^{3} \sum_{v=0}^{3} \sum_{w=0}^{3} &(|x_1(n)| - |x_{1,k}(n)|)^u \\ &\times (|x_2(n)| - |x_{2,j}(n)|)^v (|x_3(n)| - |x_{3,i}(n)|)^w \end{aligned} \tag{5.20}$$

where $x_{1,k}(n)$ is the value of $x_1(n)$ at the knot k, $x_{2,j}(n)$ is the value of $x_2(n)$ at the knot j and $x_{3,i}(n)$ is the value of $x_3(n)$ at the knot i. K_s denotes the number of splines [49].

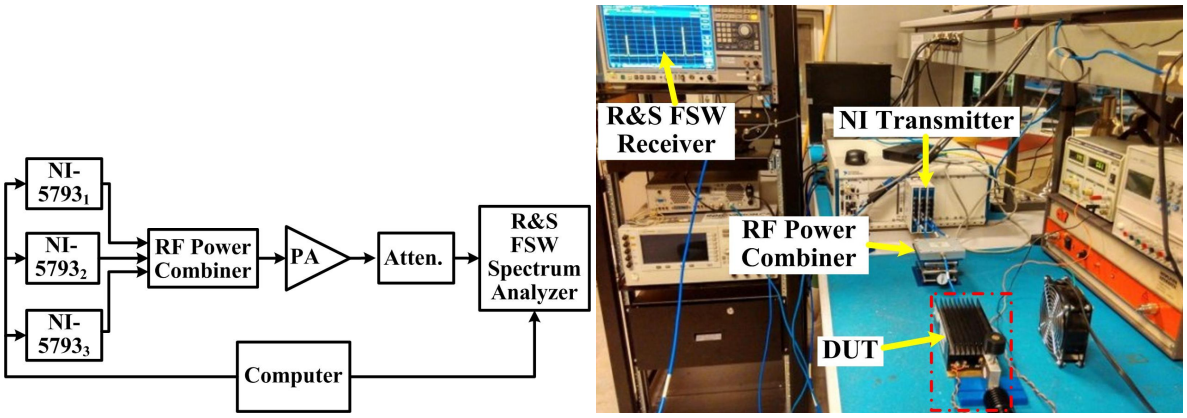

(a) (b)

Figure 5.12: (a) Block Diagram and (b) Photograph of Measurement and Control setup.

Table 5.9: Behavioral Modeling Results for different models

Model	LB		MB		UB	
	NMSE (dB)	ACEPR (dBc)	NMSE (dB)	ACEPR (dBc)	NMSE (dB)	ACEPR (dBc)
3D-MP	-23.35	-42.04/-35.53	-24.04	-35.42/-35.92	-28.23	-46.24/-41.33
3D-PAV	-26.12	-43.63/-38.43	-27.83	-38.95/-38.87	-30.24	-47.76/-44.23
3D-HVS	-41.62	-54.75/-54.47	-42.83	-55.21/-54.94	-40.81	-54.57/-55.07
3D-HMP	-41.69	-55.62/-55.36	-42.92	-55.84/-55.61	-40.95	-55.42/-55.93

Table 5.10: Coefficients comparison between models

Model	Total Number of Coefficients	
	General case	Test Case
3D-MP	$(M+1)\,K\,(K+1)\,(K+2)\,/2$	672
3D-PAV	$K\,(K+1)\,(K+2)\,/2+3(M_1+1)(M_2+1)\,(K-2)\,(K-1)\,K/2$	2328
3D-HVS	$15(M+1)(K_S+1)^3$	3840
3D-HMP	$5(M+1)K\,(K+1)\,(K+2)\,/2$	3360

5.3.4 Measurement Testbed for Concurrent Tri-Band DPD

Figure 5.12 shows the measurement setup used for the concurrent tri-band transmitter. It consists of NI transmitter (PXIe-1075), RF power combiner, ZHL-42 RF PA, attenuators

Table 5.11: DPD Results for different models

Model	**LB**		**MB**		**UB**	
	NMSE (dB)	**ACEPR (dBc)**	**NMSE (dB)**	**ACEPR (dBc)**	**NMSE (dB)**	**ACEPR (dBc)**
W/O DPD	-14.47	-36.33/ -31.58	-15.36	-29.79/ -29.97	-16.32	-34.88/ -32.40
3D-MP DPD	-21.54	-40.41/ -34.67	-23.48	-34.25/ -34.48	-26.12	-44.36/ -39.93
3D-PAV DPD	-24.26	-42.15/ -36.86	-26.75	-37.49/ -37.47	-28.63	-46.68/ -42.71
3D-HVS DPD	-40.18	-52.41/ -52.22	-41.29	-54.32/ -53.80	-39.12	-53.75/ -54.62
3D-HMP DPD	-40.32	-53.53/ -53.19	-41.37	-55.27/ -55.01	-39.43	-54.99/ -55.59

and R&S FSW spectrum analyzer as a transmitter observation receiver. Three different LTE signals of bandwidth 30 MHz, 20 MHz and 15 MHz with PAPR of 12.86 dB, 13.02 dB and 12.98 dB respectively are used. NI transmitter (PXIe-1075) have three RF channel outputs (NI-5793). These three RF channels are phase synchronized by reference clock of the transmitter. 30 MHz 101 LTE signal is transmitted at 1.2 GHz, 20 MHz 1001 LTE signal is transmitted at 2.4 GHz and 15 MHz 101 LTE signal is transmitted at 3.6 GHz. These three RF signals are combined by a RF power combiner and are used to drive ZHL-42 RF PA. ZHL-42 PA has 28 dBm output power at 1 dB gain compression and operating frequency range from 0.7 GHz to 4.2 GHz. The output RF signal of PA is attenuated and then captured by R&S FSW spectrum analyzer at 1.2 GHz, 2.4 GHz and 3.6 GHz respectively. The reference clock from the transmitter is provided to the receiver for synchronization. R&S FSW spectrum analyzer down converts the RF signals to baseband. The output and input baseband signal of each frequency band are time aligned in Matlab software. The signal is further processed by Matlab software to perform DPD.

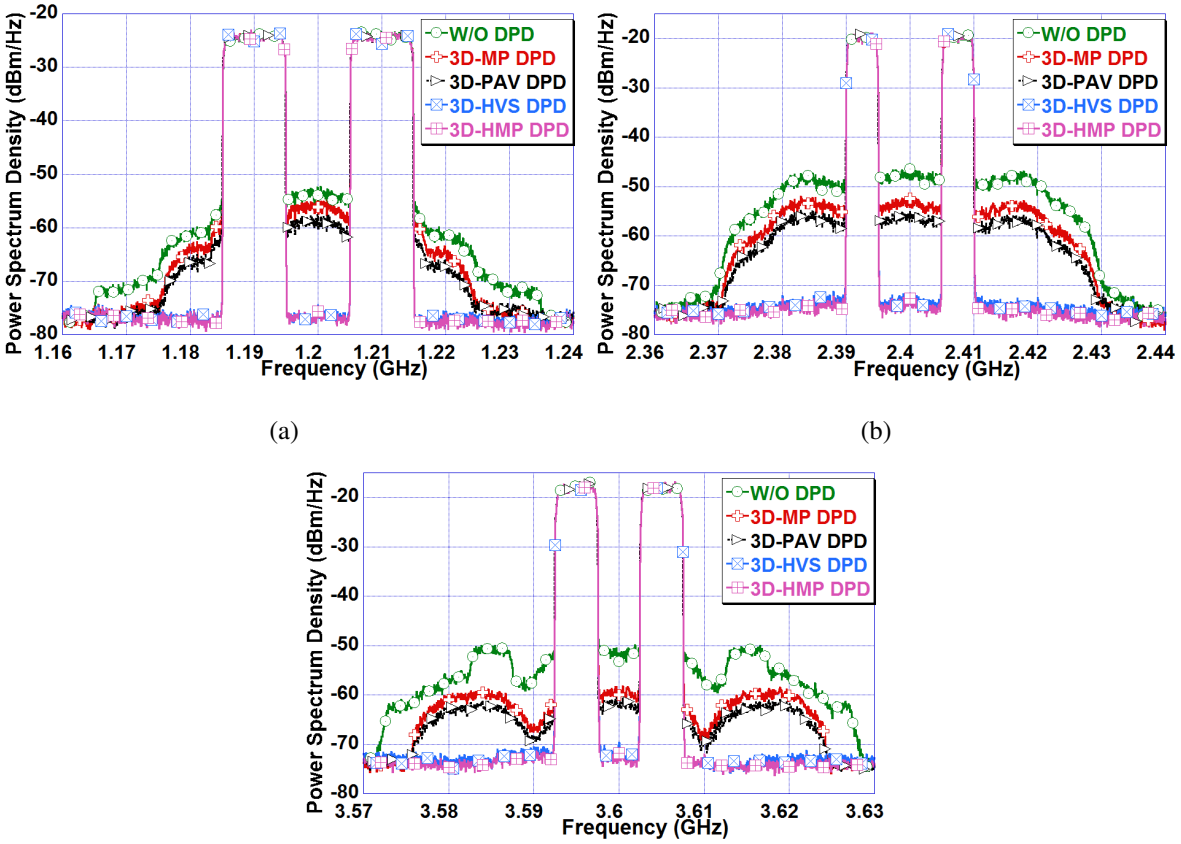

Figure 5.13: Frequency Power Spectra of various DPD model's outputs at (a) LB, (b) MB and (c) UB.

5.3.5 Results

5.3.5.1 Behavioral Modeling Results

Table 5.9 shows the behavioral modeling results for different models in terms of NMSE and ACEPR. From Table 5.9, the 3D-HMP and 3D-HVS have better NMSE and ACEPR performance as compared to state-of-the-art models, approximately 10–15 dB improvement in NMSE from 3D-PAV model, which is expected as the state-of-the-art models do not contain harmonic terms shown in section 5.3.2. It is to be noted that 3D-MP model constitutes an only first term of equations (5.15), (5.16) and (5.17). These results are for M=3, M_1=3, M_2=2, K=6, and K_S=3. Table 5.10 shows the coefficients comparison between different models and it can be observed that inclusion of harmonic terms leads to higher number of coefficients with much better behavioral modeling performance.

5.3.5.2 DPD Results

Table 5.11 shows the linearization results for different models in terms of NMSE and ACPR. From Table 5.11, the 3D-PAV DPD model has better NMSE and ACPR performance than 3D-MP DPD model. However, the 3D-PAV DPD's NMSE performance is much lesser than the acceptable performance of -35 dB. The proposed 3D-HMP and 3D-HVS DPD models have better NMSE and ACPR performance as compared to 3D-MP and 3D-PAV DPD models. The NSME and ACPR have improved approximately by 11–16 dB and 10–18 dBc from 3D-PAV DPD model. Figure 5.13 shows the frequency power spectra of various DPD models' outputs at the LB, MB, and UB. As it can be seen from the Figure 5.13, the proposed 3D-HMP and 3D-HVS DPD models have better ACPR performance.

5.4 Conclusion

In the first part of this chapter, we proposed the 2D-CHMP model to linearize the nonlinearity of concurrent dual-band transmitters in ultra-wideband applications where the second signal band lies at the harmonic frequency band of the first signal band with reduced complexity as compared to the state-of-the-art 2D-HMP model. The proposed 2D-CHMP model is constructed by simplifying the envelope terms of the 2D-HMP model. The total number of coefficients of the 2D-CHMP model is $(K+1)/2$ times lesser than the 2D-HMP model. Also, the computational complexity of 2D-CHMP DPD is $(K+1)/6$ and $3(K+1)/14$ times lesser than 2D-HMP DPD for two and three LS iterations respectively. The proposed 2D-CHMP-PCA model required least FPGA's memory resource, thus making it suitable for low-cost FPGA implementation.

In the second part of this chapter, the 3D-HMP and 3D-HVS DPD models have been presented and experimentally verified to mitigate the in-band harmonic distortions, CMDs and IMDs generated by ultra-wideband PA when carrier signals are transmitted at harmonic frequencies in the concurrent tri-band transmitter. To establish the need of this DPD model, it is compared with the state-of-the-art DPD models. It has been experimentally verified that the state-of-the-art DPD models are not able to capture in-band harmonic distortions and their NMSE and ACPR's performance are not meeting the acceptable performance. Whereas the NMSE and ACPR's performance of proposed DPD models are improved approximately by 23–26 dB and 18–20 dBc respectively over without DPD signal. The complexity of the

proposed DPD models can be reduced by pruning techniques like PCA.

The next chapter deals with the DPD models for the mitigation of imperfections present in MIMO transmitters.

Chapter 6

DPD Model for mitigation of imperfections in MIMO Transmitters

6.1 Introduction

In order to meet the ambitious requirements of improved capacity and increased data rate [105], MIMO topology based transceivers are being perceived as a viable solution [106,107]. MIMO streams can increase the data rate or system capacity as many times as the number of branches of MIMO transceivers [108–110]. However, at the transmitter side, crosstalk may occur between the RF branches, when they are placed on the same chip [111]. This adds to the signal distortion, which is already generated by the nonlinearity of the RF PAs. In addition, there may be distortion components such as impairments due to local oscillator (LO) leakage and in-phase and quadrature (I/Q) imbalance in quadrature modulators within a practical MIMO transmitter. These nonlinearities and impairments need to be compensated for distortion-free signal transmission.

There are various DPD models such as Volterra-Series [22], MP [24] and GMP [27] available for linearization of PA nonlinearities in single-input single-output (SISO) transmitter. There are few DPD models proposed in [112–118] to jointly compensate I/Q imbalance and PA nonlinearities in SISO transmitters. In case of MIMO transmitters, these models are proposed for compensation of crosstalk and PA nonlinearities [54–61]. Recently in [119], a DPD model is presented for joint mitigation of I/Q imbalance, dc offset, crosstalk and PA nonlinearity in the MIMO transmitters. The drawbacks of such DPD model is that it requires extraction of coefficients and inverse modeling of each transmitter paths i.e. for

$P \times P$ MIMO, the coefficient extraction and inverse modeling are performed P times. As this model requires high number of coefficients, extracting coefficients P times in massive MIMO would result in a high coefficients extraction burden. Therefore, complexity is one of the main concerns in DPD solutions for MIMO transmitters.

This chapter proposes a Neural Network (NN)-based DPD model, which can perform inverse modeling for P transmitters of MIMO with a single DPD block [120]. NN-based DPD model will provide ease of adaptability for multi-dimensions of MIMO transmitters e.g. a single NN can work for 2×2 MIMO as well as for $P \times P$ MIMO instead of P different DPD blocks.

This chapter also proposes an efficient polynomial-based DPD model for 4×4 MIMO transmitters while considering the decay effect of crosstalk level between the transmitting branches. This model is constructed by accounting that the crosstalk would be weaker in strength as compared to the actual carrier input signal in a given branch of a MIMO transmitter. The constructed DPD model will require less number of mathematical operations, less number of coefficients and consequently less coefficient's extraction burden on a digital signal processor using least square (LS) method as compared to the conventional DPD models. As the effects of crosstalk between branches of MIMO transmitters will decay significantly beyond the second adjacent branches with respect to a given branch of MIMO transmitter, the proposed model can be extended to large-scale MIMO transmitters as a cluster of 4×4 transmitters.

This chapter is organized as follows: Section 6.2 describes the impairments present in MIMO transmitters and existing DPD algorithms for MIMO transmitters. Section 6.3 proposes the NN-based DPD model and presents its measurement results. Section 6.4 proposes the polynomial-based DPD model and presents its measurement results. Section 6.5 presents the conclusion.

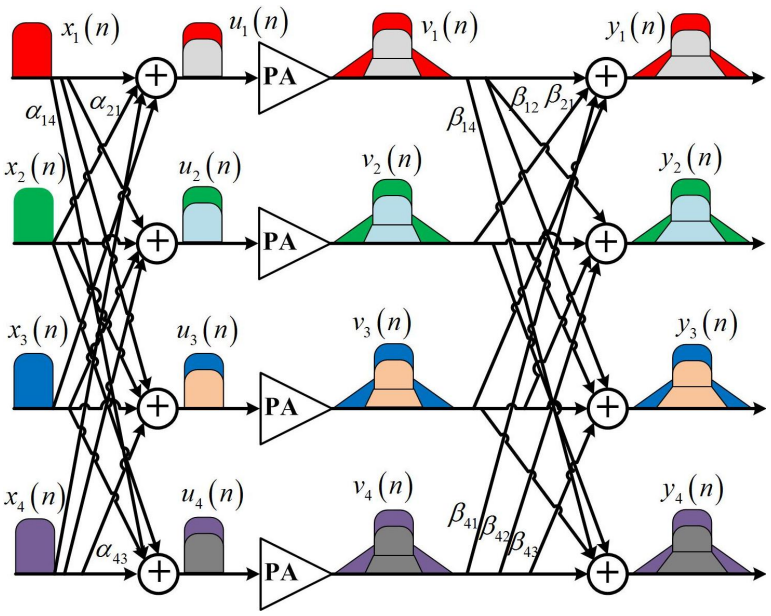

Figure 6.1: 4×4 MIMO transmitters with nonlinear crosstalk and linear crosstalk.

6.2 MIMO Transmitter

Direct-conversion transmitter is known to suffer ill-effects of gain imbalance, phase imbalance and LO leakage on the transmitted signal. In MIMO transmitters, signals are transmitted at the same carrier frequency in different transmitters' paths as shown in Figure 2.6 in chapter 2. Hence, the effect of above-mentioned impairments magnifies, when the signal is distorted due to PA nonlinearity and multi-branch crosstalk.

6.2.1 Crosstalk

Crosstalk is induced due to the coupling effects between different transmitters' paths or leakage through the common LO. Crosstalk can be categorized as linear and nonlinear. Linear crosstalk occurs after the PA and can be removed at the receiver. Figure 6.1 shows the 4×4 MIMO transmitters with nonlinear crosstalk and linear crosstalk. In Figure 6.1, coupling factors α_{12}, α_{13}, α_{14},... α_{41},... and α_{43} denotes the effects of nonlinear crosstalk. In Figure 6.1, coupling factors β_{12}, β_{13}, β_{14},... β_{41},... and β_{43} denotes the effects of linear crosstalk. Generally, MIMO crosstalk has a coupling factor between -15 dB to -30 dB [57].

6.2.2 *I/Q* Imbalance

In a MIMO transmitter, I/Q imbalance occurs due to a mismatch between the in-phase (I) and quadrature-phase (Q) signal paths in the modulator. For $P \times P$ MIMO transmitters, let $x_p(n)$ denote the p^{th} transmitter path baseband input signal, where $p = 1, 2, \cdots P$. Due to I/Q imbalance, signal at the output of quadrature modulator is

$$\hat{x}_p(n) = a_p x_p(n) + b_p x_p^*(n) \tag{6.1}$$

where

$$a_p = \cos(\theta_p/2) + j\varepsilon_p \sin(\theta_p/2) \tag{6.2}$$

$$b_p = \varepsilon_p \cos(\theta_p/2) + j \sin(\theta_p/2) \tag{6.3}$$

In equations (6.2) and (6.3), ε_p and θ_p represents the p^{th} transmitter path's gain imbalance and phase imbalance respectively. For a balanced modulator, ε_p=1 and θ_p=0°. I/Q imbalance can be represented by a metric known as image rejection ratio (IRR) [119]. It is defined as

$$\Gamma_p \text{ (dB)} = 20\log_{10}(b_p/a_p) \tag{6.4}$$

Generally, IRR in RF transmitters ranges from -20 dB to -40 dB [119].

6.2.3 Existing DPD Models for MIMO Transmitter

6.2.3.1 Crossover Memory Polynomial Model (COMPM)

In [54], the output of this model is given for 2×2 MIMO as shown in equation (2.26). This model can be straightforward mathematically derived for higher order of MIMO transmitters using the equation (2.26). The output of a first transmitter's path in 3×3 MIMO using this model is

$$\begin{aligned} y_1(n) = &\sum_{m=0}^{M}\sum_{k=0}^{K-1} c_{m,k}^{(1)} \cdot x_1(n-m) \cdot |x_1(n-m)|^k \\ &+ \sum_{m=0}^{M}\sum_{k=0}^{K-1} d_{m,k}^{(1)} \cdot x_2(n-m) \cdot |x_2(n-m)|^k \\ &+ \sum_{m=0}^{M}\sum_{k=0}^{K-1} e_{m,k}^{(1)} \cdot x_3(n-m) \cdot |x_3(n-m)|^k \end{aligned} \tag{6.5}$$

where M is the memory depth, $x_1(n)$, $x_2(n)$ and $x_3(n)$ are the baseband modulated input signals of different transmitter's path, $c_{m,k}^{(1)}$, $d_{m,k}^{(1)}$ and $e_{m,k}^{(1)}$ are the coefficients and K is the nonlinearity order of the COMP model. The second and third outputs of the 3×3 MIMO transmitters can be obtained easily using a similar expression as in equation (6.5).

6.2.3.2 Parallel Hammerstein (PH) Model

In [55], the output of this model is given for 2×2 MIMO as shown in equation (2.27). This model can be straightforward mathematically derived for higher order of MIMO transmitters using the equation (2.27). The output of a first transmitter's path in 3×3 MIMO using this model is

$$\begin{aligned} & y_1(n) = f\left(x_1(n), x_2(n), x_3(n)\right) \\ & = \sum_{m=0}^{M} \sum_{k=0}^{K-1} \sum_{j=0}^{k} \sum_{i=0}^{j} c_{m,k,j,i}^{(1)} \cdot x_1(n-m) \cdot |x_1(n-m)|^{k-j} |x_2(n-m)|^{j-i} |x_3(n-m)|^{i} \\ & + \sum_{m=0}^{M} \sum_{k=0}^{K-1} \sum_{j=0}^{k} \sum_{i=0}^{j} d_{m,k,j,i}^{(1)} \cdot x_2(n-m) \cdot |x_1(n-m)|^{k-j} |x_2(n-m)|^{j-i} |x_3(n-m)|^{i} \\ & + \sum_{m=0}^{M} \sum_{k=0}^{K-1} \sum_{j=0}^{k} \sum_{i=0}^{j} e_{m,k,j,i}^{(1)} \cdot x_3(n-m) \cdot |x_1(n-m)|^{k-j} |x_2(n-m)|^{j-i} |x_3(n-m)|^{i} \end{aligned} \tag{6.6}$$

where $c_{m,k,j,i}^{(1)}$, $d_{m,k,j,i}^{(1)}$ and $e_{m,k,j,i}^{(1)}$ are the coefficients of PH model.

The PH model has been shown to have better linearization performance than COMP model in presence of crosstalk, but requires a large of coefficients [57].

COMP and PH models linearize PA and remove crosstalk. However, both these models are insufficient to mitigate the transmitter imperfections due to I/Q imbalance and dc offset.

6.2.3.3 Augmented Complex Conjugate Parallel Hammerstein (ACC-PH) Model

In [115], complex conjugate function and a dc term were added to compensate for the I/Q imbalance and dc offset in SISO. Similarly, the complex conjugate function of PH model and a dc term can be added to PH model to compensate for the I/Q imbalance and dc offset in addition to the PA nonlinearity and crosstalk. The output of this model for the first branch of the MIMO transmitter is as follows:

$$y_1(n) = f\left(x_1(n), x_2(n), x_3(n)\right) + f\left(x_1^*(n), x_2^*(n), x_3^*(n)\right) + c' \tag{6.7}$$

where $f\left(x_1(n), x_2(n), x_3(n)\right)$ is a function as defined in equation (6.6). This model linearizes PA and mitigates crosstalk, I/Q imbalance, and dc offset. The drawback of this model is that it requires extraction of coefficients and inverse modeling of each transmitter paths, i.e. for $P \times P$ MIMO, the coefficient extraction and inverse modeling is performed P times. This model requires high number of coefficients and extracting coefficients P times in massive MIMO would result in high coefficients extraction burden.

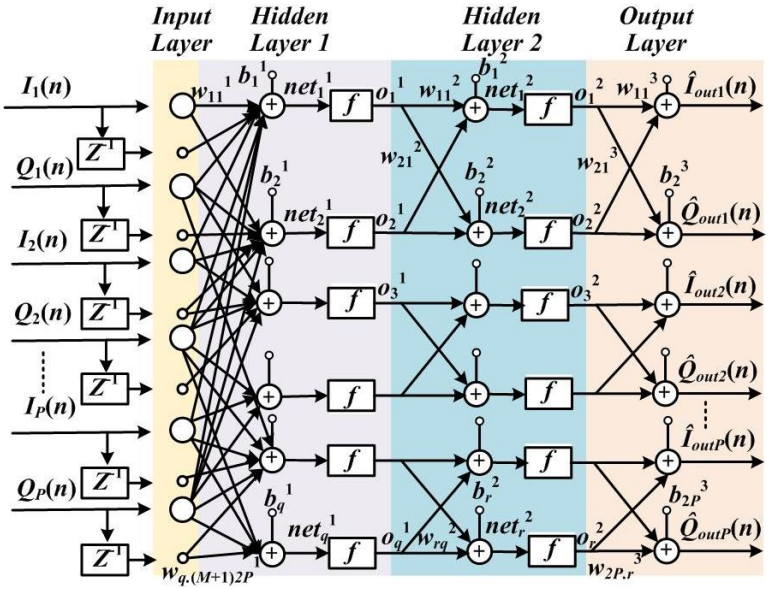

Figure 6.2: Real-valued time-delay feedforward backpropagation-based Neural Network.

6.3 Proposed Neural Network based DPD Model

Figure 6.2 shows the real-valued time-delay NN [121–125]. The input vector contains present and past values of I and Q. The input vector is defined as

$$\begin{aligned} X = [&I_1(n), \cdots, I_1(n-m), Q_1(n), \cdots, Q_1(n-m), \\ &I_2(n), \cdots, I_2(n-m), Q_2(n), \cdots, Q_2(n-m), \\ &\cdots, I_P(n), \cdots, I_P(n-m), Q_P(n), \cdots, Q_P(n-m)] \end{aligned} \tag{6.8}$$

where $I_P(n)$, $Q_P(n)$ are the I and Q components of baseband input signal of P^{th} transmitter branch at n^{th} time instant. z^{-1} represents the unit delay operator. The feedforward backpropagation neural network is used.

6.3.1 Feedforward Propagation

During feedforward computation, data propagates from neurons of a lower layer to upper layer. As shown in Figure 6.2, two hidden layers are used in this neural network. The net input in layer l+1is given by

$$net_j^{l+1} = \sum_{i=1}^{q} w_{ji}^{l+1} o_i^l + b_j^{l+1} \tag{6.9}$$

where w_{ji}^{l+1} represents the synaptic weight between the i^{th} input from the previous layer to the j^{th} neuron of the present layer. Initially, weights are set in the interval of [-0.8, 0.8] and

during backward propagation, weights are adjusted to reduce the error. q represents the total number of neurons in the previous layer and b_j^{l+1} denotes bias of the j^{th} neuron in the $l+1^{th}$ layer. The output of neuron j at $l+1^{th}$ layer is

$$o_j^{l+1} = f\left(net_j^{l+1}\right) \tag{6.10}$$

The hidden layers have the hyperbolic tangent function, as the activation function, f. It maps the nonlinearity between -1 and 1. The output of any layer works as an input to the next layer. The outputs of hidden neurons are linearly summed up at the output layer.

6.3.2 Backward Propagation

During backward propagation, the performance index for the NN is calculated as

$$\begin{aligned} V = & \tfrac{1}{2N}\sum_{n=1}^{N}\left[I_{out1}(n) - \hat{I}_{out1}(n)\right]^2 + \left[Q_{out1}(n) - \hat{Q}_{out1}(n)\right]^2 \\ & + \tfrac{1}{2N}\sum_{n=1}^{N}\left[I_{out2}(n) - \hat{I}_{out2}(n)\right]^2 + \left[Q_{out2}(n) - \hat{Q}_{out2}(n)\right]^2 \\ & \cdots + \tfrac{1}{2N}\sum_{n=1}^{N}\left[I_{outP}(n) - \hat{I}_{outP}(n)\right]^2 + \left[Q_{outP}(n) - \hat{Q}_{outP}(n)\right]^2 \\ & = \tfrac{1}{2}\sum_{n=1}^{N}\left\{e_n^T e_n\right\} \end{aligned} \tag{6.11}$$

where e is the error, $I_{outP}(n)$ and $Q_{outP}(n)$ are the I and Q components of the actual base-band outputs of P^{th} transmitter branch of MIMO, $\hat{I}_{outP}(n)$ and $\hat{Q}_{outP}(n)$ are the I and Q components of the outputs from output-layer neurons of the NN model.

Then the Levenberg-Marquardt algorithm [122] is used, which is an approximation to Gauss-Newtons method. According to this algorithm, the parameter V is minimized with respect to a parameter $\mathbf{u}$ which depends on synaptic weights and biases. During backward propagation $\mathbf{u}$ is updated as

$$\mathbf{u}^{k+1} = \mathbf{u}^k - \left[\mathbf{J}^T\mathbf{J} + \mu\mathbf{I}\right]^{-1}\mathbf{J}^T\mathbf{e} \tag{6.12}$$

where

$$\mathbf{u} = \left[w_{11}^1 \cdots w_{q.2P(M+1)}^1 b_1^1 \cdots b_q^1 w_{11}^2 \cdots w_{rq}^2 b_1^2 \cdots b_r^2 w_{11}^3 \cdots w_{2Pr}^3 b_1^3 \cdots b_{2P}^3\right] \tag{6.13}$$

where $\mathbf{J}$ is the Jacobian matrix calculated over error matrix $\mathbf{e}$ with respect to $\mathbf{u}$. q and r are the numbers of neurons of two hidden layers. M and P are the memory depth and number of transmitter's branches in MIMO. Whenever V increases, μ is multiplied by some factor β.

Whenever V decreases, μ is divided by some factor β. Initially μ and β are set equal to 0.01 and 10 respectively. The whole procedure is iterated until the good performance is achieved by NN.

The calculation of Jacobian Matrix $\mathbf{J}$ is shown in the appendix A.

6.3.3 Coefficient Complexity comparison between DPD models

In conventional DPD models like COMPM, PH and ACC-PH models, the least square (LS) algorithm is applied to the observation (predistorter) matrix for calculation of the model's coefficients. To implement least square extraction, pseudo-inverse method is used. Let

$$\mathbf{y} = \mathbf{X}\mathbf{A} \tag{6.14}$$

where $\mathbf{y}$ is a $N\times 1$ vector representing the N samples of the output signal, $\mathbf{A}$ is a vector of coefficients, $\mathbf{X}$ is an observation (predistorter) matrix and its size is $N \times$ (No of Coeff.). Then using pseudo inverse method, $\mathbf{A}$ is calculated as

$$\mathbf{A} = \left(\mathbf{X}^H\mathbf{X}\right)^{-1}\mathbf{X}^H\mathbf{y} \tag{6.15}$$

In NN, Levenberg-Marquardt algorithm [122] also uses LS algorithm to the batch training of multi-layer perceptrons. According to this algorithm, $\mathbf{u}$ is updated as in equation (6.12). The size of Jacobian matrix depends on $N \times$ (No of Weights and Biases). It is defined as

$$\mathbf{J} = \begin{bmatrix} \frac{\partial e(1)}{\partial w_{11}} & \frac{\partial e(1)}{\partial w_{12}} & \cdots & \frac{\partial e(1)}{\partial b_{2P}} \\ \frac{\partial e(2)}{\partial w_{11}} & \frac{\partial e(2)}{\partial w_{12}} & \cdots & \frac{\partial e(2)}{\partial b_{2P}} \\ \vdots & \vdots & \cdots & \vdots \\ \frac{\partial e(N)}{\partial w_{11}} & \frac{\partial e(N)}{\partial w_{12}} & \cdots & \frac{\partial e(N)}{\partial b_{2P}} \end{bmatrix} \tag{6.16}$$

In conventional DPD models, inverse of $\mathbf{X}^H\mathbf{X}$ is calculated, whereas in NN model inverse of $\mathbf{J}^T\mathbf{J} + \mu\mathbf{I}$ is calculated. Thus the complexity of model extraction depends directly on the size of matrix $\mathbf{X}$ and $\mathbf{J}$ i.e. number of coefficients/number of weights and biases.

Table 6.1 shows the comparison between the number of weights and biases/number of coefficients of different DPD models. The Number of weights in a neural network is $2P(M+1)q + rq + 2Pr$, where P is the number of MIMO's transmitter branches. The number of biases in a neural network is $q + r + 2P$. The total number of weights and biases in a NN are $2P(M+1)q + rq + 2Pr + q + r + 2P$. The number of coefficients required by COMP

Table 6.1: Complexity comparison between different DPD Models in MIMO Transmitters

	Total No. of Coefficients/Number of Weights and Biases	
Models	**2×2 MIMO**	**3×3 MIMO**
COMPM DPD	$4(M+1)K$	$9(M+1)K$
PH DPD	$4(M+1)K(K+1)/2$	$9(M+1)K(K+1)(K+2)/6$
ACC-PH DPD	$4(M+1)K(K+1)+2$	$3(M+1)K(K+1)(K+2)+3$
NN DPD	$4(M+1)q+rq+4r+q+r+4$	$6(M+1)q+rq+6r+q+r+6$

model for a single transmitter branch in $P \times P$ MIMO is $P(M+1)K$. Thus, the total number of coefficients required by COMP model in $P \times P$ MIMO is $P^2(M+1)K$. The number of coefficients required by PH model for a single transmitter branch in 2×2 MIMO is $2(M+1)K(K+1)/2$. Thus, the total number of coefficients required by PH model in 2×2 MIMO is $4(M+1)K(K+1)/2$. Similarly, the number of coefficients required by PH model for a single transmitter branch in 3×3 MIMO is $3(M+1)K(K+1)(K+2)/6$. Thus, the total number of coefficients required by PH model in 3×3 MIMO is $9(M+1)K(K+1)(K+2)/6$. ACC-PH model requires nearly twice the number of coefficients as compared to PH model The total number of coefficients required by ACC-PH model in 2×2 MIMO and 3×3 MIMO are $4(M+1)K(K+1)+2$ and $3(M+1)K(K+1)(K+2)+3$ respectively.

6.3.4 Measurement Setup

Figure 6.3 shows the measurement setup for MIMO transmitter. The measurement setup consists of NI transmitter (PXIe-1075), couplers, different 101 LTE signals, ZHL-42 RF PAs, attenuators and FSW spectrum analyzer as a transmitter observation receiver. Three different 30 MHz 101 LTE signals are used and each consisted of 122880 samples at a sampling rate of 122.88 Msps. Three different 15 MHz 101 LTE signals are used and each set consisted of 184320 samples at a sampling rate of 92.16 Msps. NI transmitter (PXIe-1075) consists of two or three RF channel outputs (NI-5793). For 2×2 MIMO, the two different RF signals are generated by NI-5793s at a carrier frequency of 2.14 GHz. Similarly, for 3×3 MIMO, the three different RF signals are generated by NI-5793s at a carrier frequency of 2.14 GHz. These RF signals are passed through couplers of -15 dB coupling factor. After that these RF signals are used to drive ZHL-42 RF PAs. ZHL-42 PA has operating frequency range from

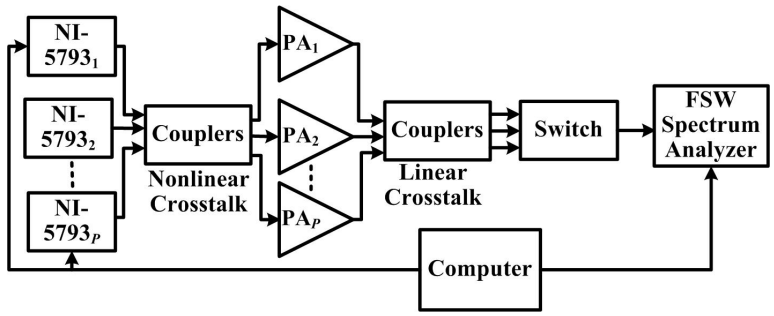

(a)

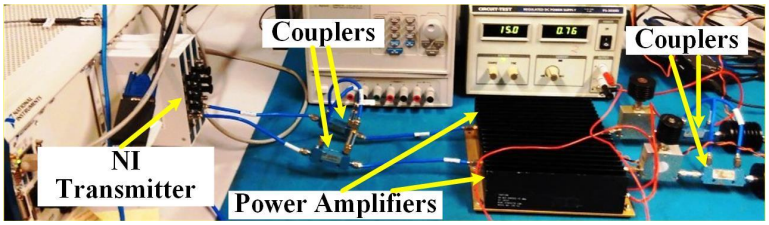

(b)

Figure 6.3: (a) Block Diagram and (b) Photograph of Measurement and Control Setup used for MIMO Transmitter.

700 to 4200 MHz and 29.28 dBm output power at 1 dB gain compression. The outputs of these PAs are passed through couplers of -15 dB coupling factor. The outputs of couplers are then passed through attenuators and then through a switch to be captured by FSW spectrum analyzer of Rohde & Schwarz.

6.3.5 Measurement Results

The DPD is performed for 2×2 and 3×3 MIMO transmitters. The training of NN is performed offline. To showcase the usefulness of utilizing the NN, two scenarios are considered in each MIMO transmitters.

6.3.5.1 Scenario I: PA and MIMO Crosstalk without Modulator Imperfection

In the first scenario, the linear crosstalk of -15 dB coupling factor and nonlinear crosstalk of -15 dB coupling factor are present in MIMO transmitters. Table 6.2 shows the inverse modeling results for scenario I, when 40000 samples of 15 MHz 101 LTE signal is used for training of NN and NN model is validated for different length of samples of 15 MHz 101 LTE signal using different random generator seeds. As from Table 6.2, varying the samples from 40000 to 184320 does not affect the inverse modeling performance much. Therefore

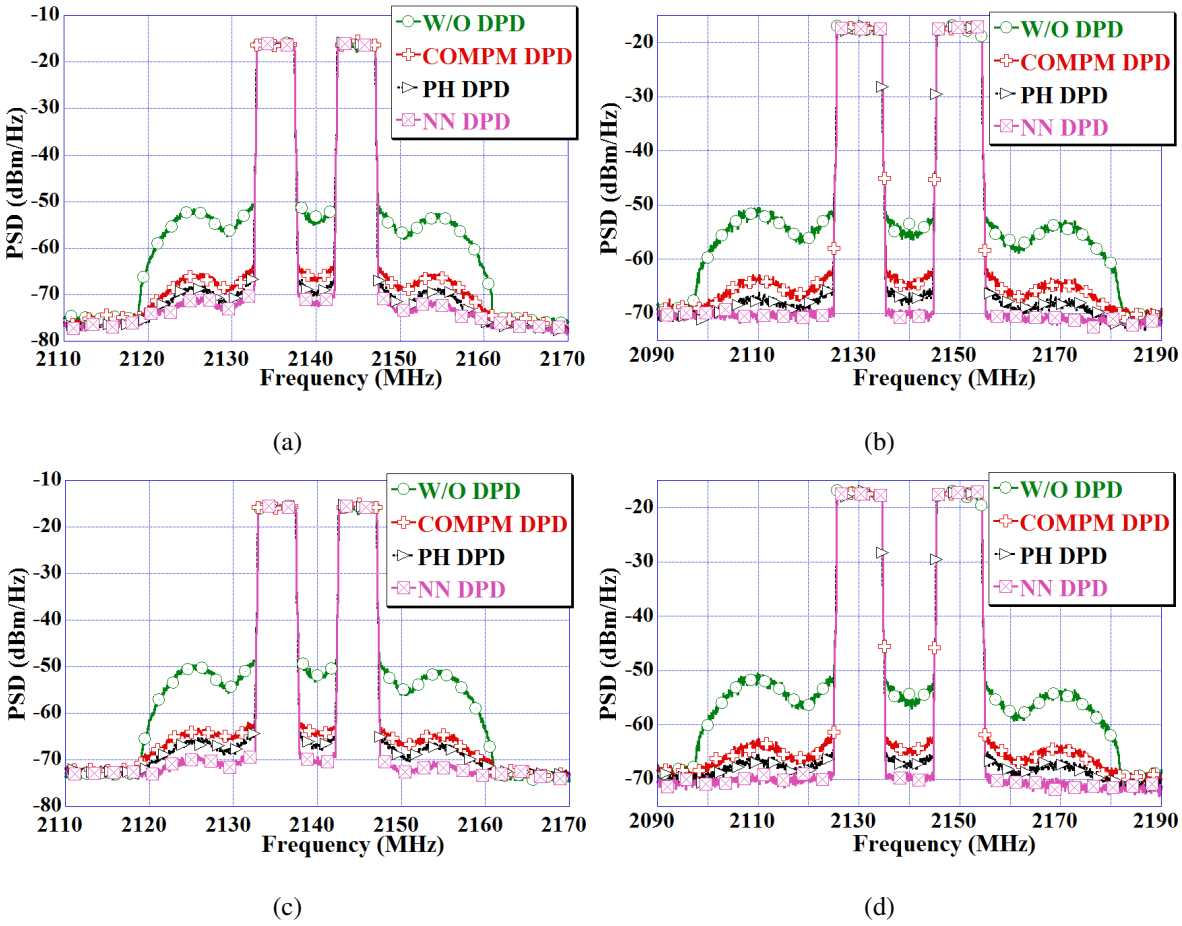

Figure 6.4: Frequency Power Spectra of various DPD models in the presence of linear crosstalk and nonlinear crosstalk for (a) 15 MHz LTE signal in 2×2, (b) 30 MHz LTE signal in 2×2, (c) 15 MHz LTE signal in 3×3, and (d) 30 MHz LTE signal in 3×3 MIMO Transmitters.

for performing DPD, 40000 samples of 15 MHz 101 LTE signal is used for training of NN i.e. model identification. After that NN model is validated for 184320 samples of 15 MHz 101 LTE signal. For 30 MHz 101 LTE signal, 40000 samples of 30 MHz 101 LTE signal is used for training of NN. After that NN model is validated for 122880 samples of 30 MHz LTE signal. Figure 6.4(a) and 6.4(b) shows the frequency power spectra of various DPD models for the scenario I in 2×2 MIMO transmitters of 15 MHz and 30 MHz LTE signals respectively. Figure 6.4(c) and 6.4(d) shows the frequency power spectra of various DPD models for the scenario I in 3×3 MIMO transmitters of 15 MHz and 30 MHz LTE signals respectively. As it can be seen from the Figure 6.4, the proposed NN-based DPD model have better ACPR.

Table 6.3 and Table 6.4 show the performance of various DPD models in presence of

Table 6.2: Inverse Modeling performances in presence of PA Nonlinearity and Crosstalk in 2×2 MIMO Transmitters for LTE 101 (15 MHz)

No. of Samples for validation	**NMSE (dB)**	**ACEPR (dBc)**
40000	-40.75	-56.78/-57.13
80000	-40.30	-56.45/-56.81
120000	-39.81	-55.99/-56.41
160000	-39.78	-55.95/-56.36
184320	-39.76	-55.92/-56.34

Table 6.3: DPD performances in presence of PA Nonlinearity and Crosstalk in 2×2 MIMO Transmitters

Signal	**LTE 101 (15 MHz)**			**LTE 101 (30 MHz)**		
Models	**NMSE (dB)**	**ACPR (dBc)**	**No. of Coeff./ Weights & Biases**	**NMSE (dB)**	**ACPR (dBc)**	**No. of Coeff./ Weights & Biases**
Without DPD	-10.88	-35.87/-37.20	N/A	-9.57	-33.64/-36.18	N/A
COMPM DPD	-35.96	-49.64/-50.06	120	-34.68	-46.76/-47.15	120
PH DPD	-37.83	-52.86/-53.47	420	-36.59	-49.80/-50.09	420
NN DPD	-39.62	-55.72/-56.19	431	-38.83	-52.76/-53.39	431

linear and nonlinear crosstalk for 2×2 and 3×3 MIMO. The COMP and PH DPD models are performed for M=4 and K=6. The number of neurons in two hidden layers of NN-based DPD model are q=14 and r=7 respectively. NN converges to its best performance in 10 iterations. From the table, it is clear that the proposed NN-based DPD model have better NMSE.

The proposed NN-based DPD model not only outperforms other DPD models in presence of crosstalk but also requires less number of coefficients (weights and biases) for large size MIMO transmitters as illustrated by the results obtained and shown in Table 6.4 for 3×3 MIMO transmitters.

Figure 6.5 shows the crosstalk in an antenna array. The antennas which are nearer would

Table 6.4: DPD performances in presence of PA Nonlinearity and Crosstalk in 3×3 MIMO Transmitters

Signal	**LTE 101 (15 MHz)**			**LTE 101 (30 MHz)**		
Models	**NMSE (dB)**	**ACPR (dBc)**	**No. of Coeff./ Weights & Biases**	**NMSE (dB)**	**ACPR (dBc)**	**No. of Coeff./ Weights & Biases**
Without DPD	-8.58	-34.38/-35.76	N/A	-9.27	-34.22/-36.52	N/A
COMPM DPD	-34.45	-48.21/-49.82	270	-32.46	-46.70/-46.79	270
PH DPD	-36.19	-50.32/-51.72	2520	-35.47	-49.27/-49.74	2520
NN DPD	-38.71	-54.95/-55.90	587	-37.96	-52.29/-52.85	587

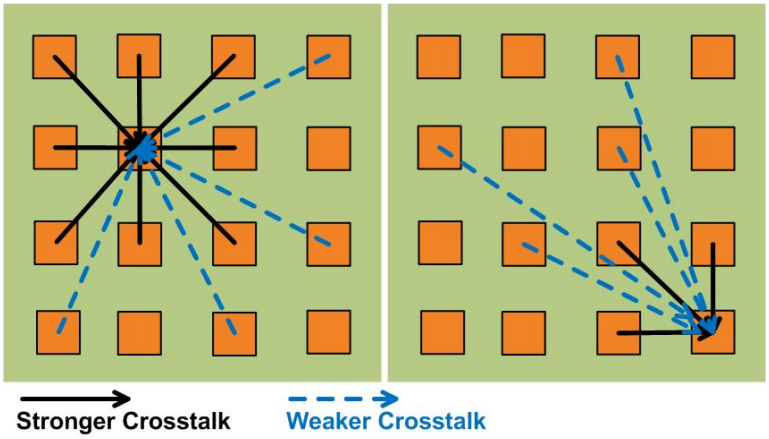

Figure 6.5: Antenna Array showing crosstalk.

impose stronger crosstalk as compared to antennas which are farther [126–128]. We have earlier chosen stronger crosstalk of equal coupling factor of -15 dB because if NN works for that, then it should work in other cases like unequal coupling factor.

To showcase that NN DPD model would also work for unequal crosstalk, Table 6.5 shows the performance of various DPD models in presence of PA nonlinearity, unequal nonlinear crosstalk (coupling factor of -15 dB from branch 2 to branch 1 and -20 dB from branch 3 to branch 1) and unequal linear crosstalk (coupling factor of -15 dB from branch 2 to branch 1 and -20 dB from branch 3 to branch 1) in 3×3 MIMO Transmitters.

Table 6.5: DPD performances in presence of PA Nonlinearity and Unequal Crosstalk in 3×3 MIMO Transmitters

Signal	**LTE 101 (30 MHz)**		
Models	**NMSE (dB)**	**ACPR (dBc)**	**No. of Coeff./Weights & Biases**
Without DPD	-10.39	-34.68/-36.75	N/A
COMPM DPD	-33.72	-46.86/-46.95	270
PH DPD	-37.14	-49.46/-49.82	2520
NN DPD	-39.07	-52.42/-52.76	587

6.3.5.2 Scenario II: PA and MIMO Crosstalk with Modulator Imperfection

In the second scenario, the linear and equal crosstalk of -15 dB coupling factor, nonlinear and equal crosstalk of -15 dB coupling factor, I/Q imbalance of -20 dB IRR, phase imbalance θ_p= 4° and dc offset of -20 dB with respect to the main signal are present in MIMO transmitters.

Figure 6.6 shows the effect of the increase of number of MIMO transmitter's branches on the inverse modeling performance and complexity as compared to other DPD models in scenario II for M=4, K=6, q=14 and r=7. With the increase in order of MIMO, the number of coefficients required by PH and ACC-PH models increases exponentially. Whereas with the increase of MIMO order, the NN model requires less number of weights and biases as compared to number of coefficients required by PH and ACC-PH models. The inverse modeling performance in terms of NMSE (dB) of NN model is better than other models.

The DPD is done for both 2×2 and 3×3 MIMO transmitters with 10 MHz and 30 MHz LTE signals. The 10 MHz LTE signal is shown for heterodyne case by using the IF-shift of 7 MHz to show the effects of I/Q imbalance in the frequency domain. For 10 MHz (IF shifted) LTE signal, 40000 samples of 10 MHz LTE signal is used for training of NN. After that NN model is validated for 184320 samples of 10 MHz (IF shifted) LTE signal. Table 6.6 and Table 6.7 show the performance of various DPD models. As seen from the tables, the performance of COMPM and PH model degrades due to the presence of I/Q imbalance and dc offset. Again, the proposed NN-based DPD model outperforms other DPD models and also requires less number of coefficients (weights and biases) as shown in Table 6.7 for 3×3 MIMO transmitters. Also, it performs inverse modeling of different transmitter's branches in one step.

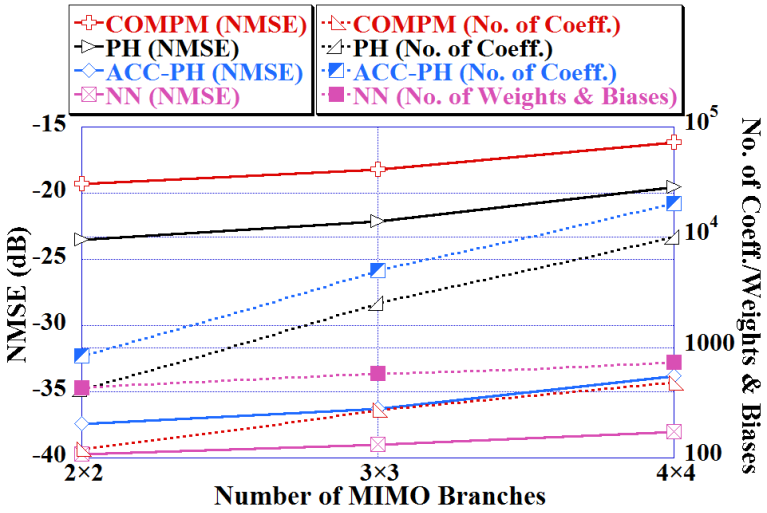

Figure 6.6: Effect of increase of number of MIMO transmitter's branches on the inverse modeling performance and number of coefficients/weights and biases in scenario II.

Table 6.6: DPD performances in presence of PA Nonlinearity, Crosstalk, I/Q Imbalance and dc offset in 2×2 MIMO Transmitters

Signal	**LTE 1 (10 MHz-IF shifted)**			**LTE 101 (30 MHz)**		
Models	**NMSE (dB)**	**ACPR (dBc)**	**No. of Coeff./ Weights & Biases**	**NMSE (dB)**	**ACPR (dBc)**	**No. of Coeff./ Weights & Biases**
Without DPD	-13.81	-36.58	N/A	-10.14	-34.44/-34.62	N/A
COMPM DPD	-21.88	-46.12	120	-18.36	-43.53/-44.07	120
PH DPD	-25.67	-48.08	420	-22.56	-47.17/-47.53	420
ACC-PH DPD	-36.37	-50.68	842	-36.47	-50.29/-51.41	842
NN DPD	-39.48	-54.04	431	-38.81	-53.04/-53.50	431

Figure 6.7(a) and Figure 6.7(c) show the frequency power spectra of various outputs of DPD models for scenario II in 2×2 MIMO transmitters and 3×3 MIMO transmitters for 10 MHz LTE signal IF-shifted by 7 MHz. There is an image present in the output of without DPD signal having IRR of -20 dB due to I/Q imbalance. COMPM DPD and PH DPD outputs also have images and thus they are unable to mitigate the effects of I/Q imbalance. Table 6.8 shows the IRR (dB) values of DPD outputs for scenario II in 2×2 MIMO transmitters and 3×3 MIMO transmitters for 10 MHz LTE signal IF-shifted by 7 MHz. The

Table 6.7: DPD performances in presence of PA Nonlinearity, Crosstalk, I/Q Imbalance and dc offset in 3×3 MIMO Transmitters

Signal	**LTE 1 (10 MHz-IF shifted)**			**LTE 101 (30 MHz)**		
Models	**NMSE (dB)**	**ACPR (dBc)**	**No. of Coeff./ Weights & Biases**	**NMSE (dB)**	**ACPR (dBc)**	**No. of Coeff./ Weights & Biases**
Without DPD	-12.54	-36.20	N/A	-9.57	-34.17/-34.84	N/A
COMPM DPD	-20.63	-45.43	270	-17.28	-42.21/-42.56	270
PH DPD	-23.65	-46.15	2520	-21.19	-45.38/-45.56	2520
ACC-PH DPD	-34.32	-50.44	5043	-35.33	-48.86/-49.88	5043
NN DPD	-38.96	-53.85	587	-38.09	-51.62/-52.44	587

NN-based DPD model output has least IRR. Figure 6.7(b) and Figure 6.7(d) show the frequency power spectra of various outputs of DPD models and its error (e.g. COMPM error= $y_{meas-COMPM}(n) - x(n)$) for scenario II in 2×2 MIMO transmitters and 3×3 MIMO transmitters for 30 MHz LTE signal. COMPM and PH errors plots show in-band errors which are due to the presence of I/Q imbalance. Actually, there is an image due to I/Q imbalance, which is hiding under signal, appears as an error during transmission in Figure 6.7(b) and 6.7(d) for IF shift=0 case. From the graph, it is clear that the proposed NN DPD model has better ACPR and IRR performance as compared to other DPD model and requires the less number of coefficients (weights and biases) in 3×3 MIMO transmitters.

Earlier results show the DPD performance of different LTE signals for two scenarios of only one output of 2×2 MIMO and 3×3 MIMO transmitters. Table 6.9 shows the proposed NN DPD performances for both scenarios for all the branches in 3×3 MIMO transmitters for 30 MHz LTE 101 signals. NN performs DPD of different branches in one step with good linearization results.

6.3.5.3 Batch-Mode NN DPD Resource Consumption Estimation

NN is an iterative method; therefore, its main advantage is in terms of DPD application and adaptation. Figure 6.8 shows the proposed intermittent updating process, where NN training is performed offline (SD card) and the weights are updated in predistorter (FPGA or digital

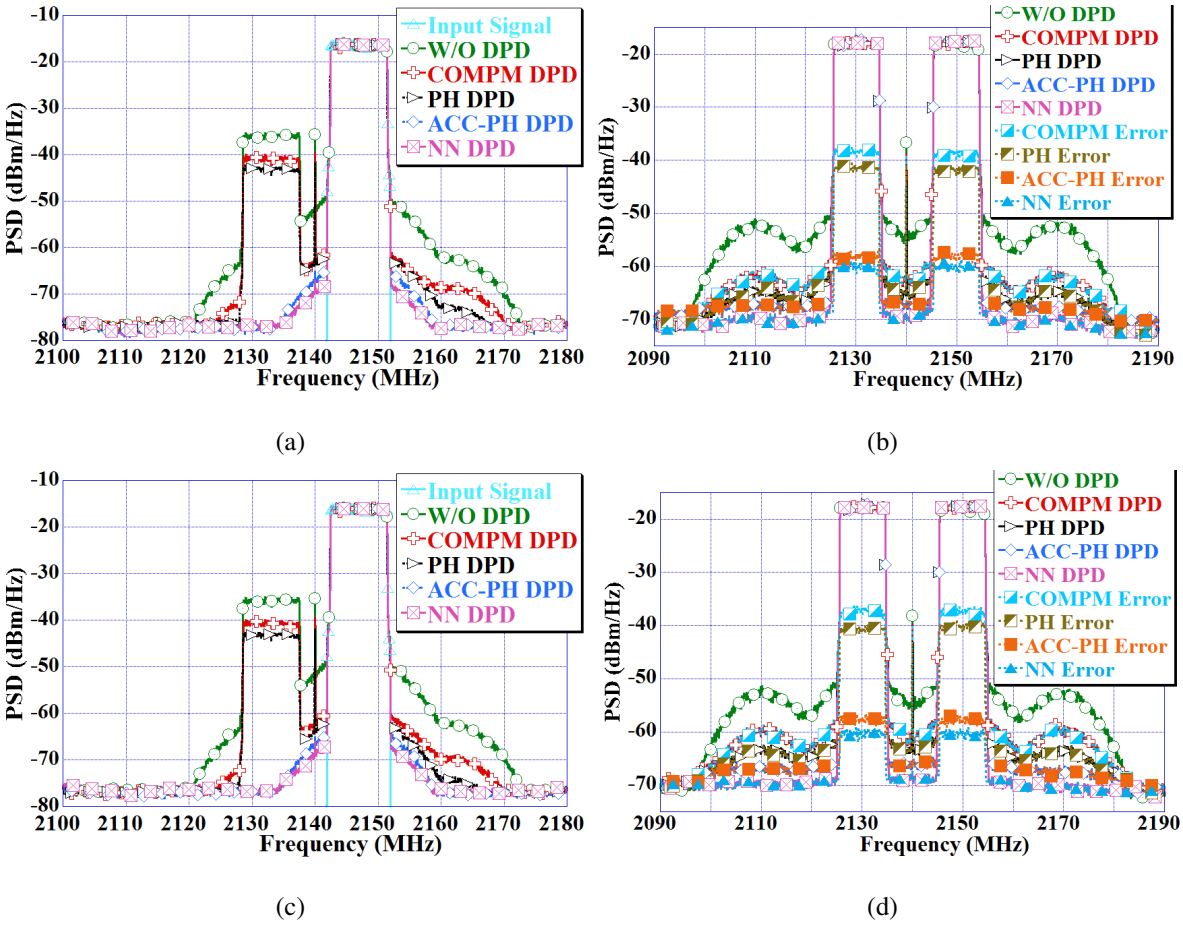

Figure 6.7: Frequency Power Spectra of various DPD models in the presence of crosstalk, *I*/*Q* imbalance and dc offset for (a) 10 MHz in 2×2, (b) 30 MHz in 2×2, (c) 10 MHz in 3×3 and (d) 30 MHz in 3×3 MIMO Transmitters.

Table 6.8: DPD performances in terms of IRR for Scenario II in 2×2 and 3×3 MIMO Transmitters for 10 MHz LTE Signal IF-Shifted

Transmitter	**2×2**	**3×3**
Models	**IRR (dB)**	**IRR (dB)**
Without DPD	-20 dB	-20 dB
COMPM DPD	-24.88	-24.86
PH DPD	-27.11	-27.33
ACC-PH DPD	-55.72	-55.32
NN DPD	-57.10	-56.60

signal processor) after a fixed interval of time.

It is to be noted that the DPD application is a continuous process, as all data passes

Table 6.9: DPD performances for both Scenarios for all the branches in 3×3 MIMO Transmitters for 30 MHz LTE 101 Signals

Performance	Scenario I			Scenario II		
	Branch 1	Branch 2	Branch 3	Branch 1	Branch 2	Branch 3
NMSE (dB)	-37.96	-37.91	-37.67	-38.09	-38.48	-38.03
ACPR (dBc)	-52.29/ -52.85	-52.37/ -52.54	-52.08/ -52.63	-51.62/ -52.44	-51.12/ -51.03	-51.47/ -51.21

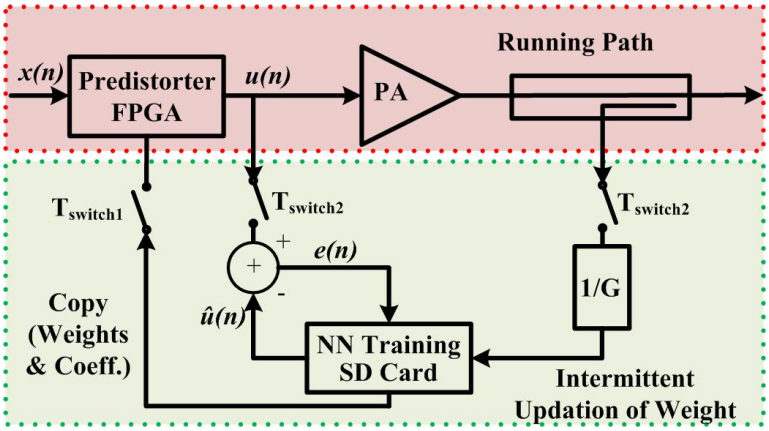

Figure 6.8: Proposed intermittent updating process for NN DPD.

through DPD application block. While, DPD training is done intermittently for a predefined length of training data after a fixed time interval, or whenever ACPR drops below a given interval, therefore processing complexity of DPD application is more prominent which is dependent on number of coefficients.

For training, it is anticipated that after the first application of trained NN, the training converge of the NN network to an acceptable solution will be faster and the model tends to be more appropriate for batch mode based adaptive DPD where the training of the network for each iteration will be based on the previous iteration network parameter's value.

Furthermore, it is anticipated that for $P \times P$ MIMO system, the rate of increase of complexity of NN DPD in terms of number of model coefficients is less than the PH, ACC-PH and COMPM models. Indeed, the increase of numbers of coefficients in PH and ACC-PH is proportional to $P^2 \times K^P$, whereas in COMPM it is proportional to P^2, however, in contrast, the neural network might require the addition of few supplementary neurons to reach to an acceptable modeling performance and it is proportional to $2P$.

6.4 Proposed Polynomial based DPD Model

Usually, the crosstalk from another branch to the main branch is less as compared to the strength of the original signal of the main branch i.e. $|x_1(n)| > |\alpha_{21}x_2(n)|$, $|x_1(n)| > |\alpha_{31}x_3(n)|$, $|x_1(n)| > |\alpha_{41}x_4(n)|$, $|v_1(n)| > |\beta_{21}v_2(n)|$, $|v_1(n)| > |\beta_{31}v_3(n)|$ and $|v_1(n)| > |\beta_{41}v_4(n)|$. These coupling factors are defined in section 6.2.1 and Figure 6.1. The coupling factor varies from -15 dB to -30 dB for typical levels of crosstalk [57]. As a result, PA driven by $|\alpha_{21}x_2(n)|$ provides less nonlinearity in comparison to $|x_1(n)|$ driven PA in first transmitter path.

The output PA signal of first transmitter path in case of nonlinear crosstalk can be mathematically expressed as

$$\begin{aligned} v_1(n) = &\sum_{m=0}^{M}\sum_{k=0}^{K-1}\sum_{j=0}^{k}\sum_{i=0}^{j}\sum_{h=0}^{i} x_1(n-m)\,l(n-m) \\ &+ \sum_{m=0}^{M}\sum_{k=0}^{K-1}\sum_{j=0}^{k}\sum_{i=0}^{j}\sum_{h=0}^{i} x_2(n-m)\,l(n-m) \\ &+ \sum_{m=0}^{M}\sum_{k=0}^{K-1}\sum_{j=0}^{k}\sum_{i=0}^{j}\sum_{h=0}^{i} x_3(n-m)\,l(n-m) \\ &+ \sum_{m=0}^{M}\sum_{k=0}^{K-1}\sum_{j=0}^{k}\sum_{i=0}^{j}\sum_{h=0}^{i} x_4(n-m)\,l(n-m) \end{aligned} \tag{6.17}$$

where

$$\begin{aligned} l(n) &= l\left(|x_1(n)|, |x_2(n)|, |x_3(n)|, |x_4(n)|\right) \\ &= \left(|x_1(n)|^{k-j}|\alpha_{21}x_2(n)|^{j-i}|\alpha_{31}x_3(n)|^{i-h}|\alpha_{41}x_4(n)|^{h}\right) \end{aligned} \tag{6.18}$$

For a MIMO transmitter having coupling factor of -10 dB between branches i.e $\alpha_{21} = \alpha_{31} = \alpha_{41} = (10)^{-10/20} = 1/(10)^{1/2}$, one can write that

$$l(n) = \left(|x_1(n)|^{k-j}\left|\frac{x_2(n)}{(10^{1/2})}\right|^{j-i}\left|\frac{x_3(n)}{(10^{1/2})}\right|^{i-h}\left|\frac{x_4(n)}{(10^{1/2})}\right|^{h}\right) \tag{6.19}$$

The typical high nonlinearity order K of PAs would make these terms $\left|x_2/\left(10^{1/2}\right)\right|^{j-i}\left|x_3/\left(10^{1/2}\right)\right|^{i-h}\left|x_4/\left(10^{1/2}\right)\right|^{h}$ tend to be negligible and the contribution of $l(n)$ function to the overall output of the system will decay with the order of the nonlinearity K. Therefore this would result in a model with a reduced nonlinearity order when compared to the nonlinearity order of the model where the system is driven only with actual carrier signal without leaking crosstalk signals.

The expansion and simplification of first term of equation (6.17) is shown in Appendix B. Correspondingly, rearranging rest three terms of equation (6.17) using the equation (B.2),

the output of a transmitter path in case of nonlinear crosstalk can be mathematically modeled as

$$\begin{aligned}
y_1(n) &= \sum_{m=0}^{M}\sum_{k=0}^{K-1} c^{(1)}_{m,k,1}\cdot x_1(n-m)\cdot|x_1(n-m)|^k \\
&+\sum_{m=0}^{M}\sum_{k=1}^{K/2}\sum_{j=1}^{k}\sum_{i=1}^{j}\sum_{h=1}^{i} c^{(1)}_{m,k,j,i,h,1}\cdot x_1(n-m)\,|x_1(n-m)|^{k-j}|x_2(n-m)|^{j-i}|x_3(n-m)|^{i-h}|x_4(n-m)|^{h} \\
&+\sum_{m=0}^{M}\sum_{k=1}^{K/2}\sum_{j=1}^{k}\sum_{i=1}^{j}\sum_{h=1}^{i} c^{(1)}_{m,k,j,i,h,2}\cdot x_2(n-m)\,|x_1(n-m)|^{k-j}|x_2(n-m)|^{j-i}|x_3(n-m)|^{i-h}|x_4(n-m)|^{h} \\
&+\sum_{m=0}^{M}\sum_{k=1}^{K/2}\sum_{j=1}^{k}\sum_{i=1}^{j}\sum_{h=1}^{i} c^{(1)}_{m,k,j,i,h,3}\cdot x_3(n-m)\,|x_1(n-m)|^{k-j}|x_2(n-m)|^{j-i}|x_3(n-m)|^{i-h}|x_4(n-m)|^{h} \\
&+\sum_{m=0}^{M}\sum_{k=1}^{K/2}\sum_{j=1}^{k}\sum_{i=1}^{j}\sum_{h=1}^{i} c^{(1)}_{m,k,j,i,h,4}\cdot x_4(n-m)\,|x_1(n-m)|^{k-j}|x_2(n-m)|^{j-i}|x_3(n-m)|^{i-h}|x_4(n-m)|^{h}
\end{aligned} \tag{6.20}$$

where $c^{(1)}_{m,k,j,i,h,1}$ are the coefficients and

$$\begin{aligned}
f(n-m) &= f\left(|x_1(n-m)|,|x_2(n-m)|,|x_3(n-m)|,|x_4(n-m)|\right) \\
&= |x_1(n-m)|^{k-j}|x_2(n-m)|^{j-i}|x_3(n-m)|^{i-h}|x_4(n-m)|^{h}
\end{aligned} \tag{6.21}$$

In case of linear crosstalk, the PA output would be a linear transfer function of cross-over single-input nonlinear memory polynomial functions. Again its nonlinearity order is much lesser than the nonlinearity due to the actual carrier input signal. Thus the output of the proposed model including both linear and nonlinear crosstalk can be expressed as

$$\begin{aligned}
y_1(n) &= \sum_{m=0}^{M}\sum_{k=0}^{K-1} c^{(1)}_{m,k,1}\cdot x_1(n-m)\cdot|x_1(n-m)|^k \\
&+\sum_{m=0}^{M}\sum_{k=1}^{K/2}\sum_{j=1}^{k}\sum_{i=1}^{j}\sum_{h=1}^{i} c^{(1)}_{m,k,j,i,h,1}\cdot x_1(n-m)\cdot f(n-m) \\
&+\sum_{m=0}^{M}\sum_{k=1}^{K/2}\sum_{j=1}^{k}\sum_{i=1}^{j}\sum_{h=1}^{i} c^{(1)}_{m,k,j,i,h,2}\cdot x_2(n-m)\cdot f(n-m) \\
&+\sum_{m=0}^{M}\sum_{k=1}^{K/2}\sum_{j=1}^{k}\sum_{i=1}^{j}\sum_{h=1}^{i} c^{(1)}_{m,k,j,i,h,3}\cdot x_3(n-m)\cdot f(n-m) \\
&+\sum_{m=0}^{M}\sum_{k=1}^{K/2}\sum_{j=1}^{k}\sum_{i=1}^{j}\sum_{h=1}^{i} c^{(1)}_{m,k,j,i,h,4}\cdot x_4(n-m)\cdot f(n-m) \\
&+\sum_{m=0}^{M}\sum_{k=0}^{K/2-1} c^{(1)}_{m,k,2}\cdot x_2(n-m)\cdot|x_2(n-m)|^k \\
&+\sum_{m=0}^{M}\sum_{k=0}^{K/2-1} c^{(1)}_{m,k,3}\cdot x_3(n-m)\cdot|x_3(n-m)|^k \\
&+\sum_{m=0}^{M}\sum_{k=0}^{K/2-1} c^{(1)}_{m,k,4}\cdot x_4(n-m)\cdot|x_4(n-m)|^k
\end{aligned} \tag{6.22}$$

Indirect learning approach is used to perform the DPD [22]. In this approach, while performing inverse modeling of PA, the complex baseband normalized input signal and normalized output signal are replaced with each other.

The matrix form of equation (6.22) is represented as

$$\mathbf{y} = \mathbf{V}\mathbf{c} \tag{6.23}$$

where $\mathbf{c}$ is a vector of coefficients to be extracted, $\mathbf{V}$ is the observation (predistorter) matrix containing the terms of DPD input/PA feedback output and $\mathbf{y}$ is a vector of output of model. Then using the Least-Squares (LS) solution, $\hat{\mathbf{c}}$ is extracted as

$$\hat{\mathbf{c}} = \left(\mathbf{V}^H\mathbf{V}\right)^{-1}\mathbf{V}^H\mathbf{y} = \mathbf{V}^+\mathbf{y} \tag{6.24}$$

where $\mathbf{V}^H$ denotes hermitian transpose of $\mathbf{V}$ and $\mathbf{V}^+$ is called the pseudo-inverse.

6.4.1 Complexity comparison between DPD models

The running complexity of a DPD model is the number of mathematical operations done for each sample. In digital signal processor, it is measured in terms of floating point operations (FLOPs). The complex-complex addition and complex-complex multiplication operation require 2 and 6 flops respectively [30]. Table 6.10 shows the comparison between the numbers of coefficients and flops of the different DPD models. The number of coefficients required by COMP model from equation (6.5) for a single transmitter branch in 4×4 MIMO is $4(M+1)K$. It requires $4(M+1)K$ complex-complex multiplication operations and $4(M+1)K$-1 complex-complex addition operations. The total number of flops required by COMP model for a single transmitter branch in 4×4 MIMO is $8 \times 4(M+1)K$-2. Thus, the total number of coefficients and flops required by COMP model in 4×4 MIMO are $16(M+1)K$ and $128(M+1)K$-8 respectively.

The number of coefficients required by PH model from equation (6.6) for a single transmitter branch in 4×4 MIMO is $4(M+1)K(K+1)(K+2)(K+3)$/24. The total number of flops required by PH model for a single transmitter branch in 4×4 MIMO is $8 \times 4(M+1)K(K+1)(K+2)(K+3)$/24-2. Thus, the total number of coefficients and flops required by PH model in 4×4 MIMO is $2(M+1)K(K+1)(K+2)(K+3)$/3 and $16(M+1)K(K+1)(K+2)(K+3)$/3-8 respectively.

The number of coefficients required by proposed model from equation (6.22) for a single transmitter branch in 4×4 MIMO is $(M+1)K$+$3(M+1)\times g(K)$+$4(M+1)\times g(K)(g(K)+1)(g(K)+2)(g(K)+3)$/24, where $g(K)$ is a floor function and $g(K) = floor(K/2)$. The total number of flops required by proposed model for a single transmitter branch in 4×4

Table 6.10: Complexity comparison between different DPD Models in 4×4 MIMO Transmitters

Models	Total No. of Coef. in 4×4 MIMO	Total No. of Flops in 4×4 MIMO
COMPM DPD	$16(M+1)K$	$128(M+1)K$-8
PH DPD	$2(M+1)K(K+1)(K+2)(K+3)/3$	$16(M+1)K(K+1)(K+2)(K+3)/3$-8
Proposed DPD	$4(M+1)[K+3g(K)+g(K)(g(K)+1)(g(K)+2)(g(K)+3)/6]$	$32(M+1)[K+3g(K)+g(K)(g(K)+1)(g(K)+2)(g(K)+3)/6]$-8

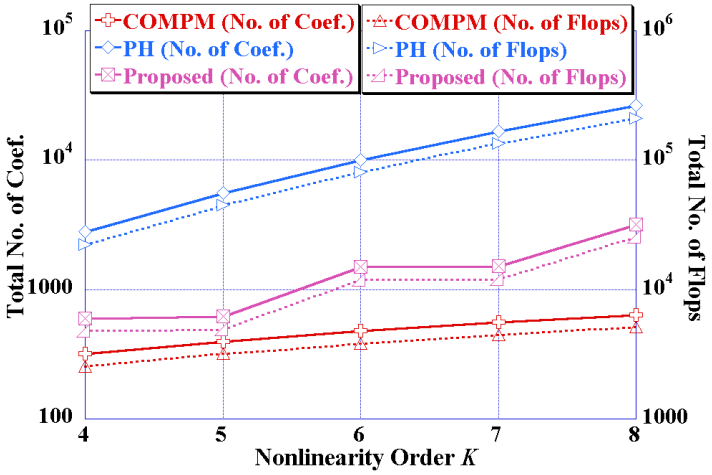

Figure 6.9: Total number of coefficients and flops of different models as a function of nonlinearity order K and fixed memory depth M=4.

MIMO is $8(M+1)[K+3g(K)+g(K)(g(K)+1)(g(K)+2)(g(K)+3)/6]$-2. Thus, the total number of coefficients and flops required by the proposed model in 4×4 MIMO is $4(M+1)[K+3g(K)+g(K)(g(K)+1)(g(K)+2)(g(K)+3)/6]$ and $32(M+1)[K+3g(K)+g(K)(g(K)+1)(g(K)+2)(g(K)+3)/6]$-8 respectively.

ACO-MP Model has been derived only for 2×2 MIMO transmitters [57] and there is no straightforward mathematical derivation of this model for higher dimension of MIMO transmitters; for this reason it is not included in Table 6.10 as well as in the comparison of the performance of the different models in section 6.4.3.

Figure 6.9 shows the total number of coefficients and number of flops of different DPD models for a fixed memory depth M=4 and nonlinearity order K from 4 to 8. As from the figure, the proposed DPD model has less number of coefficients and flops than PH model.

6.4.2 Measurement Setup

Figure 6.10 shows the measurement setup for MIMO transmitter. The measurement setup consists of a Tektronix transmitter (AWG5200), couplers, different LTE signals, RF PAs, at-

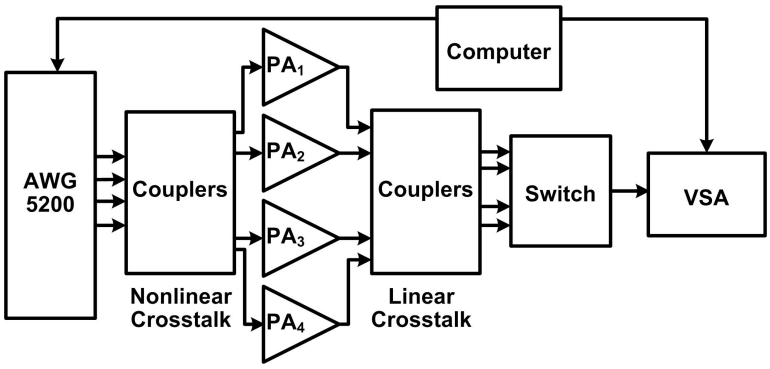

(a)

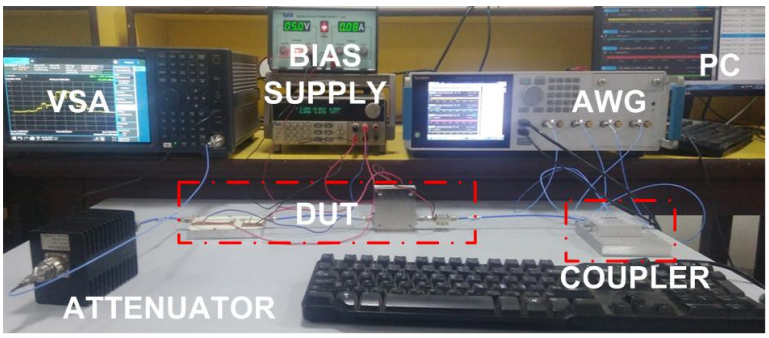

(b)

Figure 6.10: (a) Block Diagram and (b) Photograph of Measurement Setup used for MIMO Transmitter.

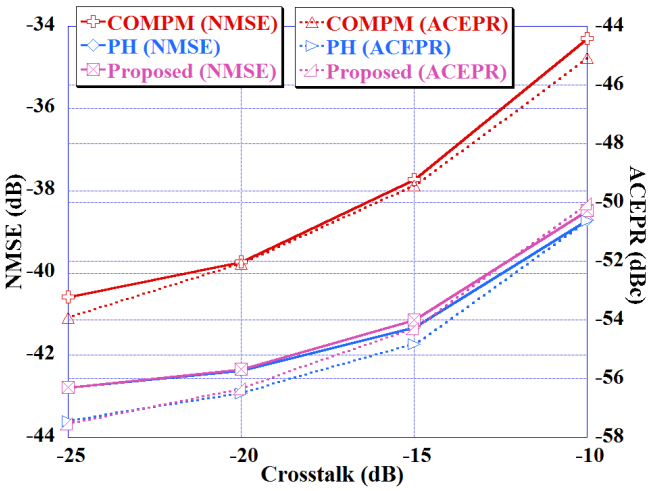

Figure 6.11: Effect of the nonlinear crosstalk on the behavioral modeling of the different models in 4×4 MIMO.

tenuators and VSA (MXA N9020B) as a transmitter observation receiver. AWG5200 transmitter has four RF output channels which samples signals at 200 Msps. Four different LTE signals of 40 MHz bandwidth are transmitted at a carrier frequency of 4 GHz from AWG and these RF signals are passed through 4×4 coupling network. The outputs of these couplers

Table 6.11: Behavioral modeling results for different models in 4×4 MIMO Transmitters of LTE 40 MHz Signal

	Case I			Case II		
Models	**NMSE (dB)**	**ACEPR (dBc)**	**Total No. of Coef./Flops**	**NMSE (dB)**	**ACEPR (dBc)**	**Total No. of Coef./Flops**
COMPM	-37.72	-49.92	480/3832	-36.26	-47.04	480/3832
PH	-41.32	-54.82	10080/80632	-39.45	-52.51	10080/80632
Proposed	-41.15	-54.30	1500/11992	-39.36	-52.20	1500/11992

Table 6.12: Behavioral modeling results for different models in 4×4 MIMO Transmitters of LTE 111 30 MHz Signal

	Case I			Case II		
Models	**NMSE (dB)**	**ACEPR (dBc)**	**Total No. of Coef./ Flops**	**NMSE (dB)**	**ACEPR (dBc)**	**Total No. of Coef./ Flops**
COMPM	-38.97	-48.58	480/3832	-37.24	-48.05	480/3832
PH	-42.34	-56.50	10080/80632	-41.12	-54.71	10080/80632
Proposed	-42.25	-56.54	1500/11992	-41.01	-54.68	1500/11992

are passed through the four similar PAs (model: ZX60-V63+). The ZX60-V63+ PA has 15 dBm output power at 1 dB gain compression and output frequency ranging from 0.05 to 6 GHz. The outputs of PAs are then passed through 4×4 coupling network and then through a switch to be selectively captured by the VSA. A 10 MHz reference is provided from AWG to VSA for phase synchronization. The measurements are also done for four different LTE carriers aggregated (CA) 111 signals of 30 MHz bandwidth each. 30 MHz LTE RF signals are generated by AWG at a carrier frequency of 1.9 GHz. These RF signals are passed through 4×4 coupling networks to induce the nonlinear crosstalk and then passed through four amplifiers; each is constituted by a driver PA (model: ZX60-2411BM-S+) and a 15–W class AB PA. ZX60-2411BM-S+ PA has 24 dBm output power respectively at 1 dB gain compression and output frequency ranging from 0.8 to 2.4 GHz. The 15–W Class-AB is a gallium nitride (GaN) based PA, biased at a drain voltage of 28 V and drain current of 90 mA. The outputs of PAs are then passed through 4×4 coupling network and then through

Table 6.13: DPD results for different models in 4×4 MIMO Transmitters of LTE 40 MHz Signal

	Case I			Case II		
Models	**NMSE (dB)**	**ACPR (dBc)**	**Total No. of Coef./Flops**	**NMSE (dB)**	**ACPR (dBc)**	**Total No. of Coef./Flops**
W/O DPD	-9.47	-39.31	N/A	-7.71	-37.38	N/A
COMPM DPD	-36.67	-49.51	480/3832	-34.04	-47.11	480/3832
PH DPD	-40.94	-54.56	10080/80632	-38.93	-52.29	10080/80632
Proposed DPD	-40.75	-54.13	1500/11992	-38.86	-52.04	1500/11992

a switch to be selectively captured by the VSA for signal acquisition, downconversion and demodulation purposes.

6.4.3 Measurement Results

6.4.3.1 Behavioral Modeling Results

The behavioral modeling performance is measured in terms of metrics like ACEPR and NMSE.

Figure 6.11 shows the effect of nonlinear crosstalk on the behavioral modeling of different models. The behavioral modeling is performed for nonlinearity order K=6, memory depth M=4 in 4×4 MIMO for 40 MHz LTE signal. PH and proposed models have nearly same NMSE and ACEPR performance. For stronger nonlinear crosstalk (-10 dB, -15 dB), NMSE performance of the proposed model is better than COMP model by 4 dB. For weaker nonlinear crosstalk (-25 dB), NMSE performance of the proposed model is still better than COMP model by 2 dB.

The behavioral modeling is also performed for 4×4 MIMO transmitters for two different cases and different LTE signals. In Case I, -15 dB nonlinear crosstalks are introduced in all branches of MIMO transmitters. In Case II, -15 dB nonlinear crosstalks and -15 dB

Table 6.14: DPD results for different models in 4×4 MIMO Transmitters of LTE 111 30 MHz Signal

	Case I			Case II		
Models	**NMSE (dB)**	**ACPR (dBc)**	**Total No. of Coef./Flops**	**NMSE (dB)**	**ACPR (dBc)**	**Total No. of Coef./Flops**
W/O DPD	-8.22	-39.86	N/A	-6.46	-39.22	N/A
COMPM DPD	-37.48	-48.47	480/3832	-35.92	-47.82	480/3832
PH DPD	-41.24	-56.33	10080/80632	-40.45	-54.86	10080/80632
Proposed DPD	-41.05	-56.04	1500/11992	-40.18	-54.39	1500/11992

linear crosstalks are introduced in all branches of MIMO transmitter. Table 6.11 shows the behavioral modeling performance of different models for 40 MHz LTE signal for the above two cases at K=6 and M=4. In both cases, the proposed model has nearly same NMSE and ACEPR with less number of coefficients and flops as compared to PH model. The proposed model has better NMSE and ACEPR as compared to COMP model. Table 6.12 shows the behavioral modeling performance of different models for 30 MHz LTE 111 signal for both cases at K=6 and M=4. Again, in both cases, the proposed model has nearly same NMSE and ACEPR with much less number of coefficients and flops as compared to PH model.

6.4.3.2 DPD Results

The linearization performance of the DPD model is measured in terms of metrics like ACPR and NMSE.

DPD is also performed for 4×4 MIMO transmitters for the above two cases having different LTE signals. Table 6.13 shows the DPD results of different models for 40 MHz LTE signals for the above two cases at K=6, and M=4. In both cases, the proposed model has nearly same NMSE and ACPR with less number of coefficients and flops as compared to PH model. The Proposed model has better NMSE and ACPR as compared to COMP model. Table 6.14 shows the DPD results of different models for 30 MHz LTE 111 signals for both

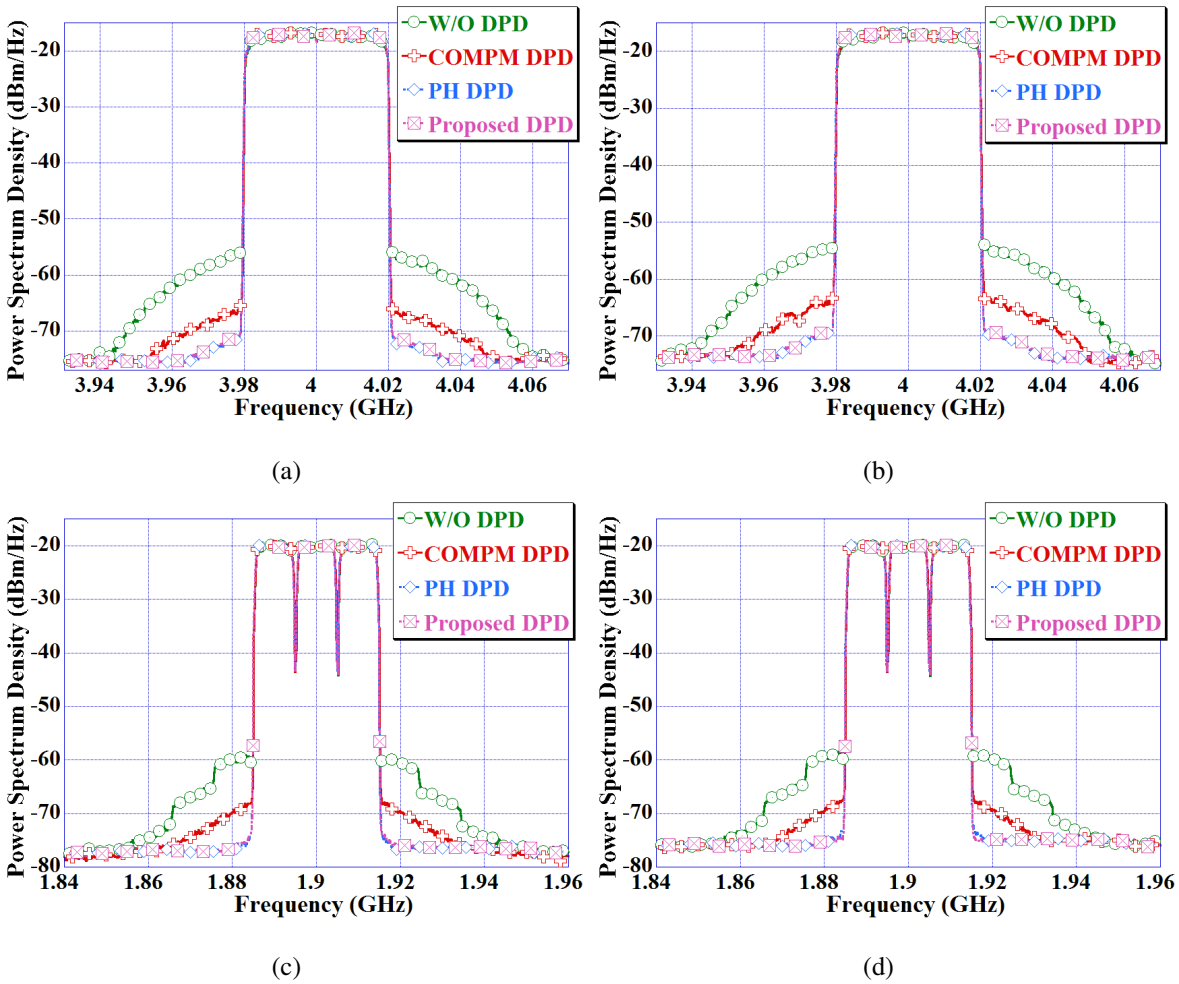

Figure 6.12: Frequency Power Spectra of various DPD model for (a) 40 MHz LTE signal for case I in 4×4 MIMO, (b) 40 MHz LTE signal for case II in 4×4 MIMO, (c) 30 MHz LTE signal for case I in 4×4 MIMO and (d) 30 MHz LTE signal for case II in 4×4 MIMO Transmitters.

cases at K=6 and M=4. Again, in both cases, the proposed model has nearly same NMSE and ACPR with less number of coefficients and flops as compared to PH model.

Figure 6.12 shows the frequency power spectra of various DPD models. It is clear from the figures that the ACPR of the proposed model is nearly same as PH model. ACPR of the proposed model is better than COMP model.

Figure 6.13 shows the constellation plot of the output of PA without DPD and proposed DPD output. This constellation plot is for 64-QAM of 40 MHz LTE signal. As from Figure 6.13, constellation plot of the output of PA without DPD is much distorted and has error vector magnitude (EVM)=7.31%. The Proposed DPD output is linearized and has EVM=1.08%.

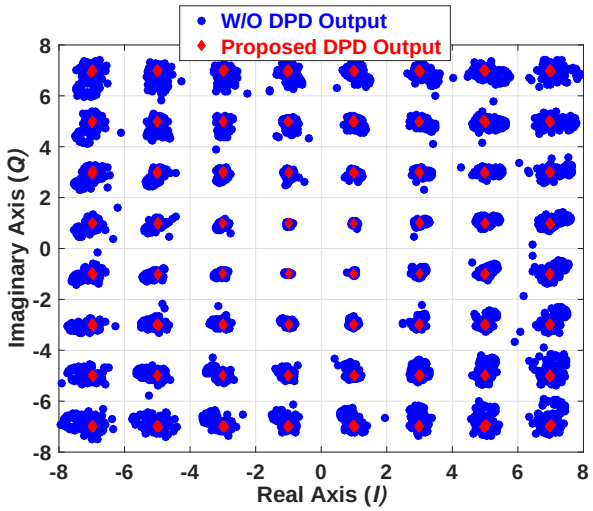

Figure 6.13: Constellation diagram of PA output without DPD and Proposed DPD output.

6.5 Conclusion

In the first part of this chapter, we present a one-step digital solution for linearization and compensation of transmitter's impairment in MIMO topology. The proposed NN-based DPD model is implemented in 2×2 and 3×3 MIMO transmitters having impairments like PA nonlinearity, crosstalk, I/Q imbalance and dc offset. The proposed NN-based DPD model shows good results as compared to other DPD models with less number of coefficients (weights and biases) as the order of MIMO transmitters increases. This proposed model could be extended for linearization and compensation of impairments present in massive MIMO for 5G wireless communication. It is to be noted that the neural network based methods are generally considered complex over its polynomial counterpart. However, in the case of MIMO, due to use of the single DPD block, this complexity is justified.

In the second part of this chapter, we present a novel, less complex DPD model for linearization of MIMO transmitters by considering that the crosstalk would be weaker in strength as compared to the actual carrier input signal in a given branch of a MIMO transmitter. The proposed DPD model is implemented in 4×4 MIMO transmitters having impairments like PA nonlinearity, nonlinear crosstalk and linear crosstalk. The results show that nonlinearity due to crosstalk can be modeled by half of the nonlinearity order as compared to the nonlinearity order of the main branch. This reduces the model complexity, number of mathematical operations and coefficient extraction burden of DPD. The proposed model could be extended for linearization and compensation of impairments present in large scale or massive MIMO for 5G wireless communications. This can be anticipated since, in partic-

ular situations, the effects of crosstalk between branches of MIMO transmitters will decay significantly beyond the second adjacent branches with respect to a given branch of massive MIMO transmitter. Therefore the proposed model can be extended to large-scale MIMO transmitters that can be considered as a cluster of 4×4 transmitters.

Chapter 7

Conclusions and Future Work

7.1 Conclusions

The focus of this thesis is to reduce model complexity and improve numerical stability of DPD model, while maintaining linearization performance of DPD for distortions due to analog imperfections such as PA nonlinearity, I/Q imbalance, cross-band inter modulation and cross-branch interference for concurrent multi-band and multi-channel transmission. The attainments of this thesis are concluded as follows:

1. The MP-PCA DPD model is proposed. The main advantages of this model are:
    - The proposed MP-PCA model has comparable performance in terms of NMSE and ACEPR in 64-bit double floating point calculation but with a reduced number of coefficients, condition number and dispersion coefficient as compared with the conventional MP model and OMP model.
    - NMSE and ACEPR performances are better in MP-PCA model as compared to MP model and OMP model for the 16-bit fixed point DSP.
2. The novel Independent Component Analysis (ICA) method for the DPD models is proposed, which is suitable for all three cases (intraband contiguous, intra-band non-contiguous and inter-band non-contiguous) of CA. The main advantages of this model are:
    - MP-ICA has least condition number and dispersion coefficient as compared with the MP, OMP and MP-PCA model in intra-band and inter-band carrier aggregation.

- The proposed ICA based DPD model is implemented in 12-bit fixed point DSP and shows good linearization results.

3. The 2D-CHMP model is proposed for linearization in concurrent dual-band transmitters operating at harmonic frequencies. The main advantages of this model are:

   - The proposed 2D-CHMP model is constructed by simplifying the envelope terms of the 2D-HMP model.
   - The total number of coefficients of the 2D-CHMP model is $(K+1)/2$ times lesser than the 2D-HMP model.
   - Also, the computational complexity of 2D-CHMP DPD is $(K+1)/6$ and $3(K+1)/14$ times lesser than 2D-HMP DPD for two and three LS iterations respectively.

4. The 3D-HMP and 3D-HVS DPD models are proposed to mitigate the in-band harmonic distortions, CMDs and IMDs generated by ultra-wideband PA when carrier signals are transmitted at harmonic frequencies in the concurrent tri-band transmitter.

5. A one-step digital solution for linearization and compensation of transmitters' impairments in MIMO topology is proposed. The main advantages of this model are:

   - The proposed NN-based DPD model is implemented in 2×2 and 3×3 MIMO transmitters having impairments like PA nonlinearity, crosstalk, I/Q imbalance and dc offset.
   - The proposed NN-based DPD model shows good results as compared to other DPD models with less number of coefficients (weights and biases) as the order of MIMO transmitters increases.

6. A less complex polynomial-based DPD model is also proposed for linearization of MIMO transmitters by considering that nonlinearity introduced due to crosstalk would be less severe than the PA nonlinearity already present in the branches of MIMO transmitters. The main advantages of this model are:

   - The proposed polynomial-based DPD model is implemented in 4×4 MIMO transmitters having impairments like PA nonlinearity, nonlinear crosstalk and linear crosstalk.

- The results show that nonlinearity due to crosstalk can be modeled by half of the nonlinearity order as compared to the nonlinearity order of the main branch. This reduces the model complexity and coefficient extraction burden of DPD.

7.2 Future Work

Some of the potential future directions are listed as follows:

- The complexity of 3D-HMP and 3D-HVS models presented for DPD of concurrent tri-band transmitter operating at harmonics frequencies are very high. One of the direction for the future work would be to reduce model complexity of 3D-HMP and 3D-HVS models. The pruning techniques like PCA, ICA and compressed sampling (CS) can be used further to reduce model complexity.

- The proposed polynomial-based DPD model is presented for 4×4 MIMO transmitters. Another area of suggested future work would be extension of this polynomial-based DPD model for Massive MIMO transmitters. It can further include investigation of complexity reduction on behavioral modeling performance.

- The DPD technique can be used as spectrum and power efficient technique in high speed train communications, IOTs, D2D communications and other future communication applications. Power consumption and RF interference control are the key requirements of any efficient transceiver system. The nonlinearity produced by the RF PAs in transceiver devices should be addressed because it not only decreases the transmission quality, but also increases the interference among channels.

- With in a complete transceiver system an investigation regarding the challenges for implementing DPD in frequency hopping systems such as Wi-Fi can be done on how the implemented DPD designs can allow faster frequency hopping. To exclude the need of manual adjustment an automatic calibration can be added to fine tune the system.

- Another area of suggested future work is to investigate the performance and limitations of existent DPD models for latest 5G signals such as Filter Bank Multi-Carrier (FBMC), Generalized Frequency Division Multiplexing (GFDM), Universal Filtered

Multi-Carrier (UFMC), Filtered-OFDM (F-OFDM), Biorthogonal Frequency Division Multiplexing (BFDM) signal etc. This investigation will involve the effect of different bandwidths of these signals on performance of behavioral modeling and DPD.

Appendix A

Evaluation of elements of Jacobian Matrix J

The elements of jacobian matrix equation (6.16) are calculated using backpropagation algorithm. In this algorithm, the error of the outer layer is calculated as

$$\delta^{l+1} = f'\left(net^{l+1}\right) \tag{A.1}$$

After that error of the previous layer is calculated as

$$\delta^{l} = f'\left(net^{l}\right)\left(\mathbf{W}^{l+1}\right)^{T}\delta^{l+1} \tag{A.2}$$

Then, partial derivative with respect to weight is calculated as

$$\frac{\partial V}{\partial w_{ji}^{l}} = \delta_{j}^{l} o_{i}^{l-1} \tag{A.3}$$

and partial derivative with respect to bias is calculated as

$$\frac{\partial V}{\partial b_{j}^{l}} = \delta_{j}^{l} \tag{A.4}$$

The partial derivatives of inner layers can be found by repeating the above procedure ((A.1)–(A.4)). These partial derivatives with respect to weight and with respect to bias are the elements of the Jacobian matrix.

Appendix B

Simplification of Parallel Hammerstein Model

The expansion and simplification of first term of equation (6.17) is as follows

$$\begin{aligned}
&\sum_{m=0}^{M}\sum_{k=0}^{K-1}\sum_{j=0}^{k}\sum_{i=0}^{j}\sum_{h=0}^{i} x_1(n-m)\cdot\left(|x_1(n-m)|^{k-j}\left|\frac{x_2(n-m)}{\left(10^{1/2}\right)}\right|^{j-i}\left|\frac{x_3(n-m)}{\left(10^{1/2}\right)}\right|^{i-h}\left|\frac{x_4(n-m)}{\left(10^{1/2}\right)}\right|^{h}\right)\\
&=\sum_{m=0}^{M}\sum_{k=0}^{K-1} x_1(n-m)\cdot|x_1(n-m)|^{k}\\
&+\sum_{m=0}^{M}\sum_{k=1}^{K/2-1}\sum_{j=1}^{k}\sum_{i=1}^{j}\sum_{h=1}^{i} x_1(n-m)\cdot\left(|x_1(n-m)|^{k-j}\left|\frac{x_2(n-m)}{\left(10^{1/2}\right)}\right|^{j-i}\left|\frac{x_3(n-m)}{\left(10^{1/2}\right)}\right|^{i-h}\left|\frac{x_4(n-m)}{\left(10^{1/2}\right)}\right|^{h}\right)\\
&+\sum_{m=0}^{M}\sum_{k=K/2}^{K-1}\sum_{j=1}^{k}\sum_{i=1}^{j}\sum_{h=1}^{i} x_1(n-m)\cdot\left(|x_1(n-m)|^{k-j}\left|\frac{x_2(n-m)}{\left(10^{1/2}\right)}\right|^{j-i}\left|\frac{x_3(n-m)}{\left(10^{1/2}\right)}\right|^{i-h}\left|\frac{x_4(n-m)}{\left(10^{1/2}\right)}\right|^{h}\right)
\end{aligned} \tag{B.1}$$

Due to the fact that the high order terms have a week contribution as mentioned above in section 6.4, one can simplify equation (B.1) by neglecting the third term dedicated to the nonlinearity order of K/2 to K-1 and replacing the coupling factors of second term by coefficient $c^{(1)}_{m,k,j,i,h,1}$. The first term of equation (B.1) is the crosstalk-free response of the first branch of the 4×4 transmitter.

Considering the above, the first term of equation (6.17) simplifies as

$$\begin{aligned}
&\sum_{m=0}^{M}\sum_{k=0}^{K-1} x_1(n-m)\cdot|x_1(n)|^{k}\\
&+\sum_{m=0}^{M}\sum_{k=1}^{K/2-1}\sum_{j=1}^{k}\sum_{i=1}^{j}\sum_{h=1}^{i} c^{(1)}_{m,k,j,i,h,1} x_1(n-m)\cdot|x_1(n)|^{k-j}|x_2(n)|^{j-i}|x_3(n)|^{i-h}|x_4(n)|^{h}
\end{aligned} \tag{B.2}$$

Bibliography

[1] P. B. Kenington, "RF and Baseband Techniques for Software Defined Radio," Artech House, Inc., Norwood, MA, 2005.

[2] A. Mohammadi, and F. M. Ghannouchi, "RF Transceiver Design for MIMO Wireless Communications," Springer, 2012.

[3] 3GPP RP-091440, "Work Item Description: Carrier Aggregation for LTE," Nokia Corporation, Sanya, P.R. China, Dec. 2009.

[4] K. I. Pedersen *et al.*, "Carrier Aggregation for LTE-Advanced: Functionality and Performance Aspects," *IEEE Commun. Mag.*, vol. 49, no. 6, pp. 89–95, Jun. 2011.

[5] S. Cripps, "RF power amplifers for wireless communications," 2nd ed. Boston: Artech House, 2006.

[6] J. I. Díaz, C. Pantaleón, I. Santamaría, T. Fernández, and D. Martínez, "Nonlinearity estimation in power amplifiers based on subsampled temporal data," *IEEE Trans. Instrum. Meas.*, vol. 50, no. 4, pp. 882–886, Aug. 2001.

[7] F. H. Raab, P. Asbeck, S. Cripps, P. B. Kenington, Z. B. Popovic, N. Pothecary, J. F. Sevic, N. O. Sokal, "Power amplifiers and transmitters for RF and microwave," *IEEE Trans. Microwave Theory Techn.*, vol. 50, no. 3, pp. 814-826, Mar. 2002.

[8] D. Mirri, F. Filicori, G. Iuculano, and G. Pasini, "A nonlinear dynamic model for performance analysis of large-signal amplifiers in communication systems," *IEEE Trans. Instrum. Meas.*, vol. 53, no. 2, pp. 341–350, Apr. 2004.

[9] K. A. Remley, D. F. Williams, D. Schreurs, and J. Wood, "Simplifying and interpreting two-tone measurements," *IEEE Trans. Microwave Theory Techn.*, vol. 52, no. 11, pp. 2576–2584, Nov. 2004.

[10] J. Verspecht, D. F. Williams, D. Schreurs, K. A. Remley and M. D. McKinley, "Linearization of large-signal scattering functions," *IEEE Trans. Microwave Theory Techn.*, vol. 53, no. 4, pp. 1369-1376, Apr. 2005.

[11] R. Wang, Y. K. Su, and C. H. Liu, "35 GHz cascaded UWB power amplifier," *IEEE Asia Pacific Circuits Syst. Conf.*, Dec. 2006, pp. 367–369.

[12] "Study on Energy Efficient Radio Access Network (EERAN) Technologies," 2009 Project Report of Technical University of Dresden, Vodafone Chair Mobile Communication Systems.

[13] Lydi Smaini, "RF Analog Impairments Modeling for Communication Systems Simulation: Application to OFDM-based Transceivers," Wiley, Inc., 2012.

[14] U. Goyal, and M. Mishra, "Improved parameter extraction technique for GAN HEMT's small signal model," *2014 IEEE 2nd International Conf. on Emerging Electronics (ICEE)*, Bengalore, 2014, pp. 1–3.

[15] M. Mishra, S. Kumar, S. K. Tomar, S. Vinayak, and B. K. Sehgal, "Effect of traps on small signal equivalent circuit in AlGaN/GaN HEMTs," *2014 IEEE 2nd International Conf. on Emerging Electronics (ICEE)*, Bengalore, 2014, pp. 1–4.

[16] H. Jang, P. Roblin and Z. Xie, "Model-Based Nonlinear Embedding for Power-Amplifier Design," *IEEE Trans. Microw. Theory Techn.*, vol. 62, no. 9, pp. 1986–2002, Sep. 2014.

[17] H. Jang, P. Roblin, C. Quindroit, Y. Lin, and R. D. Pond, "Asymmetric Doherty Power Amplifier Designed Using Model-Based Nonlinear Embedding," *IEEE Trans. Microw. Theory Techn.*, vol. 62, no. 12, pp. 3436–3451, Dec. 2014.

[18] A. Jindal, U. Goyal, S. K. Tomar, M. Mishra, and S. Vinayak, "Design of a 2.8 W S-band power amplifier using load pull measurement," *2015 IEEE Applied Electromagnetics Conf. (AEMC)*, Guwahati, India, 2015, pp. 1–2.

[19] U. Goyal, S. K. Tomar, M. Mishra and S. Vinayak, "Design and development of S band 10W and 20W power amplifier," *2015 IEEE Applied Electromagnetics Conf. (AEMC)*, Guwahati, India, 2015, pp. 1–2.

[20] J. K. Cavers, "Amplifier linearization using a digital predistorter with fast adaptation and low memory requirements," *IEEE Trans. Veh. Technol.*, vol. 39, no. 4, pp. 374-382, Nov. 1990.

[21] O. Hammi, F. M. Ghannouchi, S. Boumaiza, and B. Vassilakis, "A data-based nested LUT model for RF power amplifiers exhibiting memory effects" *IEEE Microw. Wireless Compon. Lett.*, vol. 17, no. 10, pp. 712–714, Oct. 2007.

[22] C. Eun, and E. J. Powers, "A new Volterra predistorter based on the indirect learning architecture," *IEEE Trans. Signal Process.*, vol. 45, no. 1, pp. 223–227, Jan. 1997.

[23] J. Kim and K. Konstantinou, "Digital predistortion of wideband signals based on power amplifier model with memory," *Electron. Lett.*, vol. 37, no. 23, pp. 1417–1418, Nov. 2001.

[24] L. Ding *et al.*, "A robust digital baseband predistorter constructed using memory polynomials," *IEEE Trans. Commun.*, vol. 52, no. 1, pp. 159–165, Jan. 2004.

[25] R. Raich, H. Qian, and G. T. Zhou, "Orthogonal polynomials for power amplifier modeling and predistorter design," *IEEE Trans. Veh. Technol.*, vol. 53, no. 5, pp. 1468–1479, Sep. 2004.

[26] O. Hammi, F. M. Ghannouchi, and B. Vassilakis, "A compact envelope-memory polynomial for RF transmitters modeling with application to baseband and RF-digital predistortion," *IEEE Microw. Wireless Compon. Lett.*, vol. 18, no. 5, pp. 359–361, May 2008.

[27] D. Morgan, Z. Ma, J. Kim, M. Zierdt, and J. Pastalan, "A generalized memory polynomial model for digital predistortion of RF power amplifiers," *IEEE Trans. Signal Process.*, vol. 54, no. 10, pp. 3852–3860, Oct. 2006.

[28] A. Zhu, J. C. Pedro, and T. J. Brazil, "Dynamic deviation reduction-based behavioral modeling of RF power amplifiers," *IEEE Trans. Microw. Theory Techn.*, vol. 54, no. 12, pp. 4323–4332, Dec. 2006.

[29] A. Zhu, P. J. Draxler, J. J. Yan, T. J. Brazil, D. F. Kimball, and P. M. Asbeck, "Open-loop digital predistorter for RF power amplifiers using dynamic deviation reduction-

based Volterra series," *IEEE Trans. Microw. Theory Techn.*, vol. 56, no. 7, pp. 1524–1534, Jul. 2008.

[30] M. Rawat, K. Rawat, F.M. Ghannouchi, S. Bhattacharjee and H. Leung, "Generalized Rational Functions for Reduced-Complexity Behavioral Modeling and Digital Predistortion of Broadband Wireless Transmitters," *IEEE Trans. Instrum. Meas.*, vol. 63, no. 2, pp. 485–498, Feb. 2014.

[31] N. Safari, P. Fedorenko, J. S. Kenney, and T. Roste, "Spline-based model for digital predistortion of wideband signals for high power amplifier linearization," *IEEE MTT-S Int. Microwave Symp.*, Honolulu, HI, USA, Jun. 2007, pp. 1441–1444.

[32] D. Rönnow, D. Wisell, and M. Isaksson, "Three-tone characterization of nonlinear memory effects in radio-frequency power amplifiers," *IEEE Trans. Instrum. Meas.*, vol. 56, no. 6, pp. 2646–2657, Dec. 2007.

[33] D. Schreurs, M. O'Droma, A. A. Goacher, and M. Gadringer, "RF power amplifier behavioral modeling," Cambridge University Press, New York, NY, USA, 2008.

[34] P. Roblin *et al.*, "Frequency-Selective Predistortion Linearization of RF Power Amplifiers," *IEEE Trans. Microw. Theory Techn.*, vol. 56, no. 1, pp. 65–76, Jan. 2008.

[35] O. Hammi, and F.M. Ghannouchi, "Power Alignment of Digital Predistorters for Power Amplifiers Linearity Optimization," *IEEE Transactions on Broadcasting*, vol. 55, no. 1, pp. 109-114, Mar. 2009.

[36] F. M. Ghannouchi, and O. Hammi, "Behavioral modeling and predistortion," *IEEE Microw. Mag.*, vol.10, no.7, pp. 52–64, Dec. 2009.

[37] A. Katz, "Linearization: Reducing Distortion in Power Amplifiers," *IEEE Microw. Mag.*, vol. 2, no. 4, pp. 37-49, Dec. 2011.

[38] K. J. Muhonen, M. Kavehrad, and R. Krishnamoorthy, "Look-up table techniques for adaptive digital predistortion: a development and comparison," *IEEE Trans Veh Technol.*, vol. 49, no. 5, pp. 1995-2-002, Sep. 2000.

[39] K. Rawat, M. Rawat, and F. M. Ghannouchi, "Compensating IQ imperfections in hybrid RF/digital predistortion with an adapted look up table implemented in an

FPGA," *IEEE Trans. Circuits Syst. II Exp. Briefs*, vol. 57, no. 5, pp. 389–393, May 2010.

[40] M. Rawat, P. Roblin, C. Quindroit, N. Naraharisetti, R. Pond, K. Salam, and C. Xie, "Characterization and modeling scheme for harmonics at power amplifier output," in *83rd ARFTG Microw. Meas. Symp.*, Tampa, FL, USA, Jun. 2014, pp. 1–4.

[41] M. Rawat, P. Roblin, C. Quindroit, K. Salam, and C. Xie, "Digitally supported feed-forward harmonic cancellation for filter-less ultra-wideband transmitters," in *IEEE Int. Microw. RF Conf.*, Dec. 2014. pp. 1–4.

[42] M. Rawat, P. Roblin, C. Quindroit, K. Salam, and C. Xie, "Concurrent Dual-Band Modeling and Digital Predistortion in the Presence of Unfilterable Harmonic Signal Interference," *IEEE Trans. Microw. Theory Techn.*, vol. 63, no. 2, pp. 625–637, Feb. 2015.

[43] S. A. Bassam, M. Helaoui, and F. M. Ghannouchi, "2-D digital predistortion (2-DDPD) architecture for concurrent dual-band transmitters," *IEEE Trans. Microw. Theory Techn.*, vol. 59, no. 10, pp. 2547–2553, Oct. 2011.

[44] G. Yang, F. Liu, L. Li, H. Wang, C. Zhao, and Z. Wang, "2D orthogonal polynomials for concurrent dual-band digital predistortion," in *IEEE MTT-S Int. Microw. Symp. Dig.*, Seattle, WA, USA, Jun. 2013, pp. 1–3.

[45] C. Quindroit, N Naraharisetti, P Roblin, S Gheitanchi, V Mauer, and M Fitton, "FPGA Implementation of Orthogonal 2D Digital Predistortion System for Concurrent Dual-Band Power Amplifiers Based on Time-Division Multiplexing," *IEEE Trans. Microw. Theory Techn.*, vol. 61, no. 12, pp. 4591–4599, Dec. 2013.

[46] Y.-J. Liu, J. Zhou, W. Chen, B. Zhou, and F.M. Ghannouchi, "Low complexity 2D behavioural model for concurrent dual-band power amplifiers," *Electron. Lett.*, vol. 48, no. 11, pp. 620-621, May 2012.

[47] M. Rawat, C. Quindroit, P. Roblin, N. Narharishetti, R. Pond, K. Salam and C. Xie, "Concurrent Dual-band transmitter behavioral modeling with physically motivated 2-D rational functions," in *82nd ARFTG Microw. Meas. Symp.*, Columbus, OH, USA, Nov. 2013, pp. 1–4.

[48] L. Ding, Z. Yang, and H. Gandhi, "Concurrent dual-band digital predistortion," in *IEEE MTT-S Int. Microw. Symp. Dig.*, Montreal, QC, Canada, Jun. 2012, pp. 1–3.

[49] N. Naraharisetti, P. Roblin, C. Quindroit, and S. Gheitanchi, "Efficient Least-Squares 2-D-Cubic Spline for Concurrent Dual-Band Systems," *IEEE Trans. Microw. Theory Techn.*, vol. 63, no. 7, pp. 2199-2210, Jul. 2015.

[50] P. Jaraut, and M. Rawat, "Complexity and Numerical Stability investigation in Concurrent Dual-Band Modeling of Ultra-Wideband Power Amplifiers for Harmonically related Signals," in *Proc. IEEE MTT-S Asia-Pacific Microw. Conf.*, New Delhi, India, Dec. 2016, pp. 1–4.

[51] S. Sharma, and C. C. Tripathi, "Frequency Reconfigurable U-Slot Antenna for SDR Application," *Progress In Electromagnetics Research Letters*, vol. 55, pp. 129-136, 2015.

[52] S. Sharma, and C. C. Tripathi, "A versatile reconfigurable antenna for Cognitive Radio," *2016 Asia-Pacific Microwave Conference (APMC)*, New Delhi, India, 2016, pp. 1–4.

[53] S. Sharma, and C. C. Tripathi, "Wideband to concurrent tri-band frequency reconfigurable microstrip patch antenna for wireless communication," *International Journal of Microwave and Wireless Technologies*, vol. 9, no. 4, pp. 915-922, 2017.

[54] S. A. Bassam, M. Helaoui, and F. M. Ghannouchi, "Crossover digital predistorter for the compensation of crosstalk and nonlinearity in MIMO transmitters," *IEEE Trans. Microw. Theory Techn.*, vol. 57, no. 5, pp. 1119–1128, May 2009.

[55] S. Amin, P. N. Landin, P. Händel, and D. Rönnow, "Behavioral modeling and linearization of crosstalk and memory effects in RF MIMO transmitters," *IEEE Trans. Microw. Theory Techn.*, vol. 62, no. 4, pp. 810–823, Apr. 2014.

[56] D. Saffar, N. Boulejfen, F. Ghannouchi, A. Gharsallah, and M. Helaoui, "Behavioral modeling of MIMO nonlinear systems with multivariable polynomials," *IEEE Trans. Microw. Theory Techn.*, vol. 59, no. 11, pp. 2994–3003, Nov. 2011.

[57] A. Abdelhafiz, L. Behjat, F. M. Ghannouchi, M. Helaoui and O. Hammi, "A High-Performance Complexity Reduced Behavioral Model and Digital Predistorter for

MIMO Systems With Crosstalk," *IEEE Trans. Commun.*, vol. 64, no. 5, pp. 1996–2004, May 2016.

[58] H. Qian, X. Cheng, X. Luo and W. Feng, "Calibration of Nonlinear Crosstalk in MIMO Transmitter," *IEEE Trans. Veh. Technol.*, vol. 66, no. 5, pp. 3739–3748, May 2017.

[59] M. Alizadeh, S. Amin and D. Rönnow, "Measurement and Analysis of Frequency-Domain Volterra Kernels of Nonlinear Dynamic 3×3 MIMO Systems," *IEEE Trans. Instrum. Meas.*, vol. 66, no. 7, pp. 1893–1905, Jul. 2017.

[60] E. Zenteno and D. Rönnow, "MIMO Subband Volterra Digital Predistortion for Concurrent Aggregated Carrier Communications," *IEEE Trans. Microw. Theory Techn.*, vol. 65, no. 3, pp. 967–979, March 2017.

[61] A. Vaezi, A. Abdipour, A. Mohammadi and F. M. Ghannouchi, "On the Modeling and Compensation of Backward Crosstalk in MIMO Transmitters," *IEEE Microw. Wireless Compon. Lett.*, vol. 27, no. 9, pp. 842–844, Sept. 2017.

[62] L. Guan, and A. Zhu, "Low-Cost FPGA Implementation of Volterra Series-Based Digital Predistorter for RF Power Amplifiers," *IEEE Trans. Microw. Theory Techn.*, vol. 58, no. 4, pp. 866–872, Apr. 2010.

[63] L. Guan, and A. Zhu, "Optimized Low-Complexity Implementation of Least Squares Based Model Extraction for Digital Predistortion of RF Power Amplifiers," *IEEE Trans. Microw. Theory Techn.*, vol. 60, no. 3, pp. 594–603, Mar. 2012.

[64] F. M. Barradas, T. R. Cunha, P. M. Lavrador, and J. C. Pedro, "Polynomials and LUTs in PA Behavioral Modeling: A Fair Theoretical Comparison," *IEEE Trans. Microw. Theory Techn.*, vol. 62, no. 12, pp. 3274–3285, Dec. 2014.

[65] I.T. Jolliffe, "Principal Component Analysis," Springer-Verlag, 2002.

[66] R. Neil Braithwaite, "Wide bandwidth adaptive digital predistortion of power amplifiers using reduced order memory correction," in *IEEE MTT-S Int. Microw. Symp. Dig.*, Jun. 2008, pp. 1517–1520.

[67] P. L. Gilabert *et al.*, "Order reduction of wideband digital predistorters using principal component analysis," in *IEEE MTT-S Int. Microw. Symp. Dig.*, Seattle, WA, USA, Jun. 2013, pp. 1–4.

[68] P. L. Gilabert and G. Montoro, "3-D Distributed Memory Polynomial Behavioral Model for Concurrent Dual-Band Envelope Tracking Power Amplifier Linearization," *IEEE Trans. Microw. Theory Techn.*, vol. 63, no. 2, pp. 638–648, Feb. 2015.

[69] Y. Lin, C. Quindroit, H. Jang, and P. Roblin, "3-D Fourier Series Based Digital Predistortion Technique for Concurrent Dual-Band Envelope Tracking With Reduced Envelope Bandwidth," *IEEE Trans. Microw. Theory Techn.*, vol. 63, no. 9, pp. 2764–2775, Sep. 2015.

[70] T. Wang, P. L. Gilabert, and G. Montoro, "Under-sampling effects and computational cost reduction in RF power amplifier behavioral modeling," in *Proc. European Microwave Integrated Circuits Conf.*, Sep. 2015, pp. 57–60.

[71] P. Jaraut, and M. Rawat, "Application of principal component analysis based effective digital predistortion technique for low-cost FPGA implementation," *Int. J. RF and Microw. Comput.-Aided Eng.*, vol. 27, no. 6, pp. 1–15, Aug. 2017, DOI: 10.1002/mmce.21095.

[72] S. S. Lokesh, A. Kumar, and M. Agrawal, "On the hierarchical least-squares algorithm," *IEEE Commun. Lett.*, vol. 6, no. 4, pp. 153–155, Apr. 2002.

[73] S. S. Lokesh, A. Kumar, and M. Agrawal, "Structure of an Optimum Linear Precoder and its Application to ML Equalizer," *IEEE Trans. Signal Processing*, vol. 56, no. 8, pp. 3690–3701, Aug. 2008.

[74] G. H. Golub, and C. F. Van Loan, *Matrix Computations*, 3rd ed. Baltimore, MD, USA: The Johns Hopkins Univ. Press, 1996, ch. 2, p. 81.

[75] E. W. Cheney, and D. Kincaid, *Numerical Mathematics and Computing*, 7th ed. Pacific Grove, CA, USA: Brooks/Cole, 2008, ch. 8, p. 321.

[76] J. H. Wilkinson, *The Algebraic Eigenvalue Problem.* Oxford, U.K.: Claredon Press, 1995, p. 374.

[77] B. Beckermann, "The condition number of real Vandermonde, Krylov and positive definite Hankel matrices," *Numer. Math.*, vol. 85, no. 4, pp. 553–577, Apr. 2000.

[78] M. Rawat, F. M. Ghannouchi, and K. Rawat, "Three-layered biased memory polynomial for modeling and predistortion of transmitters with memory," *IEEE Trans. Circuits Syst. I, Reg. Papers*, vol. 60, no. 3, pp. 768–777, Mar. 2013.

[79] P. N. Landin, M. Isaksson, and P. Händel, "Comparison of evaluation criteria for power amplifier behavioral modeling," in *IEEE MTT-S Int. Microw. Symp. Dig.*, Jun. 2008, pp. 1441–1444.

[80] D. Y.-T. Wu and S. Boumaiza, "A modified Doherty configuration for broadband amplification using symmetrical devices," *IEEE Trans. Microw. Theory Techn.*, vol. 60, no. 10, pp. 3201–3213, Oct. 2012.

[81] S. V. Thyagarajan, A. M. Niknejad, and C. D. Hull, "A 60 GHz Drain-Source Neutralized Wideband Linear Power Amplifier in 28 nm CMOS," *IEEE Trans. Circuits Syst. I: Reg. Papers*, vol. 61, no. 8, pp. 2253–2262, Aug. 2014.

[82] R. Giofrè, L. Piazzon, P. Colantonio, and F. Giannini, "A Closed-Form Design Technique for Ultra-Wideband Doherty Power Amplifiers," *IEEE Trans. Microw. Theory Techn.*, vol. 62, no. 12, pp. 3414–3424, Oct. 2014.

[83] R. Liu, D. Schreurs, W. De Raedt, F. Vanaverbeke, and R. Mertens, "Concurrent dual-band power amplifier with different operation modes," in *IEEE MTT-S Int. Microw. Symp. Dig.*, Baltimore, MD, USA, Jun. 2011, pp. 1–4.

[84] W. Chen, S. Zhang, Y. Liu, Y. Liu, and F. Ghannouchi, "A concurrent dual-band uneven Doherty power amplifier with frequency-dependent input power division," *IEEE Trans. Circuits Syst. I: Reg. Papers*, vol. 61, no. 2, pp. 552–561, Feb. 2014.

[85] A. Hyvärinen, J. Karhunen, and E. Oja, "ICA by Maximization of Nongaussianity," in *Independent Component Analysis*, John Wiley & Sons, 2001, ch. 8, sec. 8.3.5, pp. 188–192.

[86] P. Jaraut, G. C. Tripathi, M. Rawat and P. Roblin, "Independent component analysis for multi-carrier transmission for 4G/5G power amplifiers," in *89th ARFTG Microwave Measurement Conference (ARFTG)*, Honolulu, HI, Jun. 2017, pp. 1–4.

[87] P. Jaraut, M. Rawat, and P. Roblin, "Digital Predistortion technique for Low resource consumption using Carrier Aggregated 4G/5G Signals," *IET Microw. Antennas Propag.*, vol. 13, no. 2, pp. 197–207, Feb. 2019.

[88] M. Agrawal and S. Prasad, "A modified likelihood function approach to DOA estimation in the presence of unknown spatially correlated Gaussian noise using a uniform linear array," *IEEE Trans. Signal Process.*, vol. 48, no. 10, pp. 2743–2749, Oct. 2000.

[89] P. Rost *et al.*, "Mobile network architecture evolution toward 5G," *IEEE Commun. Mag.*, vol. 54, no. 5, pp. 84–91, May 2016.

[90] A. Nordrum, "5 myths about 5G," *IEEE Spectrum*, May 2016.

[91] A. Maeder *et al.*, "A Scalable and Flexible Radio Access Network Architecture for Fifth Generation Mobile Networks," *IEEE Commun. Mag.*, vol. 54, no. 11, pp. 16–23, Nov. 2016.

[92] *Understanding the Requirements for LTE-Advanced Carrier Aggregation Manufacturing Test*, Agilent Technol., Santa Clara, CA, USA, Appl. Note 5991-3762EN, 2014.

[93] 3GPP R4-120442, "Way forward for inter-band CA Class A2," Nokia Corporation, Dresden, Germany, Feb. 2012.

[94] 3GPP R4-123845, "Feasibility study of harmonic spurious emission from B28 in Japan," NTT DOCOMO, Sharp, NEC, Qingdao, P.R. China, Aug. 2012.

[95] Y. J. Liu, W. Chen, J. Zhou, B. H. Zhou, and F. M. Ghannouchi, "Digital predistortion for concurrent dual-band transmitters using 2-D modified memory polynomials," *IEEE Trans. Microw. Theory Techn.*, vol. 61, no. 1, pp. 281–290, Jan. 2013.

[96] M. Omer, R. Rimini, P. Draxler, and J. S. Kenney, "Interference cancellation for odd harmonics of envelope tracking RF power amplifier systems," in *IEEE MTT-S Int. Microw. Symp. Dig.*, Seattle, WA, USA, Jun. 2013, pp. 1–3.

[97] P. Jaraut, M. Rawat and F. M. Ghannouchi, "2-D Curtailed Harmonic Memory Polynomial for reduced complexity in Concurrent Dual-Band Modeling and Digital Predistortion with the second band at Harmonic Frequency," *IET Commun.*, vol. 12, no. 12, pp. 1438–1447, Jul. 2018.

[98] M. Younes, A. Kwan, M. Rawat, and F. M. Ghannouchi, "Three-dimensional digital predistorter for concurrent tri-band power amplifier linearization," in *IEEE MTT-S Int. Microw. Symp. Dig.*, Seattle, WA, USA, Jun. 2013, pp. 1–4.

[99] M. Younes, A. Kwan, M. Rawat, and F. M. Ghannouchi, "Linearization of Concurrent Tri-Band Transmitters Using 3-D Phase-Aligned Pruned Volterra Model," *IEEE Trans. Microw. Theory Techn.*, vol. 61, no. 12, pp. 4569–4578, Dec. 2013.

[100] T. Tian, Y. Zhao, Y. Dou, C. Yu, and J. Qiu, "A novel concurrent triband digital predistortion for broadband signals," in *European Microwave Conference (EuMC)*, Paris, 2015, pp. 1136–1139.

[101] F. Mkadem, A. Islam, and S. Boumaiza, "Multi-Band Complexity-reduced Generalized-Memory-Polynomial Power-Amplifier Digital Predistortion," *IEEE Trans. Microw. Theory Techn.*, vol. 64, no. 6, pp. 1763–1774, Jun. 2016.

[102] A. Kwan, *et al.*, "Selective Intermodulation Compensation in a Multi-Stage Digital Predistorter for Nonlinear Multi-Band Power Amplifiers," *IEEE J. Emerg. Sel. Topics Circuits Syst.*, vol. 7, no. 4, pp. 534–546, Dec. 2017.

[103] P. Jaraut, M. Rawat, and F. M. Ghannouchi, "Harmonically Related Concurrent Tri-Band Behavioral Modeling and Digital Predistortion," *IEEE Trans. Circuits Syst. II, Exp. Briefs*, to be published. DOI: 10.1109/TCSII.2018.2873251.

[104] S. Lipschutz, "Arrays, Records and Pointers," in *Data Structures*, Revised 1st ed., Schaum's Outline Series, McGraw-Hill Education (India), 2013, ch. 4, sec. 4.8, pp. 4.15–4.18.

[105] E. G. Larsson, O. Edfors, F. Tufvesson, and T. L. Marzetta, "Massive MIMO for next generation wireless systems," *IEEE Commun. Mag.*, vol. 52, no. 2, pp. 186–195, Feb. 2014.

[106] M. R. Bhatnagar and A. Hjorungnes, "Differential Coding for MAC Based Two-User MIMO Communication Systems," *IEEE Trans. Wireless Commun.*, vol. 11, no. 1, pp. 9–14, Jan. 2012.

[107] A. M.K., and M. R. Bhatnagar, "Performance Analysis of Two-Way AF MIMO Relaying of OSTBCs With Imperfect Channel Gains," *IEEE Trans. Veh. Technol.*, vol. 63, no. 8, pp. 4118–4124, Oct. 2014.

[108] J. Gozalvez, "Samsung electronics sets 5G speed record at 7.5 Gb/s [mobile radio]," *IEEE Veh. Technol. Mag.*, vol. 10, no. 1, pp. 12–16, Mar. 2015.

[109] V. S. Krishna, and M. R. Bhatnagar, "A Joint Antenna and Path Selection Technique in Single-Relay-Based DF Cooperative MIMO Networks," *IEEE Trans. Veh. Technol.*, vol. 65, no. 3, pp. 1340-1353, March 2016.

[110] A. Jaiswal, M. Abaza, M. R. Bhatnagar, and V. K. Jain, "An Investigation of Performance and Diversity Property of Optical Space Shift Keying-Based FSO-MIMO System," *IEEE Trans. Commun.*, vol. 66, no. 9, pp. 4028–4042, Sep. 2018.

[111] Y. Palaskas *et al.*, "A 5-GHz 108-Mb/s 2×2 MIMO transceiver RFIC with fully integrated 20.5-dBm power P1dB amplifiers in 90-nm CMOS," *IEEE J. Solid-State Circuits*, vol. 41, no. 12, pp. 2746–2756, Dec. 2006.

[112] H. Zareian, and V. T. Vakili, "Analytical EVM, BER, and TD performances of the OFDM systems in the presence of jointly nonlinear distortion and IQ imbalance," *Ann. Telecommun.*, vol. 64, nos. 1112, pp. 753–762, 2009.

[113] M. Aziz, M. Rawat, and F. M. Ghannouchi, "Rational function based model for the joint mitigation of I/Q imbalance and PA nonlinearity," *IEEE Microw. Compon. Lett.*, vol. 23, no. 4, pp. 196–198, Apr. 2013.

[114] H. Cao, A. S. Tehrani, C. Fager, T. Eriksson, and H. Zirath, "I/Q imbalance compensation using a nonlinear modeling approach," *IEEE Trans. Microw. Theory Techn.*, vol. 57, no. 3, pp. 513–518, Mar. 2009.

[115] L. Anttila, P. Händel, and M. Valkama, "Joint mitigation of power amplifier and I/Q modulator impairments in broadband direct-conversion transmitters," *IEEE Trans. Microw. Theory Techn.*, vol. 58, no. 4, pp. 730–739, Apr. 2010.

[116] Z. Zhu, X. Huang, and H. Leung, "Joint I/Q mismatch and distortion compensation in direct conversion transmitters," *IEEE Trans. Wireless Commun.*, vol. 12, no. 6, pp. 2941–2951, Jun. 2013.

[117] M. Kim, Y. Maruichi, and J. I. Takada, "Parametric method of frequency dependent I/Q imbalance compensation for wideband quadrature modulator," *IEEE Trans. Microw. Theory Techn.*, vol. 61, no. 1, pp. 270–280, Jan. 2013.

[118] W. Li, Y. Zhang, L.-K. Huang, J. Cosmas, C. Maple, and J. Xiong, "Self-IQ-demodulation based compensation scheme of frequency-dependent IQ imbalance for wideband direct-conversion transmitters," *IEEE Trans. Broadcast.*, vol. 61, no. 4, pp. 666–673, Dec. 2015.

[119] Z. A. Khan, E. Zenteno, P. Händel and M. Isaksson, "Digital Predistortion for Joint Mitigation of I/Q Imbalance and MIMO Power Amplifier Distortion," *IEEE Trans. Microw. Theory Techn.*, vol. 65, no. 1, pp. 322–333, Jan. 2017.

[120] P. Jaraut, M. Rawat, and F. M. Ghannouchi, "Composite Neural Network Digital Predistortion Model for Joint Mitigation of Crosstalk, I/Q Imbalance, Nonlinearity in MIMO Transmitters," *IEEE Trans. Microw. Theory Techn.*, vol. 66, no. 11, pp. 5011–5020, Nov. 2018.

[121] S. Haykin, *Neural Networks: A Comprehensive Foundation.*, Upper Saddle River, NJ: Prentice-Hall, 1999.

[122] M. T. Hagan and M. B. Menhai, "Training feedforward network with the Marquardt algorithm," *IEEE Trans. Neural Net.*, vol. 5, no. 6, pp. 989–993, Nov. 1994.

[123] M. Rawat, K. Rawat, and F. M. Ghannouchi, "Adaptive digital predistortion of wireless power amplifiers/transmitters using dynamic real-valued focused time-delay line neural networks," *IEEE Trans. Microw. Theory Tech.*, vol. 58, no. 1, pp. 95–104, Jan. 2010.

[124] M. Rawat, and F. M. Ghannouchi, "A mutual distortion and impairment compensator for wideband direct conversion transmitters using neural networks," *IEEE Trans. Broadcast.*, vol. 58, no. 2, pp. 95–104, Jun. 2012.

[125] S. Li, K. Choi, and Y. Lee, "Artificial neural network implementation in FPGA: A case study," in *International SoC Design Conference (ISOCC)*, Jeju, 2016, pp. 297–298.

[126] P. Ranjan, S. Raj, G. Upadhyay, S. Tripathi, and V. S. Tripathi, "Circularly slotted flower shaped UWB filtering antenna with high peak gain performance," *AEU-International Journal of Electronics and Communications*, vol. 81, no. 1, pp. 209–217, Nov. 2017.

[127] N. Kishore, G. Upadhyay, A. Prakash, and V. S. Tripathi, "Millimeter Wave Antenna for Intelligent Transportation Systems Application," *Journal of Microwaves, Optoelectronics and Electromagnetic Applications*, vol. 17, no. 1, pp. 171–178, Mar. 2018.

[128] G. Upadhyay, N. Kishore, S. Raj, S.Tripathi, and V. S. Tripathi, "Dual-feed CSRR-loaded switchable multiband microstrip patch antenna for ITS applications," *IET Microw. Antennas Propag.*, to be published DOI: 10.1049/iet-map.2018.5269.

List of Publications

International Journals

1. **P. Jaraut**, M. Rawat, and P. Roblin, "Digital Predistortion technique for Low resource consumption using Carrier Aggregated 4G/5G Signals," *IET Microw. Antennas Propag.*, vol. 13, no. 2, pp. 197–207, Feb. 2019.

2. **P. Jaraut**, M. Rawat, and F. M. Ghannouchi, "Harmonically Related Concurrent Tri-Band Behavioral Modeling and Digital Predistortion," *IEEE Trans. Circuits Syst. II, Exp. Briefs*, to be published. DOI: 10.1109/TCSII.2018.2873251.

3. **P. Jaraut**, M. Rawat, and F. M. Ghannouchi, "Composite Neural Network Digital Predistortion Model for Joint Mitigation of Crosstalk, I/Q Imbalance, Nonlinearity in MIMO Transmitters," *IEEE Trans. Microw. Theory Techn.*, vol. 66, no. 11, pp. 5011–5020, Nov. 2018.

4. **P. Jaraut**, M. Rawat, and F. M. Ghannouchi, "2-D Curtailed Harmonic Memory Polynomial for reduced complexity in Concurrent Dual-Band Modeling and Digital Predistortion with the second band at Harmonic Frequency," *IET Commun.*, vol. 12, no. 12, pp. 1438–1447, Jul. 2018.

5. **P. Jaraut**, and M. Rawat, "Application of principal component analysis based effective digital predistortion technique for low-cost FPGA implementation," *Int. J. of RF and Microw. Comput.-Aided Eng.*, vol. 27, no. 6, pp. 1–15, Aug. 2017, DOI: 10.1002/mmce.21095.

6. **P. Jaraut**, M. Rawat, and F. M. Ghannouchi, "Efficient Linearization Technique for Crosstalk and Power Amplifier Nonlinearity Suitable Massive MIMO Transmitters," *IEEE Trans. Commun.*, **under review**.

International Conferences

1. **P. Jaraut**, M. Rawat, and P. Roblin, "Curtailed Digital Predistortion Model for Crosstalk in MIMO Transmitters," in *IEEE MTT-S Int. Microw. Symp. Dig.*, Philadelphia, PA, USA, Jun. 2018, pp. 927–930.

2. **P. Jaraut**, and M. Rawat, "3D Generalized coefficient supported model for Concurrent Dual-Band Digital Predistortion of Envelope Tracking Power Amplifier," in *IEEE MTT-S Int. Microw. RF Conf.*, Ahmedabad, India, Dec. 2017, pp. 1–4.

3. **P. Jaraut**, G. C. Tripathi, M. Rawat, and P. Roblin, "Independent Component Analysis for multi-carrier transmission for 4G/5G Power Amplifiers," in *89th ARFTG Microw. Meas. Symp.*, Honolulu, Hawaii, USA, Jun. 2017, pp. 1–4.

4. **P. Jaraut**, and M. Rawat, "Complexity and Numerical Stability investigation in Concurrent Dual-Band Modeling of Ultra-Wideband Power Amplifiers for Harmonically related Signals," in *Proc. IEEE MTT-S Asia-Pacific Microw. Conf.*, New Delhi, India, Dec. 2016, pp. 1–4.

5. K. Gumber, **P. Jaraut**, M. Rawat and K. Rawat, "Digitally assisted analog predistortion technique for power amplifier," in *88th ARFTG Microw. Meas. Symp.*, Austin, TX, USA, Dec. 2016, pp. 1–4.

6. G. C. Tripathi, **P. Jaraut**, M. Rawat and L. N. Reddy, "Digital Predistortion of Power Amplifiers with Diversity Technique in 4G MIMO Transceivers," in *Proc. IEEE MTT-S Int. Microw. & RF Conf. (IMaRC)*, Hyderabad, India, 2015, pp. 53–55.

7. R. Singh, M. Rawat, and **P. Jaraut**, "Novel implementation topology for Three Level Delta Sigma Modulation Based Transmitter," in *IEEE Applied Electromagnetics Conference (AEMC-2015)*, Guwahati, India, 2015, pp 1–2.

8. G. C. Tripathi, **P. Jaraut**, M. Rawat and L. N. Reddy, "Low cost implementation of Software Defined Radio for improved transmit quality of 4G signals," in *Proc. IEEE Int. Conf. on Commun. Control and Intelligent syst. (CCIS-2015)*, Mathura, 7-8th Nov.2015, pp. 108–112.